Cell Reports

Article

Cytoskeletal activation of NHE1 regulates mechanosensitive cell volume adaptation and proliferation

Graphical abstract

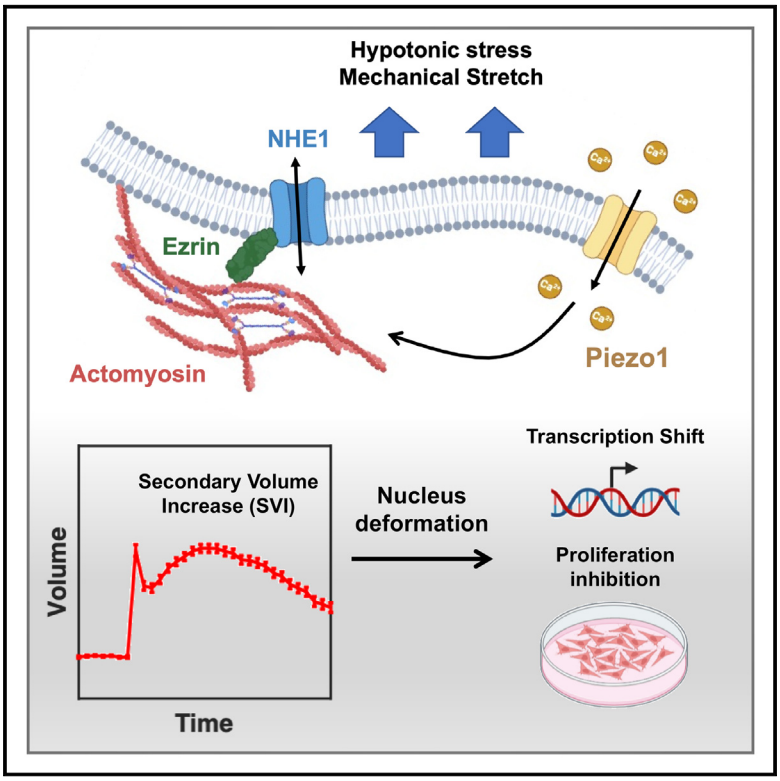

Authors

Qin Ni, Zhuoxu Ge, Yizeng Li, ..., Andrew P. Feinberg, Konstantinos Konstantopoulos, Sean X. Sun

Correspondence

ssun@jhu.edu

In brief

Ni et al. investigate the role of actomyosin and ion exchangers in cell volume regulation. They identify a secondary volume increase (SVI) in normal-like cells via cytoskeleton-mediated NHE1 activation. SVI is absent in cancer cells and on compliant substrates. This leads to nucleus deformation, transcriptomic changes, and ERK-dependent growth inhibition.

Highlights

- Hypotonic stress triggers a secondary volume increase in non-cancerous cells
- Actomyosin regulates cell and nucleus volume via NHE1 activation through Piezo1 and ezrin
- Acute transcriptomic and epigenetic changes follow NHE1-induced nucleus deformation
- Cytoskeletal activation of NHE1 results in ERK-dependent growth inhibition

Ni et al., 2024, Cell Reports *43*, 114992
December 24, 2024
https://doi.org/10.1016/j.celrep.2024.114992

CellPress

Cell Reports

CellPress
OPEN ACCESS

Article

Cytoskeletal activation of NHE1 regulates mechanosensitive cell volume adaptation and proliferation

Qin Ni,[1,2,10] Zhuoxu Ge,[1,2,10] Yizeng Li,[3] Gabriel Shatkin,[4] Jinyu Fu,[1,5] Anindya Sen,[1,6] Kaustav Bera,[1,6] Yuhan Yang,[7] Yichen Wang,[2] Yufei Wu,[1,2] Ana Carina Nogueira Vasconcelos,[1,2] Yuqing Yan,[1,8] Dingchang Lin,[1,8] Andrew P. Feinberg,[4,7,9] Konstantinos Konstantopoulos,[1,4,6,7] and Sean X. Sun[1,2,11,*]

[1]Institute for NanoBioTechnology, Johns Hopkins University, Baltimore, MD, USA
[2]Department of Mechanical Engineering, Johns Hopkins University, Baltimore, MD, USA
[3]Department of Biomedical Engineering, Binghamton University, Binghamton, NY, USA
[4]Department of Biomedical Engineering, Johns Hopkins University, Baltimore, MD, USA
[5]Department of Physics, Johns Hopkins University, Baltimore, MD, USA
[6]Department of Chemical and Biomolecular Engineering, Johns Hopkins University, Baltimore, MD, USA
[7]Department of Oncology, The Sidney Kimmel Comprehensive Cancer Center, Johns Hopkins University School of Medicine, Baltimore, MD, USA
[8]Department of Materials Science and Engineering, Johns Hopkins University, Baltimore, MD, USA
[9]Center for Epigenetics, Johns Hopkins University School of Medicine, Baltimore, MD, USA
[10]These authors contributed equally
[11]Lead contact
*Correspondence: ssun@jhu.edu
https://doi.org/10.1016/j.celrep.2024.114992

SUMMARY

Mammalian cells rapidly respond to environmental changes by altering transmembrane water and ion fluxes, changing cell volume. Contractile forces generated by actomyosin have been proposed to mechanically regulate cell volume. However, our findings reveal a different mechanism in adherent cells, where elevated actomyosin activity increases cell volume in normal-like cells (NIH 3T3 and others) through interaction with the sodium-hydrogen exchanger isoform 1 (NHE1). This leads to a slow secondary volume increase (SVI) following the initial regulatory volume decrease during hypotonic shock. The active cell response is further confirmed by intracellular alkalinization during mechanical stretch. Moreover, cytoskeletal activation of NHE1 during SVI deforms the nucleus, causing immediate transcriptomic changes and ERK-dependent growth inhibition. Notably, SVI and its associated changes are absent in many cancer cell lines or cells on compliant substrates with reduced actomyosin activity. Thus, actomyosin acts as a sensory element rather than a force generator during adaptation to environmental challenges.

INTRODUCTION

Cells actively control their size during the cell cycle, and failure of cell size control is an indicator of disease.[1–5] Cell size or volume influences all intracellular biochemical reactions by affecting concentrations of cytoplasmic components. During interphase, the cell size steadily increases due to the synthesis of new cytoplasmic components.[6–9] On the other hand, mitotic cells can swell and increase their volume by 10%–20% in minutes without producing extra mass.[10,11] Moreover, short-timescale cell swelling/shrinkage can generate significant mechanical forces,[10,12–14] provide cytoplasmic space for chromosome segregation,[15] and also impact cell migration.[16–19]

At the timescale of minutes, cell volume changes are predominantly due to water flux across the cell membrane, driven by both osmotic and hydraulic pressure gradients.[13,18,20] When the cell size and shape are steady, hydraulic pressure gradients are also mechanically balanced by tension in the cell membrane and the actomyosin cortex.[14] As a consequence, cell volume is sensitive to both environmental physical and chemical variables, including extracellular osmolarity,[1,18,21,22] medium viscosity,[19,23] substrate stiffness or geometry,[24–27] hydraulic resistance,[19,28,29] and mechanical confinement.[30]

To maintain the necessary balance between the osmotic pressure and the hydraulic pressure, cells use transmembrane ion fluxes to change the cytoplasmic solute concentration. Ion "pump and leak" has been identified as a major mechanism in volume regulation,[1,31] involving Na^+ and K^+ fluxes through ion pumps, exchangers, and channels such as sodium-potassium ATPases (NKA) and sodium-hydrogen exchanger (NHE). The latter has been shown to be involved in mitotic swelling and cell migration.[11,16,19] Actomyosin contractile force has been proposed as another way to control cell volume.[12,13,32–35] However, direct evidence showing volume regulation by actomyosin is

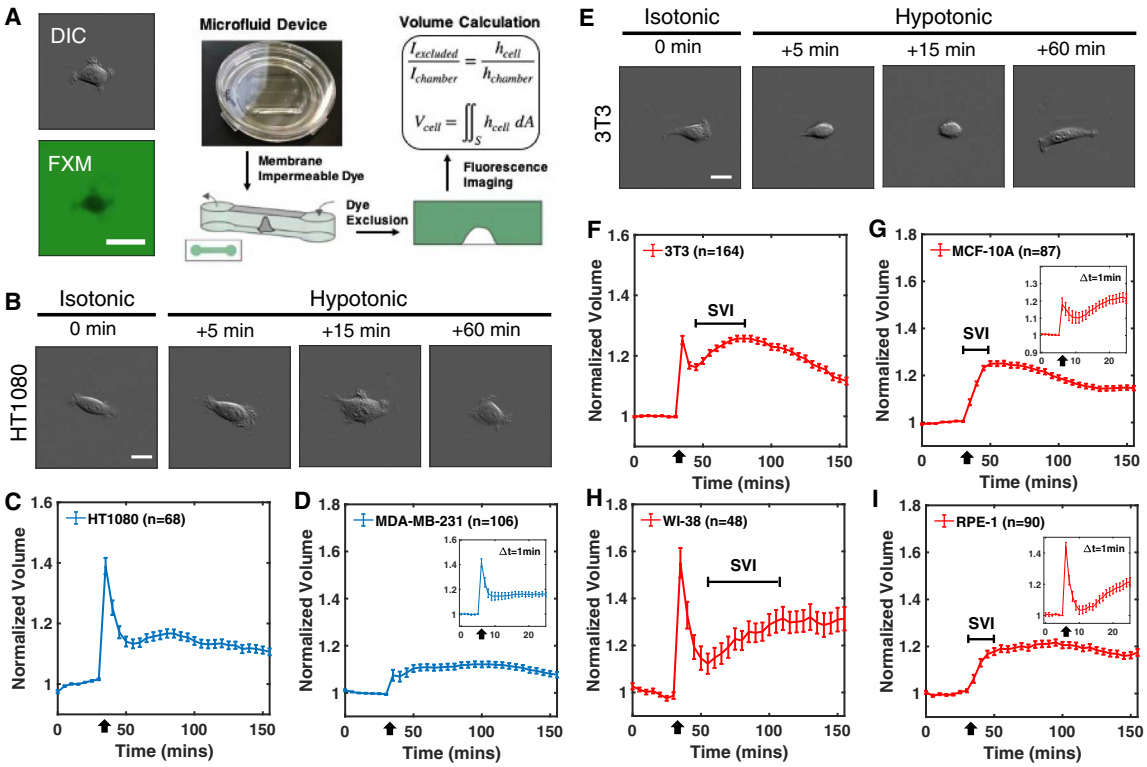

Figure 1. Distinct cell volume dynamics during hypotonic shock

(A) A schematic of the fluorescence exclusion method (FXm) and representative differential interference contrast (DIC) and epifluorescence images.

(B) DIC images of HT1080 cells before and 5, 15, and 60 min after hypotonic shock.

(C and D) Cell volume tracking of HT1080 (C) and MDA-MB-231 (D) cells before and after hypotonic shock. Hypotonic solutions were injected into FXm channels at 30 min. Insets in (D) show volume imaged at a 1 min frame rate for MDA-MB-231 cells (n = 35).

(E) Representative DIC images of NIH 3T3 cells before and 5, 15, and 60 min after hypotonic shock.

(F–I) Cell volume tracking of NIH 3T3 (F), MCF-10A (G), WI-38 (H), and RPE-1 (I) cells before and after hypotonic shock. Insets in (G) and (I) show volume imaged at a 1 min frame rate for MCF-10A (n = 29) and RPE-1 (n = 55) cells, respectively.

(C, D, and F–I) Error bars represent the standard error of the mean (SEM). Statistical tests of all time series plots can be found in Figures S13–S15. Black arrows indicate the time of osmotic shock. (A, B, and E) Scale bars, 20 μm.

lacking. Ca^{2+}-related signaling cascade initiated by mechanosensitive ion channels is a promising candidate that bridges actomyosin contractility with ion transport.[1,36–38] Currently, how cell volume regulation is achieved through actomyosin and Ca^{2+}-mediated signaling is still unclear.

In this work, we investigate the interplay between actomyosin dynamics, Ca^{2+} signaling, and ion fluxes in regulating cell volume. Our findings reveal that different cell types display distinct volume adaptation dynamics during hypotonic stress. We identify a secondary volume increase (SVI) in many normal-like cell lines, such as NIH 3T3 fibroblasts and non-tumorigenic breast MCF-10A cells, after the initial regulatory volume decrease (RVD). The SVI is triggered by cytoskeletal activation of sodium-hydrogen exchanger isoform 1 (NHE1) via Ca^{2+} influx through the mechanosensitive channel Piezo1, actomyosin remodeling, and the NHE1-actin binding partner ezrin. The cytoskeletal activation of NHE1 is also validated by direct mechanical stretching of cells. This mechanism appears to be mostly absent in certain cancer cell types, such as HT1080 fibrosarcoma and MDA-MB-231 metastatic breast cancer cells. Importantly, NIH 3T3 cells lack SVI when plated on compliant substrates, further demonstrating the sensory role of actomyosin in this process. Further explorations reveal that SVI leads to large-scale nuclear deformation and significant changes in the cell transcriptomic and epigenetic landscapes. Specifically, SVI uniquely upregulates phosphatases that inhibit the ERK/mitogen-activated protein kinase (MAPK) signaling pathway, thereby impeding cell growth—a phenomenon that is not observed in cells lacking SVI.

RESULTS

Hypotonic shock triggers non-monotonic cell volume responses

To reveal the cell volume-regulatory system, we applied 50% hypotonic shock as an external perturbation and monitored the subsequent cell volume dynamics using the single-cell tracking fluorescence exclusion method (FXm; Figure 1A).[39,40] We first examined HT1080 fibrosarcoma cells and found that these cells underwent monotonic RVD within 20 min after hypotonic shock, reaching a steady state that is 10% higher than their isotonic volume (Figures 1B and 1C). Hypotonic stress also resulted in a slight increase in HT1080 cell base area without significant cell

shape change (Figures S1A and S1B; Video S1). Similar monotonic RVD with a faster recovery speed was found in MDA-MB-231 breast cancer cells (Figure 1D) and has also been reported recently for HeLa Kyoto cells.[21,22] The RVD showcases the ability of cells to quickly adjust their volume in response to environmental stimuli and has been established as a universal property of mammalian cells.[1,20]

Interestingly, normal-like NIH 3T3 fibroblast cells, during hypotonic shock, displayed a second phase of volume increase after the initial RVD (Figures 1E and 1F). NIH 3T3 cell volume first decreased to a level that was ~18% higher than the baseline isotonic volume after 10 min of hypotonic shock, accompanied by an ~30% base area reduction (Figure S1A) and significant cell rounding (Figures S1B and S1C; Video S2). After that, NIH 3T3 cells showed an SVI, followed by another phase of volume decrease and re-spreading with increased base area. We also conducted an isotonic medium switch and found no volume change (Figure S9A), confirming that the observed SVI is not due to fluid shear stress. This SVI was also found in many other normal-like cell lines, including MCF-10A breast epithelial cells (Figure 1G), WI-38 lung fibroblast cells (Figure 1H), hTERT-immortalized retinal pigmented epithelial (RPE-1) cells (Figure 1I), human embryonic kidney (HEK239A) cells (Figure S1D), and human foreskin fibroblast (HFF-1) cells (Figure S1E), indicating that the SVI is common in many cell types and not an NIH 3T3 cell-specific response. On the other hand, none of the five cancerous cell lines tested (fibrosarcoma HT1080; breast cancer MDA-MB-231, BT-549, and HS578t; and pancreatic ductal adenocarcinoma KPC) exhibited SVI (Figures S9B–S9D). Tracking single-cell volume trajectories, however, revealed significant variations, with all cell lines displaying SVI and monotonic RVD subpopulations (Figures S1F and S1G). The majority of NIH 3T3 and MCF-10A cells displayed the SVI phenotype with varying timescales (on average 45 min for NIH 3T3 and 42 min for MCF-10A cells; Figure S1H) and magnitudes (on average 18% for NIH 3T3 and 30% for MCF-10A cells; Figure S1I). Since the doubling time of NIH 3T3 cells is ~17 h, SVI is not a consequence of cell growth. On the other hand, 60% hypertonic shock resulted in rapid cell volume decrease with a slow regulatory volume increase in both NIH 3T3 and HT1080 cells (Figures S1J and S1K).

Ion pump and leak regulates RVD and SVI

Pump and leak through ion transporters has been implicated as a key mechanism of cell volume regulation,[1,31] and thus we examined its impact on SVI. We first investigated the role of NHE, whose activation leads to an increase of both cell volume and intracellular pH by importing Na^+ and exporting H^+.[41–43] Under isotonic conditions, adding the NHE inhibitor EIPA reduced cell volume in NIH 3T3 but not in HT1080 cells (Figure 2A). During hypotonic shock, HT1080 and MDA-MB-231 cells treated with EIPA displayed a significantly faster RVD (Figures 2B and S2C). This indicates that hypotonicity triggers NHE activation, leading to a cell volume increase that impedes RVD. In NIH 3T3 and MCF-10A cells, EIPA not only increased the speed of RVD but also completely removed the SVI (Figures 2C and S2D). Specifically, we found that the removal of SVI was controlled by NHE1, as confirmed by comparing NHE1 knockdown using RNA interference (shNHE1) with the non-targeting scramble control (SC; Figures 2D and S2F) and the selective NHE1 inhibitor Bix (Figure S2E). We then tracked the relative change of intracellular pH (ΔpH_i), using pHrodo Red-AM[19,44] to assess NHE activity. Upon hypotonic shock, NIH 3T3 cells displayed significant alkalinization that slowly recovered over 40 min, in striking contrast to the immediate decrease and rapid pH recovery found in HT1080 cells (Figure 2E). This alkalinization was abolished upon NHE1 inhibition using Bix (Figure S9E). These results confirm that NHE1 is activated after hypotonic shock and that its activity is sustained during SVI in NIH 3T3 cells, whereas NHE1 activation in HT1080 cells occurs transiently during RVD. Overall, our observations indicate that NHE plays a significant negative role in RVD and that the observed SVI is associated with NHE1 activity.

We next examined NKA, which regulates cell volume decrease by importing 2 K^+ and exporting 3 Na^+,[45] using its inhibitor ouabain (Oua). With a high dosage (250 μM) of Oua, NIH 3T3 cell volume decreased by 20%, while HT1080 cell volume remained the same in isotonic medium (Figure 2A). During hypotonic shock, however, Oua completely removed HT1080 cells' RVD, where its initial cell volume peak (defined as the first measured time point after hypotonic shock) reached 60% higher than its isotonic volume (Figure 2F). HT1080 cell volume continuously increased over the next 2 h, leading to significant cell swelling (Figure 2H; Video S3). Similar results were observed in MDA-MB-231 and MCF-10A cells (Figures S2A and S2B), confirming that NKA is a major contributor to RVD. Blocking NKA also increased the initial cell volume peak of NIH 3T3 cells, but their volume still recovered (Figures 2G and 2I). These markedly different behaviors suggest that completely different cell volume-regulatory mechanisms exist in tissue cells.

We also examined the effects of other key ion transporters in volume regulation, chosen based on their high mRNA levels in both cell lines (Figure S10) and their established role in cell volume regulation.[1] In both NIH 3T3 and HT1080 cells, inhibition of the Na^+-K^+-Cl^- cotransporter (NKCC) using bumetanide (bume; Figures S2G and S2H), the volume-regulated anion channel (VRAC) using DCPIB (Figures S2I and S2J), or Cl^- and HCO_3^- transporters using DIDS (Figures S2M and S2N) had limited impact on the volume dynamics, while blocking the passive voltage-gated K^+ channel (VGKC) using 4-aminopyridine (4-AP) significantly increased the steady-state volume after hypotonic shock (Figures S2K and S2L). However, none of these inhibitors generated a volume change of more than 10% in an isotonic environment (Figure 2A) or changed the features of the monotonic RVD in HT1080 cells or the SVI in NIH 3T3 cells during hypotonic shock.

Theoretical modeling can explain cell-type-specific volume-regulatory behaviors

HT1080 and NIH 3T3 cells display distinct volume adaptation dynamics, both immediately after osmotic change and at longer timescales over tens of minutes. We hypothesize that this is due to distinct ion transporter activities. To identify the ion transporters that are responsible for this distinction, we employed a computational cell homeostasis model that predicts cell volume, membrane potential, pH, and ion dynamics.[42] The model is based on generic biophysical and physiological relationships: (1) the

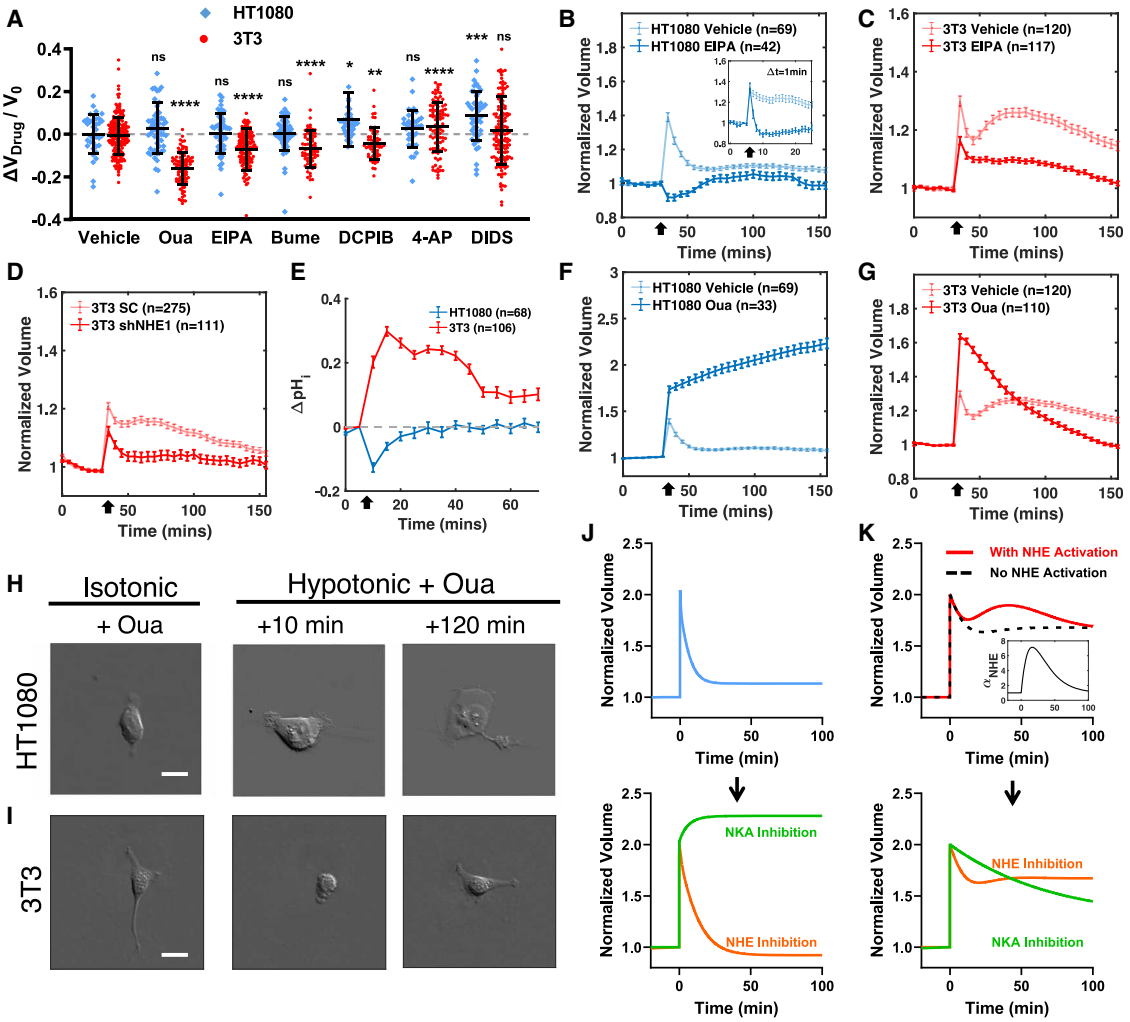

Figure 2. Ion fluxes regulate cell volume dynamics after hypotonic shock

(A) Fractional cell volume change after exposure to ion transporter inhibitors: ouabain (Oua; an NKA inhibitor), EIPA (an NHE inhibitor), bumetanide (bume; an NKCC inhibitor), DCPIB (a VRAC inhibitor), and 4-AP (a VGKC inhibitor). Cell volumes were tracked for 1–4 h until fully adapted (see STAR Methods for details). n_{HT1080} = 36, 60, 50, 61, 47, 36, and 47; n_{3T3} = 213, 94, 147, 76, 62, 100, and 147.

(B and C) EIPA-treated HT1080 (B) and NIH 3T3 (C) cell volume dynamics under hypotonic shock. The inset in (B) shows a 1 min frame rate (vehicle, n = 53; EIPA, n = 25).

(D) NIH 3T3 cell scramble control (SC) and shNHE1 volume dynamics under hypotonic shock.

(E) Relative intracellular pH change (ΔpH_i) for HT1080 and NIH 3T3 cells. Intracellular pH (pH_i) is measured by pHrodo-red AM and calibrated by standard pH buffers. ΔpH_i is calculated by tracking single-cell pH_i. Hypotonic shock was applied at 5 min.

(F and G) Oua-treated HT1080 (F) and NIH 3T3 (G) cell volume under hypotonic shock.

(H and I) Representative DIC images of Oua-treated HT1080 (H) and NIH 3T3 (I) cells before and 10 and 120 min after hypotonic shock.

(J and K) Computer simulation of HT1080 (J) and NIH 3T3 (K) cells with hypotonic shock and inhibition of NKA and NHE. The inset in (K) shows the NHE activation function, where α_{NHE} is the permeability coefficient of NHE.

(A) Error bars indicate standard deviation. Kruskal-Wallis tests followed by Dunn's multiple-comparisons test were conducted between datasets and the vehicle control of the corresponding cell type.

(B–G) Error bars indicate the SEM. Mann-Whitney U tests for two-condition comparisons were conducted at each time point post shock, and p values are plotted as a function of time in Figure S13.

(H and I) Scale bars, 20 μm.

transmembrane water flux is modulated by osmotic and hydrostatic pressure gradients, (2) the transmembrane ion fluxes follow the electro-chemical potential gradients of the ions and are proportional to the activity of the ion transporters, and (3) the intracellular pH is determined by the acid-pair reactions and buffer solutions. Details of the model can be found in the STAR Methods. The generic nature of the model allows it to make predictions for different cell types with different activity levels of ion transporters, as demonstrated in our early work.[42] In this work, we used the same model to identify the ion transporters that give rise to the

specific HT1080 and NIH 3T3 cell volume adaptation dynamics observed in the experiments.

The identification process began with an unbiased random sampling of the activity levels of all eight ion transporters used in the model. We chose a generic activity level from previous estimates[42] and varied the activity levels by 10^{-2} to 10^{2} to account for potential cell-type-specific behavior. The cell volume change after hypotonic shock was modeled using these randomly chosen parameter sets (Figure S11A). We then examined whether the resulting volume dynamics display RVD or SVI, as observed in experiments. Among all randomly searched parameter sets, we indeed found two instances that predict the types of RVD regulations observed in HT1080 and NIH 3T3 cells (Figures 2J and 2K). Principal-component analysis of the parameters identified that NHE and NKA are two key regulators in initial RVD (Figures S11B–S11E), in agreement with the experimental observations. The two sets of parameters also correctly predict the slightly higher homeostatic cytoplasmic pH observed in HT1080 compared to NIH 3T3 cells (Figure S2P).

While the discovered parameters are able to predict the RVD phenotypes associated with HT1080 and NIH 3T3 cells, they do not show SVI no matter what parameters are used. To achieve the SVI observed in NIH 3T3 cells at timescales of tens of minutes, we need to add an additional NHE activation function to the model (Figure 2K). This additional activation is effective and robust in generating the same type of volume increase as the SVI in NIH 3T3 cells (Figure S2O). The need for additional NHE activation raises the question of how NHE is regulated in different cell types and what the purpose of SVI is.

Actomyosin is involved in activating SVI

Hypotonic shock not only alters intracellular osmolarity but also exerts forces on the actomyosin network and the cell membrane by expanding the cell surface.[13] As a consequence, hypotonic stress has been reported to increase cell membrane tension[21] and lead to actin network reorganization.[46] Thus, we examined the F-actin dynamics after hypotonic shock in NIH 3T3 and HT1080 cells stained with the actin probe SPY650-FastAct or transfected with EGFP-F-tractin. Confocal microscopy showed that, in NIH 3T3 cells, F-actin remodeled rapidly and changed the cell shape after osmotic shock (Figures S1B, S1C, and 3A). This was also accompanied by elevated membrane tension, as measured by the membrane tension probe Flipper-TR[21,47] using fluorescence lifetime imaging microscopy (Figures 3D and 3E). The changes in cell shape, actin structure, and high membrane tension were sustained during SVI. Quantitative immunofluorescence (IF) of phosphorylated myosin light chain (pMLC) also showed that NIH 3T3 cell pMLC content increased after hypotonic shock and recovered after 60 min (Figure S3A). In contrast, hypotonic stress neither triggered actin network remodeling in HT1080 cells (Figure 3B) nor induced significant changes in the cell pMLC content (Figure S3B). These observations suggest that NIH 3T3 and HT1080 cells have distinct involvement of actomyosin machinery when responding to hypotonic stress, and we hypothesize that such a difference is related to their distinct volume dynamics.

We then examined whether the observed actomyosin remodeling influences cell volume. The addition of 100 nM actin depolymerizer latrunculin A (LatA) had minimal impact on the cell shape but was sufficient to disrupt the actin network and halted its remodeling after hypotonic shock in NIH 3T3 cells (Figure 3C). While LatA or another actin depolymerizer, cytochalasin D (CytoD), had limited impact on the initial RVD of NIH 3T3 cells (Figures 3F and S3C), the myosin II inhibitor (S)-nitro-blebbistatin (n-Bleb) reduced the initial peak (Figure S3D). Interestingly, all three drugs removed SVI in NIH 3T3 cells. In addition to directly disrupting actomyosin, we inhibited phosphatidylinositol 3-kinase (PI3K) with LY294002 (LY29), known for activating actin protrusions.[48] This treatment similarly reduced the initial peak and abolished SVI in NIH 3T3 cells (Figure 3H). We also validated the effect of LatA in removing SVI in MCF-10A cells (Figure S3E). On the other hand, HT1080 cells treated with LatA still showed limited actin remodeling (Figure S4A), and neither disrupting actomyosin using LatA, CytoD, and n-Bleb nor inhibiting PI3K significantly affected monotonic RVD compared to untreated cells (Figures 3G and S3F–S3H).

Substrate stiffness is known to alter F-actin network structure and change cytoskeletal forces.[49–52] As an independent way to validate the role of actomyosin in SVI, we cultured NIH 3T3 cells on polydimethylsiloxane (PDMS) substrates with varying stiffness and examined cell volume dynamics during hypotonic shock. SVI was observed on both glass surfaces and stiff (130 kPa) substrates. In marked contrast, and in line with our hypothesis, NIH 3T3 cells displayed a monotonic RVD on soft substrates at 3 and 15 kPa (Figure 3I). In addition, hypotonic shock led to transient pH reduction (Figure 3J) and no detectable change of membrane tension (Figure 3E) for NIH 3T3 cells grown on 15 kPa substrates. On the other hand, HT1080 cells displayed a consistent monotonic volume-regulatory decrease regardless of substrate stiffness (Figure S4B). Focal adhesions, known to sense osmotic shock,[1,53] were also investigated for their role in SVI. Inhibiting focal adhesion kinase using PF562271 reduced SVI (Figure S9F). Similarly, cells plated on poly-L-lysine-PEG, which disrupts adhesions and reduces cell spreading,[22] also displayed decreased SVI (Figure S9G). Collectively, we conclude that SVI generation requires cytoskeletal activity and substrate mechanosensation.

Our results demonstrate that SVI requires an active and intact actomyosin network. However, the lack of SVI after actomyosin disruption appears counterintuitive. Disruption of actomyosin reduces the contractile stress and, thus, from the perspective of force balance, should have resulted in a volume increase.[12,13] Contrary to this, pharmacological inhibitions aimed at various components of the actin cytoskeleton or its regulators failed to trigger significant changes in cell volume under isotonic conditions (Figure S4C). This indicates that cell volume is not directly governed by cytoskeletal forces. We observed that LatA treatment lowered the cytoplasmic pH after hypotonic shock in NIH 3T3 cells while having a limited impact on HT1080 cells (Figures 3K and S3I). In addition, NIH 3T3 cells grown on compliant substrates exhibited lower intracellular pH than those grown on glass, implying reduced NHE activity on soft substrates (Figure S4D). These observations suggest that actomyosin remodeling is required for NHE1 activation during SVI, leading us to postulate that actomyosin indirectly regulates the cell volume by mechanically sensing hypotonic stress and signaling

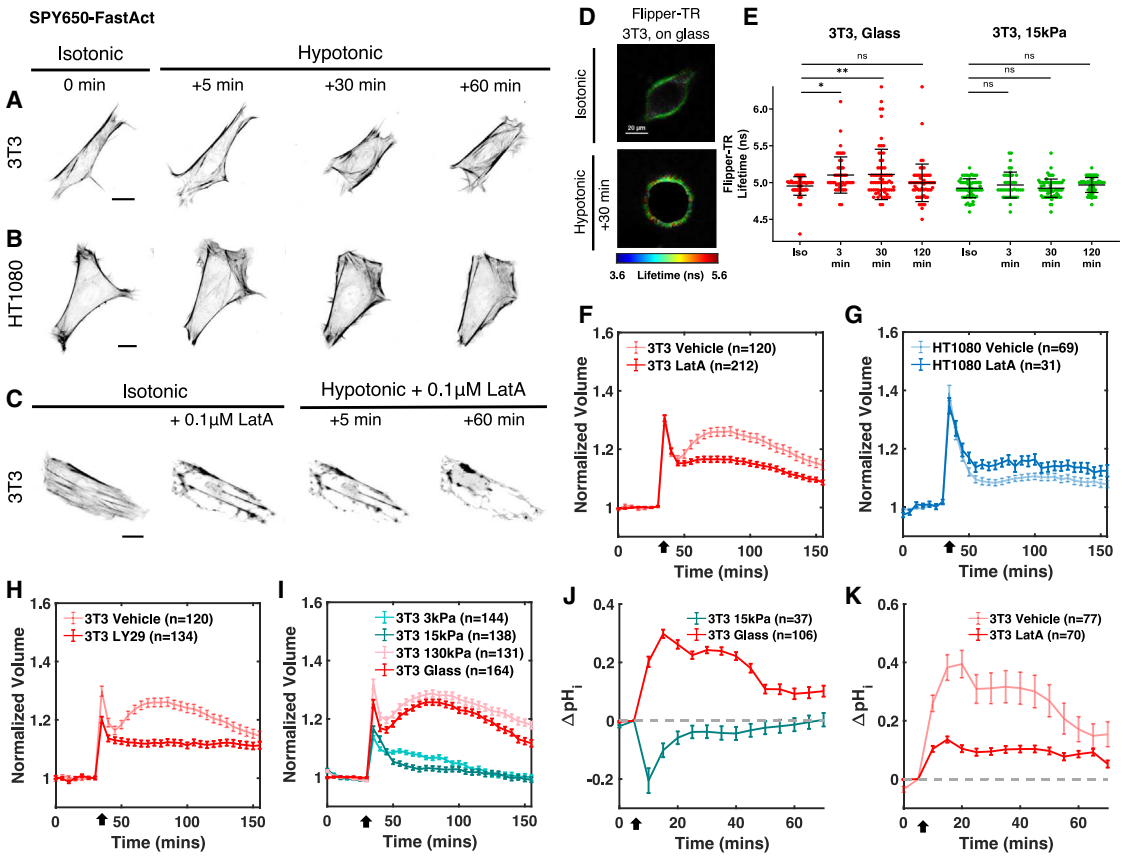

Figure 3. Actomyosin dynamics during hypotonic shock and its activation of SVI

(A–C) Confocal images of NIH 3T3 (A), HT1080 (B), and LatA-treated NIH 3T3 cells (C) stained with the live-cell F-actin probe SPY650-FastAct before and after hypotonic shock.

(D) Representative images showing elevated membrane tension measured by Flipper-TR lifetime during hypotonic shock in NIH 3T3 cells grown on glass.

(E) Membrane tension of NIH 3T3 cells grown on glass and on 15 kPa PDMS substrates before and after 3, 30, or 2 h of hypotonic shock. $n = 61$, 41, 72, and 81 for glass and 25, 18, 27, and 40 for 15 kPa substrates.

(F–H) Volume dynamics of LatA-treated NIH 3T3 (F), LatA-treated HT1080 (G), and LY29-treated NIH 3T3 (H) cells under hypotonic shock.

(I) Volume dynamics of NIH 3T3 cells grown on 3, 15, and 130 kPa PDMS substrates and on glass under hypotonic shock.

(J) ΔpH_i for NIH 3T3 cells grown on 15 kPa substrates versus on glass. Hypotonic shock was applied at 5 min.

(K) ΔpH_i for LatA-treated NIH 3T3 cells versus vehicle control under hypotonic shock.

(F–K) Error bars indicate SEM. Mann-Whitney U tests for two-condition comparisons were conducted at each time point post shock, and p values are plotted as a function of time in Figure S13.

(E) Error bars indicate standard deviation. Kruskal-Wallis tests followed by Dunn's multiple-comparisons test were used.

(A–D) Scale bars, 20 μm.

to NHE1 rather than directly exerting forces on the cell cortex and membrane.[22,34,42]

Mechanosensitive Ca^{2+} signaling regulates cytoskeletal activation of NHE1

To verify our observation that cell volume is regulated by actomyosin-mediated mechanosensation, we examined intracellular Ca^{2+} dynamics, which are known to upregulate myosin activity through Rho kinase and myosin light chain kinase.[54–56] Using the Ca^{2+} indicator GCaMP6s, we observed that NIH 3T3 cells grown on glass immediately exhibited a greater cytosolic Ca^{2+} increase than HT1080 cells after hypotonic shock (Figures 4A and 4B). Soft substrates markedly attenuated such a Ca^{2+} increase in NIH 3T3 cells. Hypotonic shock also triggered more high-frequency Ca^{2+} spikes in NIH 3T3 cells on glass compared to those in HT1080 cells grown on glass (Figures 4C, 4D, S5A, and S5B). Similarly, NIH 3T3 cells on soft substrates exhibited fewer spikes (Figures 4D and S5C). Chelating extracellular Ca^{2+} using BAPTA and intracellular Ca^{2+} using BAPTA-AM (Figures S5D and S5E) as well as blocking mechanosensitive Ca^{2+} channels using $GdCl_3$ or ruthenium red (Figures S5F and S5G) each independently removed SVI and reduced the steady-state cell volume in NIH 3T3 cells. We validated a similar effect of Ca^{2+} channel blocking on removing SVI in MCF-10A cells (Figure S5J). On the other hand, Ca^{2+} channel blockers had limited impact on the RVD response in HT1080 cells (Figures S5K and S5L). These results confirm that Ca^{2+} influx via mechanosensitive ion channels is

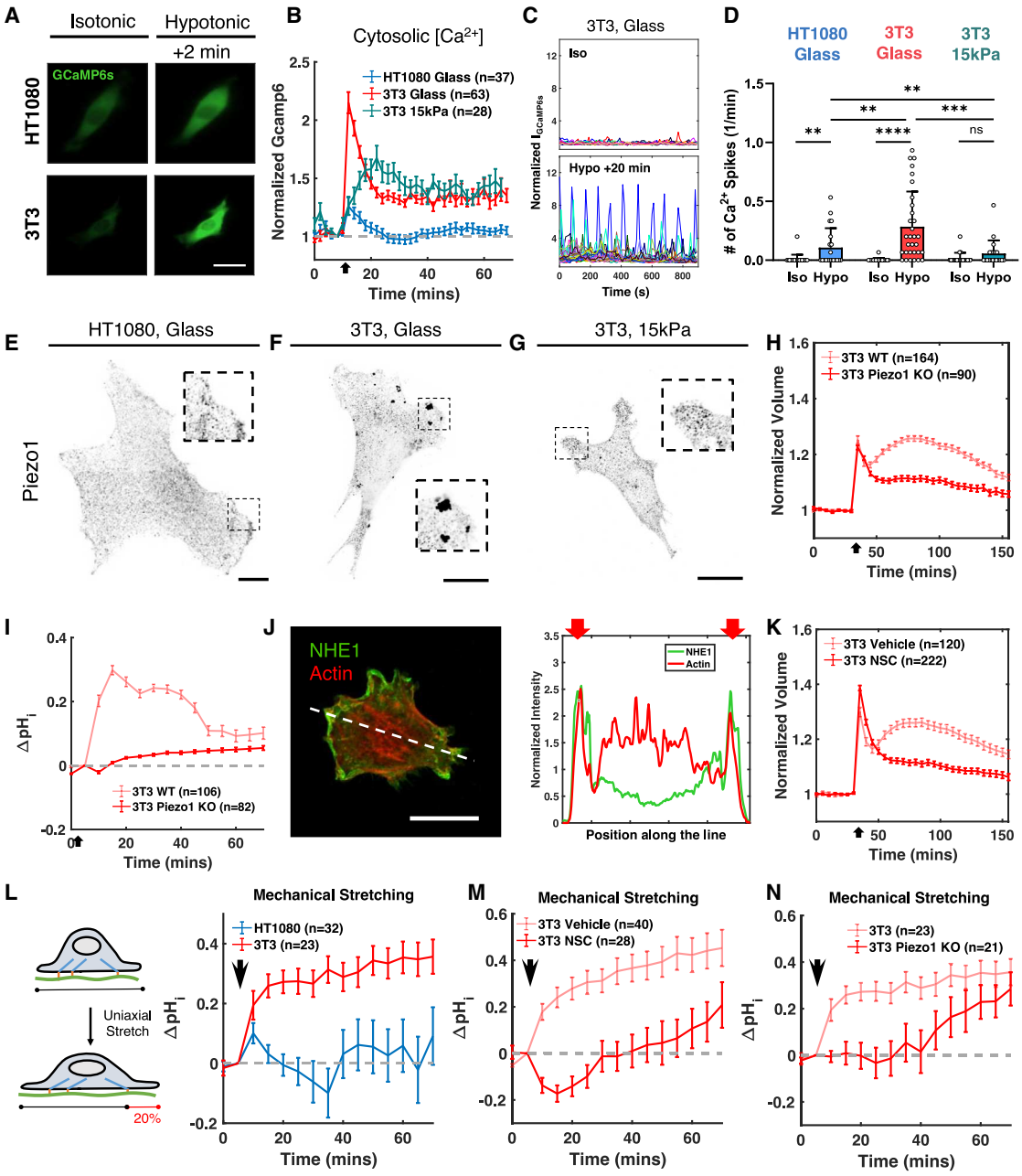

Figure 4. Mechanosensitive Ca^{2+} dynamics regulates cell volume and pH via the actin-NHE1 binding partner ezrin

(A) Representative NIH 3T3 and HT1080 cell GCaMP6s snapshots before and after hypotonic shock.

(B) Cytosolic Ca^{2+} concentration of HT1080 cells grown on glass, NIH 3T3 cells grown on glass, and NIH 3T3 cells grown on 15 kPa PDMS substrates, measured by GCaMP6s intensity under hypotonic shock (applied at 10 min) and imaged at a 2 min frame rate.

(C) NIH 3T3 single-cell GCaMP6s dynamics in isotonic medium (top) and 20 min after hypotonic shock (bottom) on glass, imaged at a 10 s frame rate.

(D) The number of Ca^{2+} spikes in isotonic medium versus 20–40 min under hypotonic shock for each cell type and substrate; defined as at least 2× intensity increase over baseline. n = 26, 20, 18, 31, 21, and 20. Mann-Whitney U tests.

(E–G) Immunostaining of Piezo1 at the basal plane for all cell types and conditions in (D).

(H and I) Volume and ΔpH_i dynamics in NIH 3T3 WT cells and Piezo1 KO cells during hypotonic shock.

(J) Co-staining of NHE1 and actin and their distribution along the line.

(K) NSC-treated NIH 3T3 cell volume dynamics under hypotonic shock.

(L–N) ΔpH_i of NIH 3T3 versus HT1080 (L), NSC-treated NIH 3T3 (M), and NIH 3T3 Piezo1 KO (N) cells under 20% uniaxial mechanical stretch (applied at 5 min).

(legend continued on next page)

essential for generating the SVI and that this mechanism is absent in HT1080 cells.

As one of the most highly expressed Ca^{2+} channels in NIH 3T3 cells (Figure S10), Piezo1 has been shown to regulate the Ca^{2+} influx triggered by membrane surface expansion.[57–59] We thus hypothesize that Piezo1 mediates SVI. Immunostaining of Piezo1 showed that NIH 3T3 cells grown on glass formed dense Piezo1 clusters on the basal plane (Figure 4E). In contrast, HT1080 cells grown on glass and NIH 3T3 cells grown on soft substrates displayed a dispersed Piezo1 localization (Figures 4F and 4G), which is unfavorable for its focal adhesion-dependent activation.[60] CRISPR knockout of Piezo1 in NIH 3T3 cells (NIH 3T3 Piezo1 KO) abolished SVI (Figure 4H) and the intracellular pH decrease (Figure 4I) when subjected to hypotonic shock, suggesting that this molecular intervention suppresses NHE1 activity. To validate the role of Piezo1 in volume regulation, we activated Piezo1 using its agonist Yoda1 when applying hypotonic shock. Both HT1080 and MDA-MB-231 cells displayed faster initial RVD (within 3 min) and SVI (Figures S5H and S5M). Overall, our results indicate that Ca^{2+} influx through the mechanosensitive ion channel Piezo1 is indispensable for SVI during volume regulation triggered by hypotonic stress.

We also asked how actomyosin communicates with NHE1. We hypothesize that the interaction is facilitated by ezrin, which crosslinks F-actin to NHE1 at the cell membrane.[61,62] The co-localization of actin and NHE1 was confirmed by IF co-staining (Figure 4J). Next, we examined whether such binding is required for the NHE1 activation during SVI. Blocking ezrin-actin binding via NSC668394 (NSC) effectively removed SVI (Figure 4K). Interestingly, NSC treatment had limited effects on the initial RVD of NIH 3T3 cells, and its effect in HT1080 cells was also minimal (Figure S6A). The distinct effect of NSC compared to EIPA treatment was in agreement with our conclusion that SVI is triggered by additional NHE1 activation via actomyosin. This is not required for the initial RVD. This conclusion was further corroborated by monitoring the intracellular pH in NIH 3T3 cells, where NSC treatment lowered the pH during SVI without affecting the pH increase during the initial RVD (Figure S6B). Taken together, our results revealed a mechanosensitive regulatory pathway of cell volume: hypotonic stress triggers Ca^{2+} influx through the mechanosensitive ion channel Piezo1, inducing actomyosin remodeling that further activates NHE1 through the actin-NHE1 synergistic binding partner ezrin, leading to SVI.

Similar to hypotonic shock, expanding the cell surface by mechanical stretch has been reported to trigger Ca^{2+} influx through Piezo1,[57] and we postulated that it can also activate NHE1 through the same mechanosensitive pathway. Indeed, applying a one-time 20% uniaxial stretch to NIH 3T3 cells led to an immediate pH increase (Figure 4L). On the contrary, mechanical stretch did not alter the pH in HT1080 cells. Consistent with the hypotonic shock experiments, knocking out Piezo1 or treating NIH 3T3 cells with NSC or LatA abolished or reduced the immediate pH change after mechanical stretch (Figures 4M, 4N, and S6C). These results support the idea that NHE1 can be mechanically activated by Ca^{2+} and the actin cytoskeleton.

Calmodulin (CaM) is a ubiquitous Ca^{2+} receptor that has been shown to bind to NHE1.[36,37,63] To examine whether Ca^{2+}-CaM regulates NHE1 activity, we treated cells with a Ca^{2+}-CaM antagonist, W7. Addition of W7 halted F-actin remodeling during hypotonic shock (Figure S6G). It also markedly accelerated the initial RVD in both NIH 3T3 and HT1080 cells (Figures S6D and S6E). Importantly, W7 treatment, similar to EIPA treatment, abolished SVI and enhanced initial RVD in NIH 3T3 cells. Addition of W7 also significantly lowered the pH in NIH 3T3 cells following hypotonic shock (Figure S6F), indicating that Ca^{2+}-CaM is also required for NHE1 activation.

Cytoskeletal activation of NHE1 deforms the cell nucleus and modifies the transcriptomic profile

Recent studies have revealed the important role of the nucleus in sensing mechanical stimuli.[64–69] To examine whether the cell nucleus responds to hypotonic stress, we simultaneously monitored cell volume and nucleus volume dynamics during hypotonic shock using a recently developed technique, N2FXm (nuclear double fluorescence exclusion method, Figure 5A).[70] In HT1080 cells, hypotonic shock increased the nuclear volume, followed by a monotonic RVD similar to the cell volume (Figure 5B). The nucleus-to-cell volume (N/C) ratio initially increased post shock but recovered during RVD (Figure S7A). In striking contrast, NIH 3T3 cells displayed an SVI-like nucleus volume increase that persisted 2 h post shock (Figure 5B), resulting in a higher N/C ratio (Figure S7A). We hypothesize that this prolonged nucleus deformation is associated with cytoskeleton-mediated NHE1 activation. Supporting this, treatments with EIPA and LatA reduced, and NSC treatment completely abolished, the secondary nuclear volume increase (Figures 5C, S7B, and S7C). These findings together indicate that SVI can decouple the nuclear-to-cell volume scaling and deform the nucleus.

The substantial nucleus deformation observed under hypotonic conditions motivated us to further examine the transcriptomic profiles using RNA sequencing (RNA-seq). Principal-component analysis (PCA) clustered all conditions into 3 transcriptomic states: isotonic, 2 h hypotonic shock, and 24 h hypotonic shock, for the NIH 3T3 and HT1080 cell lines regardless of LatA treatment (Figures 5D and S7D). Differentially expressed genes (DEGs; located with DESeq2 and defined as adjusted $p < 0.05$) between 2 h hypotonic shock and isotonic conditions suggested that NIH 3T3 cells initiated a pronounced, short-timescale transcriptomic response to hypotonic shock that was not observed in HT1080 cells (Figures 5E and 5F), in line with their distinct nucleus shape dynamics. Ingenuity Pathway Analysis (IPA)[71] identified the tumor necrosis factor signaling pathway as the primary upstream pathway responding to hypotonic shock in both NIH 3T3 and HT1080 cells, but the downstream pathways were distinct in each cell line (Figures S7G and S7H). The number of DEGs increased between 24 h after hypotonic shock and

(B, H, I, and K–N) Error bars indicate SEM. Mann-Whitney U tests were used to compare two conditions at each time point after osmotic shock or mechanical stretch, with *p* values plotted in Figure S13.
(D) Error bars indicate standard deviation.
(A, E–G, and J) Scale bars, 20 μm.

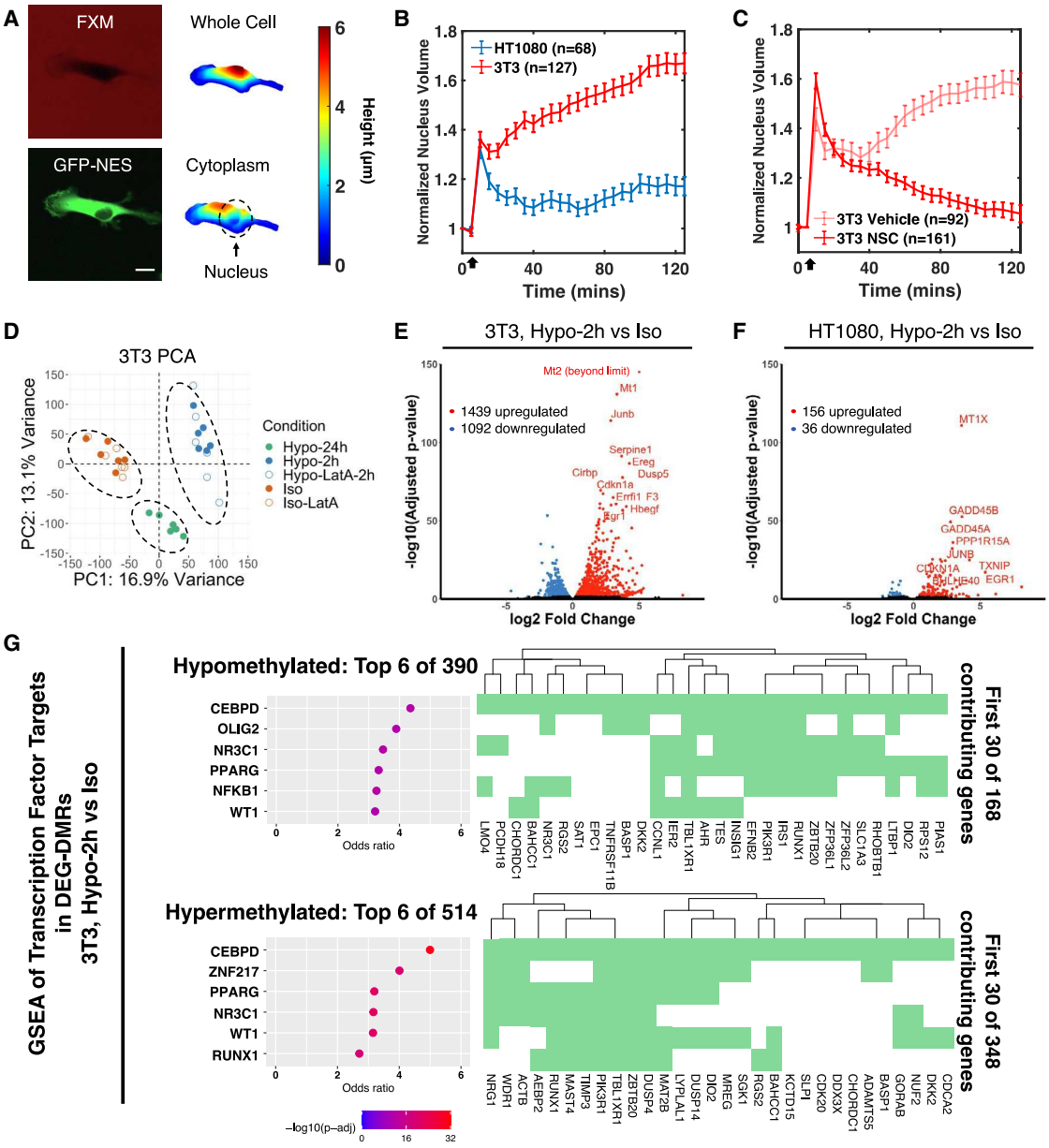

Figure 5. Hypotonic shock deforms the cell nucleus and generates large-scale transcriptional changes

(A) Representative images of N2FXm and 3D reconstructed cell and cytoplasm volumes. Nucleus volume is calculated by subtracting cytoplasm from total cell volume.

(B) Normalized nucleus volume of NIH 3T3 and HT1080 cells following hypotonic shock applied at 5 min.

(C) Normalized nucleus volume of NSC-treated NIH 3T3 cells and vehicle control following hypotonic shock applied at 5 min.

(D) Principal-component analysis (PCA) for NIH 3T3 cells before and after hypotonic shock and with or without LatA treatment. *N* = 3 biological repeats.

(E and F) Volcano plots showing DEGs at 2-h hypotonic shock versus in isotonic medium for NIH 3T3 (E) and HT1080 (F) cells.

(G) Top 6 GSEA terms in the ChEA transcription factor database for genes with hypermethylated (top) and hypomethylated (bottom) DEG-DMRs and top 30 contributing genes (right) at 2-h hypotonic shock versus in isotonic medium for NIH 3T3 cells.

(B and C) Error bars indicate SEM. Mann-Whitney U tests were used to compare two conditions at each time point after osmotic shock, and the *p* values are plotted in Figure S13.

(A) Scale bars, 10 μm.

isotonic conditions for both cell lines (Figures S7E and S7F), indicating that hypotonic shock triggered a long-lasting transcriptomic response.

To further explore how cells regulate their transcriptomic state during hypotonic shock, we examined DNA methylation patterns of NIH 3T3 cells via whole-genome bisulfite sequencing (WGBS).

Similar to RNA expression, PCA of the WGBS data showed clear segregation into isotonic and hypotonic groups regardless of LatA treatment (Figure S8A). Differentially methylated regions (DMRs) were located using DMRseq and filtered to identify DMRs over genes with previously identified DEGs in RNA-seq (termed DEG-DMRs; Figure S8B). This analysis revealed 1,004 DEG-DMRs between isotonic conditions and 2 h hypotonic shock. Gene set enrichment analysis (GSEA) using the ChIP Enrichment Analysis (ChEA) transcription factor database found significant enrichment of genes with DEG-DMRs for targets of over 900 transcription factors (TFs, Figure 5G). Many top targets are known to be involved in hypoxia, including NFKB1, CEBPD, ZNF217, RUNX2, and WT1,[72–76] and some of these TFs themselves (notably NFKB1, CEBPD, and RUNX1) have significantly increased expression during hypotonic shock (Figure S8D). Transcriptional regulation of these TFs and their targets, along with differential DNA methylation at the targets, suggests a robust and highly regulated cellular response to hypotonic shock.

SVI suppresses ERK/MAPK-dependent cell proliferation

We next examined how disrupting SVI using LatA impacted the transcriptome and epigenome. We identified 171 DEGs in NIH 3T3 cells during 2 h hypotonic shock with LatA treatment compared to the untreated cells (Figure 6A). IPA revealed several MAPK/ERK-related upstream pathways as most significantly inhibited by disrupting SVI (Figure 6B). Interestingly, LatA treatment suppressed the upregulation of Dusp2, Dusp5, and Dusp6 observed 2h after hypotonic shock in untreated cells (Figure 6C). These genes encode phosphatases that inactivate ERK1/2,[77] suggesting that ERK inhibition is associated with SVI. On the other hand, HT1080 cell transcriptomics were less sensitive to LatA, and no ERK dependence was observed (Figure S8C). Western blot analysis confirmed that 2 h hypotonic shock reduced ERK phosphorylation in NIH 3T3 wild-type WT cells but not in SVI-deficient NIH 3T3 Piezo1 KO and HT1080 cells (Figure 6D). Overall, these findings underscore a critical connection between SVI and ERK/MAPK activity.

Given that the ERK/MAPK signaling pathway is a critical controller of cell proliferation,[78] we further examined how SVI affected cell proliferation. GSEA identified significant enrichment of targets of ERK-related transcription factors in genes with DEG-DMRs between cells treated and not treated with LatA after 2 h hypotonic shock (Figure 6F). Among them, WT1 has recently been identified to upregulate ERK/MAPK activity and cell proliferation,[79] while ELK1 and STAT3 are direct downstream targets of ERK/MAPK that have been shown to control cell growth.[80,81] We then used IF to examine the proliferation marker Ki-67[82] and quantify cell proliferation by calculating the fraction of Ki-67-active cells. The fraction of Ki-67-active NIH 3T3 WT cells decreased significantly after 6 h of hypotonic shock. The reduced proliferative potential cannot be further suppressed by ERK inhibition using trametinib (Trame; Figure 6E). On the contrary, NIH 3T3 Piezo1 KO and HT1080 cells maintained higher proliferation activities in hypotonic medium, which were abolished by ERK inhibition. Taken together, our results revealed that SVI was a suppressor of ERK/MAPK-mediated cell proliferation in response to hypotonic stress.

DISCUSSION

Recent studies have revealed the importance of physical variables such as adhesions and forces in cell size regulation. However, except for a WNK-activated Cl^- secretion mechanism identified during hypertonic volume decrease,[83] a detailed mechanism of how cells regulate volume during hypotonic expansion has yet to be revealed. In this study, we showed that the initial phase of rapid RVD during hypotonic stress can be explained by rapid actions of ion channels/pumps. However, cells can further regulate their volume by mechanically activating NHE1 through a signaling cascade involving Ca^{2+}, actomyosin, and ezrin (Figure 6F), generating SVI and increasing intracellular pH. SVI is largely found in normal-like cell types but absent in HT1080 and MDA-MB-231 cancer cells, suggesting that differential mechanisms of volume and pH regulation may be a defining feature of transformed and malignant cells. Moreover, the absence of SVI-induced ERK inhibition might facilitate cell proliferation in response to external cues, especially given that ERK-mediated cell proliferation serves as a cancer marker.[78,84] While links between mechanosensation, osmoregulation, and cancer have been established previously,[85–87] the underlying mechanisms remain largely unexplored. Our findings related to SVI and cytoskeletal activation of NHE1 offer a potential bridge between mechanosensation and osmoregulation that could explain the reduced sensitivity of cancer cells under environmental stimuli.

Cell volume regulation is a classic problem and has been investigated extensively for nearly a century.[1,20,31,88] Cell volume regulation impacts cell mechanical behavior[13] and therefore influences cell shape, migration, and morphogenesis. It is now increasingly understood as being controlled by a complex network that integrates ion dynamics, cell mechanics, and metabolic activities.[13,42,85] This system incorporates multiple feedback and compensatory mechanisms. Thus, disruptions in ion transporter activity might not straightforwardly align with their molecular roles. For instances, while inhibiting NKA is traditionally thought to trap intracellular Na^+ and increase cell volume, reports vary, showing no change or even a volume decrease (Figure 2A).[31] The volume-regulatory network is also cell type specific, which might explain the varied cell volume responses to pharmacological/environmental challenges observed across studies. Additionally, phenotypic heterogeneity within each cell types requires measuring many volume trajectories to accurately capture response dynamics. Volume discrepancies can also arise from measurement methodologies. Classical methods like Coulter counters assess population averages on detached cells, which regulate volume differently than adherent cells.[25,26,89] While cell area might be a proxy for volume in suspended, rounded cells, this is invalid in adherent cells. Methodological variations might account for some studies failing to observe SVI in NIH 3T3 cells.[90] Nevertheless, SVI-like volume trajectories have been noted elsewhere but have not been investigated explicitly.[21,91] Similarly, studies reporting unrecovered volume post hypotonic shock[1] might also be explained by SVI, suggesting a broader relevance of this phenomenon than recognized previously.

Our findings highlight the critical role of Ca^{2+} in regulating cell volume and pH, despite its low concentration in the cytoplasm,

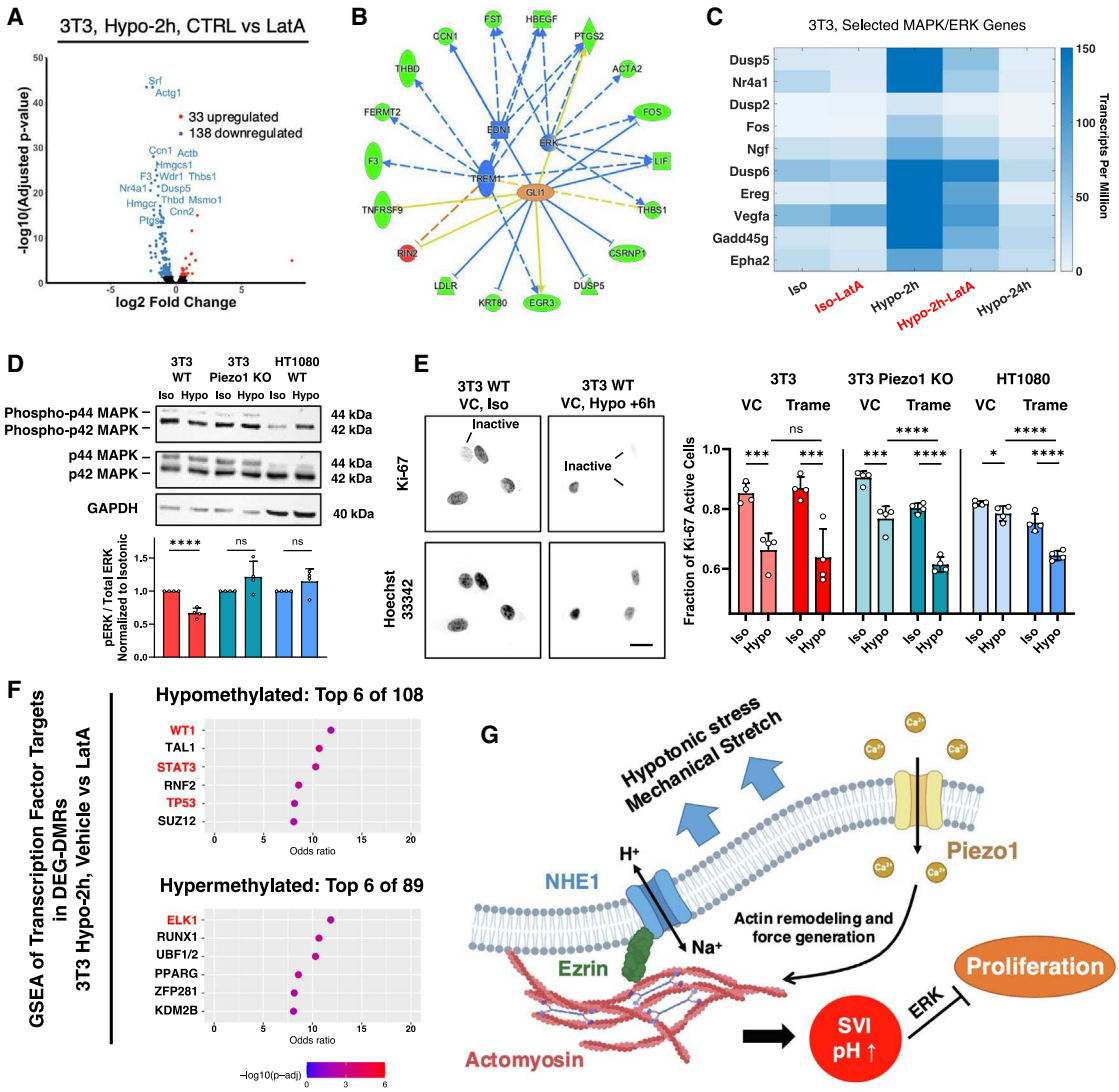

Figure 6. SVI suppress ERK/MAPK dependent cell proliferation

(A) Volcano plots showing DEGs under 2-h hypotonic shock between LatA-treated NIH 3T3 cells and vehicle control.

(B) Top 4 upstream pathways identified by IPA in NIH 3T3 cells under 2-h hypotonic shock with and without LatA treatment. Red/green indicate increased/decreased measurements, and orange/blue indicate predicated activation/deactivation.

(C) Gene heatmap showing expression of MAPK/ERK pathway genes identified in (B).

(D) Western blot for phospho-ERK and total ERK of NIH 3T3 WT, NIH 3T3 Piezo1 KO, and HT1080 cells, with quantification of phospho-ERK/total ERK ratio. $N = 4$ biological replicates. Student's t test.

(E) Images and quantification of Ki-67-active cells under isotonic conditions and after 6 h of hypotonic shock with and without Trame treatment in NIH 3T3 WT, NIH 3T3 Piezo1 KO, and HT1080 cells. $N = 4$ biological replicates, and >200 cells were examined in each repeat.

(F) Top 6 GSEA terms in the ChEA transcription factor database for genes with hypermethylated (top) and hypomethylated (bottom) DEG-DMRs at 2-h hypotonic shock with and without LatA treatment in NIH 3T3 cells.

(G) Schematic of the proposed cytoskeletal activation of the NHE1 pathway.

(D and E) Error bars indicate standard deviation. Mann-Whitney U tests.

(E) Scale bars, 20 μm.

through both direct binding and activation of NHE1 via CaM and induction of actomyosin remodeling that indirectly activates NHE1 via ezrin. Interestingly, disrupting the actin network or blocking actin-ezrin binding had limited impact on isotonic cell volume (Figure S4C), suggesting that the cytoskeletal activation of NHE1 observed during SVI and mechanical stretch is a regulatory response to environmental changes rather than a continuous process during stationary cell culture. Since cells in physiological settings likely experience varying osmolarity, pressure, and mechanical force, the mechanosensory system uncovered here is a critical link that connects environmental mechanical cues with cell growth and proliferation.

The magnitude and timescale of the observed SVI and the corresponding shape change (rounding up) in NIH 3T3 cells are surprisingly similar to mitotic cell swelling, a phenomenon that has been shown to be regulated by actomyosin and NHE.[10–12] This correspondence suggests that cells potentially regulate their mitotic entry through Ca^{2+}-mediated mechanosensation to ion channels/transporters. Nucleus deformation associated with NHE-mediated swelling maybe important for successful mitosis. This hypothesis should be examined in future work, although we note that, in HT1080 cells that lack SVI, mitotic swelling is still present. In addition, a series of recent works has shown that water flux driven by ion transport is responsible for cell migration in 1D confinement and 2D environments and that NHE is one of the central players activated by actomyosin dynamics.[16,18,19,23] While NHE-mediated proton concentration itself is not an appreciable contributor to cell osmolarity, it can affect HCO_3^- concentration on the order of ~10 mM through its equilibrium with CO_2.[42] These results establish that cell volume dynamics are associated with cell migration and that the mechanosensitive activation of NHE1 is another way for cells to generate protrusions and motility. Actin and myosin serve as sensory and control elements during this type of protrusion, but forces are generated by NHE1-mediated water influx to propel the cell.[16,42] Last, we observed a negative correlation between cytoskeletal activation of NHE1 and ERK activity. However, this relationship is complex, with some reports suggesting a positive feedback loop between NHE1 and ERK.[92–94] Given PI3K's role in SVI and its interactions with the ERK/MAPK pathway,[95] future studies should explore the intricate NHE1-ERK-PI3K interactions in response to external stimuli.

Limitations of the study

This study reveals complex cell volume and pH responses to physical cues and pharmacological treatments, suggesting multiple underlying regulatory pathways regulating SVI that have yet to be fully elucidated. For example, crosstalk between microtubules and the mTorc pathway has been reported to mediate cell volume under osmotic pressure and curvature of the substrates,[21,27] which may contribute to SVI. The pH dependency of actin cytoskeleton dynamics[62,96,97] hints at a feedback loop from NHE1 to actin that was not explored in this work. We also do not fully understand the molecular mechanism of the SVI regulation by focal adhesion and mechanosensation of the extracellular matrix. Similarly, we do not fully understand the molecular and structural details of NHE1 activation by cytoskeletal activity. In addition, while we identified the importance of stretch-activated channel Piezo1 in cell volume regulation, the roles of other mechanosensitive Ca^{2+} channels or store-operated channels are unknown. Last, the mechanisms of how the cytoskeleton and NHE1 mediate sustained nuclear volume changes under hypotonic conditions remain unclear.

RESOURCE AVAILABILITY

Lead contact

Requests for further information and resources should be directed to and will be fulfilled by the lead contact, Sean X. Sun (ssun@jhu.edu).

Materials availability

This study did not generate new unique reagents.

Data and code availability

- RNA-seq data are publicly available in the NCBI Sequence Read Archive (SRA) as NCBI: PRJNA1175048.
- Codes for data analysis are available at GitHub (https://github.com/sxslabjhu/GeneralDataProcessing) and have been archived at Zenodo (https://doi.org/10.5281/zenodo.13958563).
- Any additional information required to reanalyze the data reported in this paper is available from the lead contact upon request.

ACKNOWLEDGMENTS

We would like to thank Ikbal Choudhury, Shaozheng Sun, Bin Sheng Wong, Wenxuan Du, and Rong Li for their help with experiments and discussions. This work was supported in part by NIH R01 GM134542 and R01 CA254193 (S.X.S. and K.K.), NSF 2303648 (Y.L.), NIH R35 GM147274 (D. L. and Y. Y.), and Kavli Neuroscience Discovery Institute Distinguished Graduate Fellowship (Y. Y.). G.S. and A.P.F acknowledge support from Bloomberg Philanthropies. We also thank the John Hopkins University Integrated Imaging Center for microscope support and Rockfish HPC for computational sources.

AUTHOR CONTRIBUTIONS

Q.N., K.K., and S.X.S. conceptualized and designed the study. Q.N., Z.G., and J.F. conducted all live-cell experiments and analyzed the data (with Y. Wu). Y.L. and S.X.S. developed the cell volume model and analyzed the simulation results (with Q.N.). Z.G., Y. Yang, A.C.N.V., and Y. Wang generated and validated the CRISPR Piezo1 knockout cell line, K.B. and A.S. generated and validated the shNHE1 cell lines, and Y. Yan and D.L. generated NES cell lines. Q.N., Z.G., A.S., and Y. Yang conducted immunofluorescence and western blots. G.S. and A.P.F. conducted and performed analysis for RNA-seq and WGBS (with Q.N.). Q.N. and S.X.S. wrote the manuscript, and Z.G., J.F., Y.L., G.S., K.B., A.S., A.P.F., and K.K. edited the manuscript.

DECLARATION OF INTERESTS

The authors declare no competing interests.

STAR★METHODS

Detailed methods are provided in the online version of this paper and include the following:

- KEY RESOURCES TABLE
- EXPERIMENTAL MODEL AND STUDY PARTICIPANT DETAILS
  - Cell culture
- METHOD DETAILS
  - Osmotic shock media preparation, and pharmacological inhibitors
  - Microfluidic device fabrication
  - Cell volume tracking during pharmacological inhibition and osmotic shock experiment
  - Data analysis and cell volume calculation in fluorescence exclusion method
  - Benchmarking cell volume measurement using FXm
  - Nucleus volume measurement using N2FXm
  - Epi-fluorescence and confocal microscopy
  - Measurement of membrane tension using fluorescence lifetime imaging microscopy and Flipper-TR
  - PDMS substrates fabrication
  - Live cell reporters, cloning, lentivirus preparation, transduction, and transfection
  - CRISPR knockout
  - Immunofluorescence and image analysis
  - Western blot
  - Intracellular pH measurement

SUPPLEMENTAL INFORMATION

Supplemental information can be found online at https://doi.org/10.1016/j.celrep.2024.114992.

Received: May 22, 2024
Revised: September 24, 2024
Accepted: November 4, 2024

REFERENCES

1. Hoffmann, E.K., Lambert, I.H., and Pedersen, S.F. (2009). Physiology of cell volume regulation in vertebrates. Physiol. Rev. *89*, 193–277.
2. Ginzberg, M.B., Kafri, R., and Kirschner, M. (2015). On being the right (cell) size. Science *348*, 6236.
3. Hung, J.T., Nelliat, A.R., Choudhury, M.I., Kucharavy, A., Bradford, W.D., Cook, M.E., Kim, J., Mair, D.B., Sun, S.X., Schatz, M.C., and Li, R. (2019). Hypo-osmotic-like stress underlies general cellular defects of aneuploidy. Nature *570*, 117–121.
4. Neurohr, G.E., Terry, R.L., Lengefeld, J., Bonney, M., Brittingham, G.P., Moretto, F., Miettinen, T.P., Vaites, L.P., Soares, L.M., Paulo, J.A., et al. (2019). Excessive Cell Growth Causes Cytoplasm Dilution And Contributes to Senescence. Cell *176*, 1083–1097.e18.
5. Lanz, M.C., Zatulovskiy, E., Swaffer, M.P., Zhang, L., Ilerten, I., Zhang, S., You, D.S., Marinov, G., McAlpine, P., Elias, J.E., and Skotheim, J.M. (2022). Increasing cell size remodels the proteome and promotes senescence. Mol. Cell. *82*, 3255–3269.e8.
6. Cadart, C., Monnier, S., Grilli, J., Sáez, P.J., Srivastava, N., Attia, R., Terriac, E., Baum, B., Cosentino-Lagomarsino, M., and Piel, M. (2018). Size control in mammalian cells involves modulation of both growth rate and cell cycle duration. Nat. Commun. *9*, 3275.
7. Wu, Y., Pegoraro, A.F., Weitz, D.A., Janmey, P., and Sun, S.X. (2022). The correlation between cell and nucleus size is explained by an eukaryotic cell growth model. PLoS Comput. Biol. *18*, e1009400.
8. Rollin, R., Joanny, J.-F., and Sens, P. (2023). Physical basis of the cell size scaling laws. Elife *12*, e82490.
9. Liu, X., Yan, J., and Kirschner, M.W. (2024). Cell size homeostasis is tightly controlled throughout the cell cycle. PLoS Biol. *22*, e3002453.
10. Zlotek-Zlotkiewicz, E., Monnier, S., Cappello, G., Le Berre, M., and Piel, M. (2015). Optical volume and mass measurements show that mammalian cells swell during mitosis. J. Cell Biol. *211*, 765–774.
11. Son, S., Kang, J.H., Oh, S., Kirschner, M.W., Mitchison, T.J., and Manalis, S. (2015). Resonant microchannel volume and mass measurements show that suspended cells swell during mitosis. J. Cell Biol. *211*, 757–763.
12. Stewart, M.P., Helenius, J., Toyoda, Y., Ramanathan, S.P., Muller, D.J., and Hyman, A.A. (2011). Hydrostatic pressure and the actomyosin cortex drive mitotic cell rounding. Nature *469*, 226–230.
13. Jiang, H., and Sun, S.X. (2013). Cellular pressure and volume regulation and implications for cell mechanics. Biophys. J. *105*, 609–619.
14. Tao, J., and Sun, S.X. (2015). Active Biochemical Regulation of Cell Volume and a Simple Model of Cell Tension Response. Biophys. J. *109*, 1541–1550.
15. Lancaster, O.M., Le Berre, M., Dimitracopoulos, A., Bonazzi, D., Zlotek-Zlotkiewicz, E., Picone, R., Duke, T., Piel, M., and Baum, B. (2013). Mitotic rounding alters cell geometry to ensure efficient bipolar spindle formation. Dev. Cell *25*, 270–283.
16. Stroka, K.M., Jiang, H., Chen, S.H., Tong, Z., Wirtz, D., Sun, S.X., and Konstantopoulos, K. (2014). Konstantinos Konstantopoulos. Water permeation drives tumor cell migration in confined microenvironments. Cell *157*, 611–623.
17. Tao, J., Li, Y., Vig, D.K., and Sun, S.X. (2017). Cell mechanics: A dialogue. Rep. Prog. Phys. *80*, 36601.
18. Li, Y., Konstantopoulos, K., Zhao, R., Mori, Y., and Sun, S.X. (2020). The importance of water and hydraulic pressure in cell dynamics. J. Cell Sci. *133*, jcs240341.
19. Bera, K., Kiepas, A., Godet, I., Li, Y., Mehta, P., Ifemembi, B., Paul, C.D., Sen, A., Serra, S.A., Stoletov, K., et al. (2022). Extracellular fluid viscosity enhances cell migration and cancer dissemination. Nature *611*, 365–373.
20. Cadart, C., Venkova, L., Recho, P., Lagomarsino, M.C., and Piel, M. (2019). The physics of cell-size regulation across timescales. Nat. Phys. *15*, 993–1004.
21. Roffay, C., Molinard, G., Kim, K., Urbanska, M., Andrade, V., Barbarasa, V., Nowak, P., Mercier, V., García-Calvo, J., Matile, S., et al. (2021). Passive coupling of membrane tension and cell volume during active response of cells to osmosis. Proc. Natl. Acad. Sci. USA *118*, e2103228118.
22. Venkova, L., Vishen, A.S., Lembo, S., Srivastava, N., Duchamp, B., Ruppel, A., Williart, A., Vassilopoulos, S., Deslys, A., Garcia Arcos, J.M., et al. (2022). A mechano-osmotic feedback couples cell volume to the rate of cell deformation. Elife *11*, e72381.
23. Maity, D., Bera, K., Li, Y., Ge, Z., Ni, Q., Konstantopoulos, K., and Sun, S.X. (2022). Extracellular Hydraulic Resistance Enhances Cell Migration. Adv. Sci. *9*, 2200927.
24. Perez Gonzalez, N., Tao, J., Rochman, N.D., Vig, D., Chiu, E., Wirtz, D., and Sun, S.X. (2018). Cell tension and mechanical regulation of cell volume. Mol. Biol. Cell *29*, 2600.
25. Guo, M., Pegoraro, A.F., Mao, A., Zhou, E.H., Arany, P.R., Han, Y., Burnette, D.T., Jensen, M.H., Kasza, K.E., Moore, J.R., et al. (2017). Cell volume change through water efflux impacts cell stiffness and stem cell fate. Proc. Natl. Acad. Sci. USA *114*, E8618–E8627.
26. Xie, K., Yang, Y., and Jiang, H. (2018). Controlling Cellular Volume via Mechanical and Physical Properties of Substrate. Biophys. J. *114*, 675–687.
27. Tomba, C., Luchnikov, V., Barberi, L., Blanch-Mercader, C., and Roux, A. (e5, may 2022). Epithelial cells adapt to curvature induction via transient active osmotic swelling. Dev. Cell *57*, 1257–1270.e5.
28. Hui, T.H., Zhou, Z.L., Qian, J., Lin, Y., Ngan, A.H.W., and Gao, H. (2014). Volumetric deformation of live cells induced by pressure-activated cross-membrane ion transport. Phys. Rev. Lett. *113*, 118101–118105.
29. Park, J., Jia, S., Salter, D., Bagnaninchi, P., and Hansen, C.G. (2022). The Hippo pathway drives the cellular response to hydrostatic pressure. EMBO J. *41*, e108719.
30. Watkins, S., and Sontheimer, H. (2011). Hydrodynamic cellular volume changes enable glioma cell invasion. J. Neurosci. *31*, 17250–17259.
31. Tosteson, D.C., and Hoffman, J.F. (1960). Regulation of cell volume by active cation transport in high and low potassium sheep red cells. J. Gen. Physiol. *44*, 169–194.
32. Cantiello, H.F. (1997). Role of actin filament organization in cell volume and ion channel regulation. J. Exp. Zool. *279*, 425–435.
33. Henson, J.H. (1999). Relationships between the actin cytoskeleton and cell volume regulation. Microsc. Res. Tech. *47*, 155–162.
34. Adar, R.M., and Safran, S.A. (2020). Active volume regulation in adhered cells. Proc. Natl. Acad. Sci. USA *117*, 5604–5609.

35. Adar, R.M., Vishen, A.S., Joanny, J.-F., Sens, P., and Safran, S.A. (2023). Volume regulation in adhered cells: Roles of surface tension and cell swelling. Biophys. J. *122*, 506–512.

36. Li, X., Prins, D., Michalak, M., and Fliegel, L. (2013). Calmodulin-dependent binding to the NHE1 cytosolic tail mediates activation of the Na+/H+ exchanger by Ca2+ and endothelin. Am. J. Physiol. Cell Physiol. *305*, 1161–1169.

37. Sjøgaard-Frich, L.M., Prestel, A., Pedersen, E.S., Severin, M., Kristensen, K.K., Olsen, J.G., Kragelund, B.B., and Pedersen, S.F. (2021). Dynamic Na+/H+ exchanger 1 (NHE1) - calmodulin complexes of varying stoichiometry and structure regulate Ca2+-dependent NHE1 activation. Elife *10*, e60889.

38. He, L., Tao, J., Maity, D., Si, F., Wu, Y., Wu, T., Prasath, V., Wirtz, D., and Sun, S.X. (2018). Role of membrane-tension gated Ca 2+ flux in cell mechanosensation. J. Cell Sci. *131*. jcs208470-12.

39. Cadart, C., Zlotek-Zlotkiewicz, E., Venkova, L., Thouvenin, O., Racine, V., Le Berre, M., Monnier, S., and Piel, M. (2017). Fluorescence eXclusion Measurement of volume in live cells. Methods Cell Biol. *139*, 103–120.

40. Rochman, N.D., Yao, K., Gonzalez, N.P.A., Wirtz, D., and Sun, S.X. (2020). Single Cell Volume Measurement Utilizing the Fluorescence Exclusion Method (FXm). Bio. Protoc. *10*, e3652.

41. Jentsch, T.J. (2016). VRACs and other ion channels and transporters in the regulation of cell volume and beyond. Nat. Rev. Mol. Cell Biol. *17*, 293–307.

42. Li, Y., Zhou, X., and Sun, S.X. (2021). Hydrogen, Bicarbonate, and Their Associated Exchangers in Cell Volume Regulation. Front. Cell Dev. Biol. *9*, 683686.

43. Nagy, T.L., Strickland, E., and Weiner, O.D. (2024). Neutrophils actively swell to potentiate rapid migration. Elife *12*.

44. Kemmer, G.C., Ammitzbøll Bogh, S., Urban, M., Palmgren, M.G., Vosch, T., Schiller, J., and Günther Pomorski, T. (2015). Lipid-conjugated fluorescent pH sensors for monitoring pH changes in reconstituted membrane systems. Analyst *140*, 6313–6320.

45. Pivovarov, A.S., Calahorro, F., and Walker, R.J. (2019). Na+/K+-pump and neurotransmitter membrane receptors. Invertebr. Neurosci. *19*, 1.

46. Guilak, F., Erickson, G.R., and Ting-Beall, H.P. (2002). The effects of osmotic stress on the viscoelastic and physical properties of articular chondrocytes. Biophys. J. *82*, 720–727.

47. Colom, A., Derivery, E., Soleimanpour, S., Tomba, C., Molin, M.D., Sakai, N., González-Gaitán, M., Matile, S., and Roux, A. (2018). A fluorescent membrane tension probe. Nat. Chem. *10*, 1118–1125.

48. De Belly, H., Yan, S., Borja da Rocha, H., Ichbiah, S., Town, J.P., Zager, P.J., Estrada, D.C., Meyer, K., Turlier, H., Bustamante, C., and Weiner, O.D. (2023). Cell protrusions and contractions generate long-range membrane tension propagation. Cell *186*, 3049–3061.e15.

49. Yeung, T., Georges, P.C., Flanagan, L.A., Marg, B., Ortiz, M., Funaki, M., Zahir, N., Ming, W., Weaver, V., and Janmey, P.A. (2005). Effects of substrate stiffness on cell morphology, cytoskeletal structure, and adhesion. Cell Motil Cytoskeleton *60*, 24–34.

50. Ghibaudo, M., Saez, A., Trichet, L., Xayaphoummine, A., Browaeys, J., Silberzan, P., Buguin, A., and Ladoux, B. (2008). Traction forces and rigidity sensing regulate cell functions. Soft Matter *4*, 1836.

51. Walcott, S., and Sun, S.X. (2010). A mechanical model of actin stress fiber formation and substrate elasticity sensing in adherent cells. Proc. Natl. Acad. Sci. USA *107*, 7757–7762.

52. Isomursu, A., Park, K.Y., Hou, J., Cheng, B., Mathieu, M., Shamsan, G.A., Fuller, B., Kasim, J., Mahmoodi, M.M., Lu, T.J., et al. (2022). Directed cell migration towards softer environments. Nat. Mater. *21*, 1081–1090.

53. Schwartz, M.A., and DeSimone, D.W. (2008). Cell adhesion receptors in mechanotransduction. Curr. Opin. Cell Biol. *20*, 551–556.

54. Scholey, J.M., Taylor, K.A., and Kendrick-Jones, J. (1980). Regulation of non-muscle myosin assembly by calmodulin-dependent light chain kinase. Nature *287*, 233–235.

55. Uehata, M., Ishizaki, T., Satoh, H., Ono, T., Kawahara, T., Morishita, T., Tamakawa, H., Yamagami, K., Inui, J., Maekawa, M., and Narumiya, S. (1997). Calcium sensitization of smooth muscle mediated by a Rho-associated protein kinase in hypertension. Nature *389*, 990–994.

56. Sakurada, S., Takuwa, N., Sugimoto, N., Wang, Y., Seto, M., Sasaki, Y., and Takuwa, Y. (2003). Ca2+-dependent activation of Rho and Rho kinase in membrane depolarization-induced and receptor stimulation-induced vascular smooth muscle contraction. Circ. Res. *93*, 548–556.

57. Miyamoto, T., Mochizuki, T., Nakagomi, H., Kira, S., Watanabe, M., Takayama, Y., Suzuki, Y., Koizumi, S., Takeda, M., and Tominaga, M. (2014). Functional role for Piezo1 in stretch-evoked Ca2+ influx and ATP release in Urothelial cell cultures. J. Biol. Chem. *289*, 16565–16575.

58. Cahalan, S.M., Lukacs, V., Ranade, S.S., Chien, S., Bandell, M., and Patapoutian, A. (2015). Piezo1 links mechanical forces to red blood cell volume. Elife *4*, e07370.

59. Yang, S., Miao, X., Arnold, S., Li, B., Ly, A.T., Wang, H., Wang, M., Guo, X., Pathak, M.M., Zhao, W., et al. (2022). Membrane curvature governs the distribution of Piezo1 in live cells. Nat. Commun. *13*, 7467.

60. Yao, M., Tijore, A., Cheng, D., Li, J.V., Hariharan, A., Martinac, B., Tran Van Nhieu, G., Cox, C.D., and Sheetz, M. (2022). Force- and cell state–dependent recruitment of Piezo1 drives focal adhesion dynamics and calcium entry. Sci. Adv. *8*, eabo1461.

61. Denker, S.P., Huang, D.C., Orlowski, J., Furthmayr, H., and Barber, D.L. (2000). Direct binding of the Na-H exchanger NHE1 to ERM proteins regulates the cortical cytoskeleton and cell shape independently of H+ translocation. Mol. Cell. *6*, 1425–1436.

62. Denker, S.P., and Barber, D.L. (2002). Cell migration requires both ion translocation and cytoskeletal anchoring by the Na-H exchanger NHE1. J. Cell Biol. *159*, 1087–1096.

63. Wakabayashi, S., Ikeda, T., Iwamoto, T., Pouysségur, J., and Shigekawa, M. (1997). Calmodulin-binding autoinhibitory domain controls "pH-sensing" in the Na+/H+ exchanger NHE1 through sequence-specific interaction. Biochemistry *36*, 12854–12861.

64. Cho, S., Irianto, J., and Discher, D.E. (2017). Mechanosensing by the nucleus: From pathways to scaling relationships. J. Cell Biol. *216*, 305–315.

65. Mistriotis, P., Wisniewski, E.O., Bera, K., Keys, J., Li, Y., Tuntithavornwat, S., Law, R.A., Perez-Gonzalez, N.A., Erdogmus, E., Zhang, Y., et al. (2019). Confinement hinders motility by inducing RhoA-mediated nuclear influx, volume expansion, and blebbing. J. Cell Biol. *218*, 4093–4111.

66. Lomakin, A.J., Cattin, C.J., Cuvelier, D., Alraies, Z., Molina, M., Nader, G.P.F., Srivastava, N., Sáez, P.J., Garcia-Arcos, J.M., Zhitnyak, I.Y., et al. (2020). The nucleus acts as a ruler tailoring cell responses to spatial constraints. Science *370*, eaba2894.

67. Venturini, V., Pezzano, F., Castro, F.C., Häkkinen, H.M., Jiménez-Delgado, S., Colomer-Rosell, M., Marro, M., Tolosa-Ramon, Q., Paz-López, S., Valverde, M.A., et al. (2020). The nucleus measures shape changes for cellular proprioception to control dynamic cell behavior. Science *370*, 6514.

68. Kalukula, Y., Stephens, A.D., Lammerding, J., and Gabriele, S. (2022). Mechanics and functional consequences of nuclear deformations. Nat. Rev. Mol. Cell Biol. *23*, 583–602.

69. Song, Y., Soto, J., Chen, B., Hoffman, T., Zhao, W., Zhu, N., Peng, Q., Liu, L., Ly, C., Wong, P.K., et al. (2022). Transient nuclear deformation primes epigenetic state and promotes cell reprogramming. Nat. Mater. *21*, 1191–1199.

70. Pennacchio, F.A., Poli, A., Pramotton, F.M., Lavore, S., Rancati, I., Cinquanta, M., Vorselen, D., Prina, E., Romano, O.M., Ferrari, A., et al. (2024). N2FXm, a method for joint nuclear and cytoplasmic volume measurements, unravels the osmo-mechanical regulation of nuclear volume in mammalian cells. Nat. Commun. *15*, 1070.

71. Krämer, A., Green, J., Pollard, J., and Tugendreich, S. (2014). Causal analysis approaches in Ingenuity Pathway Analysis. Bioinformatics *30*, 523–530.

72. Rius, J., Guma, M., Schachtrup, C., Akassoglou, K., Zinkernagel, A.S., Nizet, V., Johnson, R.S., Haddad, G.G., and Karin, M. (2008). NF-kappaB links innate immunity to the hypoxic response through transcriptional regulation of HIF-1alpha. Nature *453*, 807–811.

73. Balamurugan, K., Wang, J.-M., Tsai, H.-H., Sharan, S., Anver, M., Leighty, R., and Sterneck, E. (2010). The tumour suppressor C/EBPδ inhibits FBXW7 expression and promotes mammary tumour metastasis. EMBO J. *29*, 4106–4117.

74. Zhang, C., Zhi, W.I., Lu, H., Samanta, D., Chen, I., Gabrielson, E., and Semenza, G.L. (2016). Hypoxia-inducible factors regulate pluripotency factor expression by ZNF217- and ALKBH5-mediated modulation of RNA methylation in breast cancer cells. Oncotarget *7*, 64527–64542.

75. Yang, D.-C., Yang, M.-H., Tsai, C.-C., Huang, T.-F., Chen, Y.-H., and Hung, S.-C. (2011). Hypoxia inhibits osteogenesis in human mesenchymal stem cells through direct regulation of RUNX2 by TWIST. PLoS One *6*, e23965.

76. Wagner, K.D., Wagner, N., Wellmann, S., Schley, G., Bondke, A., Theres, H., and Scholz, H. (2003). Oxygen-regulated expression of the Wilms' tumor suppressor Wt1 involves hypoxia-inducible factor-1 (HIF-1). Faseb. J. *17*, 1364–1366.

77. Lang, R., and Raffi, F.A.M. (2019). Dual-Specificity Phosphatases in Immunity and Infection: An Update. Int. J. Mol. Sci. *20*, 2710.

78. Mebratu, Y., and Tesfaigzi, Y. (2009). How ERK1/2 activation controls cell proliferation and cell death: Is subcellular localization the answer? Cell Cycle *8*, 1168–1175.

79. Chen, X., Lin, S., Lin, Y., Wu, S., Zhuo, M., Zhang, A., Zheng, J., and You, Z. (2022). BRAF-activated WT1 contributes to cancer growth and regulates autophagy and apoptosis in papillary thyroid carcinoma. J. Transl. Med. *20*, 79.

80. Chung, J., Uchida, E., Grammer, T.C., and Blenis, J. (1997). STAT3 serine phosphorylation by ERK-dependent and -independent pathways negatively modulates its tyrosine phosphorylation. Mol. Cell Biol. *17*, 6508–6516.

81. Gille, H., Kortenjann, M., Thomae, O., Moomaw, C., Slaughter, C., Cobb, M.H., and Shaw, P.E. (1995). ERK phosphorylation potentiates Elk-1-mediated ternary complex formation and transactivation. EMBO J. *14*, 951–962.

82. Yankaskas, C.L., Thompson, K.N., Paul, C.D., Vitolo, M.I., Mistriotis, P., Mahendra, A., Bajpai, V.K., Shea, D.J., Manto, K.M., Chai, A.C., et al. (2019). A microfluidic assay for the quantification of the metastatic propensity of breast cancer specimens. Nat. Biomed. Eng. *3*, 452–465.

83. Boyd-Shiwarski, C.R., Shiwarski, D.J., Griffiths, S.E., Beacham, R.T., Norrell, L., Morrison, D.E., Wang, J., Mann, J., Tennant, W., Anderson, E.N., et al. (2022). WNK kinases sense molecular crowding and rescue cell volume via phase separation. Cell *185*, 4488–4506.e20.

84. Guo, Y.-J., Pan, W.-W., Liu, S.-B., Shen, Z.-F., Xu, Y., and Hu, L.-L. (2020). ERK/MAPK signalling pathway and tumorigenesis. Exp. Ther. Med. *19*, 1997–2007.

85. Shorthouse, D., Riedel, A., Kerr, E., Pedro, L., Bihary, D., Samarajiwa, S., Martins, C.P., Shields, J., and Hall, B.A. (2018). Exploring the role of stromal osmoregulation in cancer and disease using executable modelling. Nat. Commun. *9*, 3011.

86. Yang, B., Wolfenson, H., Chung, V.Y., Nakazawa, N., Liu, S., Hu, J., Huang, R.Y.J., and Sheetz, M.P. (2020). Stopping transformed cancer cell growth by rigidity sensing. Nat. Mater. *19*, 239–250.

87. Tijore, A., Yao, M., Wang, Y.H., Hariharan, A., Nematbakhsh, Y., Lee Doss, B., Lim, C.T., and Sheetz, M. (2021). Selective killing of transformed cells by mechanical stretch. Biomaterials *275*, 120866.

88. Thaddeus, S.D. (1941). The transfer of potassium across the human blood cell membrance. J. Biol. Chem. *139*, 693–705.

89. Perez-Gonzalez, N.A., Rochman, N.D., Yao, K., Tao, J., Le, M.T.T., Flanary, S., Sablich, L., Toler, B., Crentsil, E., Takaesu, F., et al. (2019). YAP and TAZ regulate cell volume. J. Cell Biol. *218*, 3472–3488.

90. Pasantes-Morales, H., Olea, R.S., Miranda, D., and Morán, J. (1997). Volume regulation in NIH/3T3 cells not expressing P-glycoprotein. I. Regulatory volume decrease. Am. J. Physiol. *272*, C1798–C1803.

91. Model, M.A., Nia, F.H., Zook, E., Hollembeak, J.E., and Stauber, T. (2022). Uptake of Fluorescein upon Osmotic Cell Swelling is Dependent on the Volume- Regulated Anion Channel VRAC/LRRC8. Paracelsus Proc. Exp. Med. *1*, 3–14.

92. Pedersen, S.F., Darborg, B.V., Rentsch, M.L., and Rasmussen, M. (2007). Regulation of mitogen-activated protein kinase pathways by the plasma membrane Na+/H+ exchanger, NHE1. Arch. Biochem. Biophys. *462*, 195–201.

93. Haworth, R.S., McCann, C., Snabaitis, A.K., Roberts, N.A., and Avkiran, M. (2003). Stimulation of the plasma membrane Na+/H+ exchanger NHE1 by sustained intracellular acidosis. Evidence for a novel mechanism mediated by the ERK pathway. J. Biol. Chem. *278*, 31676–31684.

94. Mukhin, Y.V., Garnovskaya, M.N., Ullian, M.E., and Raymond, J.R. (2004). ERK is regulated by sodium-proton exchanger in rat aortic vascular smooth muscle cells. J. Biol. Chem. *279*, 1845–1852.

95. Mendoza, M.C., Er, E.E., and Blenis, J. (2011). The Ras-ERK and PI3K-mTOR pathways: Cross-talk and compensation. Trends Biochem. Sci. *36*, 320–328.

96. Webb, B.A., Chimenti, M., Jacobson, M.P., and Barber, D.L. (2011). Dysregulated pH: A perfect storm for cancer progression. Nat. Rev. Cancer *11*, 671–677.

97. Meima, M.E., Webb, B.A., Witkowska, H.E., and Barber, D.L. (2009). The sodium-hydrogen exchanger NHE1 is an akt substrate necessary for actin filament reorganization by growth factors. J. Biol. Chem. *284*, 26666–26675.

98. Yellin, F., Li, Y., Sreenivasan, V.K., Farrell, B., Johny, M.B., Yue, D., and Sun, S.X. (2018). Electromechanics and volume dynamics in non-excitable tissue cells. Biophys. J. *114*, 2231–2242.

99. Gadsby, D.C., Kimura, J., and Noma, A. (1985). Voltage dependence of Na/K pump current in isolated heart cells. Nature *315*, 63–65.

100. Casey, J.R., Grinstein, S., and Orlowski, J. (2010). Sensors and regulators of intracellular pH. Nat. Rev. Mol. Cell Biol. *11*, 50–61.

101. Weinstein, A.M. (1986). A mathematical model of the rat proximal tubule. Am. J. Physiol. Ren. Physiol. *250*, F860–F873.

102. Palchesko, R.N., Zhang, L., Sun, Y., and Feinberg, A.W. (2012). Development of Polydimethylsiloxane Substrates with Tunable Elastic Modulus to Study Cell Mechanobiology in Muscle and Nerve. PLoS One *7*, e51499.

103. Stewart, S.A., Dykxhoorn, D.M., Palliser, D., Mizuno, H., Yu, E.Y., An, D.S., Sabatini, D.M., Chen, I.S.Y., Hahn, W.C., Sharp, P.A., et al. (2003). Lentivirus-delivered stable gene silencing by RNAi in primary cells. RNA *9*, 493–501.

104. Belin, B.J., Goins, L.M., and Mullins, R.D. (2014). Comparative analysis of tools for live cell imaging of actin network architecture. BioArchitecture *4*, 189–202.

105. Liberti, W.A., Markowitz, J.E., Perkins, L.N., Liberti, D.C., Leman, D.P., Guitchounts, G., Velho, T., Kotton, D.N., Lois, C., and Gardner, T.J. (2016). Unstable neurons underlie a stable learned behavior. Nat. Neurosci. *19*, 1665–1671.

106. MODEL, M. (2020). Comparison of cell volume measurements by fluorescence and absorption exclusion microscopy. J. Microsc. *280*, 12–18.

107. Pusl, T., Wu, J.J., Zimmerman, T.L., Zhang, L., Ehrlich, B.E., Berchtold, M.W., Hoek, J.B., Karpen, S.J., Nathanson, M.H., and Bennett, A.M. (2002). Epidermal growth factor-mediated activation of the ETS domain transcription factor Elk-1 requires nuclear calcium. J. Biol. Chem. *277*, 27517–27527.

108. Li, Y., Konstantopoulos, K., Zhao, R., Mori, Y., and Sun, S.X. (2020). The importance of water and hydraulic pressure in cell dynamics. J. Cell Sci. *133*, jcs240341.

STAR★METHODS

KEY RESOURCES TABLE

REAGENT or RESOURCE	SOURCE	IDENTIFIER
Antibodies		
Anti-pMLC (Ser19)	Cell Signaling	Cat# 3671
anti-NHE1	Invitrogen	Cat# PA5-116471
anti-NHE1	Santa Cruz Biotechnology	Cat# sc-136239
anti-Piezo1	Invitrogen	Cat# PA5-77617
anti-Ki-67	Cell Signaling	Cat# 9129
anti-Phospho-p44/42 MAPK	Cell Signaling	Cat# 9101
anti-p44/42 MAPK	Cell Signaling	Cat# 4695
Anti-GAPDH	Cell Signaling	Cat# 2118
Alexa Fluor 488 goat anti-rabbit immunoglobulin G (IgG) H + L	Invitrogen	Cat# A11008
anti-mouse IgG, HRP-linked antibody	Cell Signaling	Cat# 7076
anti-rabbit IgG HRP-linked antibody	Cell Signaling	Cat# 7074S
Chemicals, peptides, and recombinant proteins		
DMSO	Invitrogen	Cat# D12345
Latrunculin A	Tocris	Cat# 3973
Cytochalasin D	Tocris	Cat# 12331
S)-nitro-Blebbistatin	Cayman Chemical	Cat# 13891
PF-562271	Selleckchem	Cat# S2890
W7 hydrochloride	Tocris	Cat# 0369
NSC668394	Sigma Aldrich	Cat# 341216
Ouabain	Tocris	Cat# 1076
EIPA	Tocris	Cat# 3378
Bumetanide	Tocris	Cat# 3108
DCPIB	MedChemExpress	Cat# HY-103371
4-Aminopyridine	Tocris	Cat# 0940
Ruthenium red	Tocris	Cat# 1439
Gadolinium chloride	Tocris	Cat# 4741
BAPTA Tetrapotassium Salt	Invitrogen	Cat# B1204
BAPTA-AM	Invitrogen	Cat# B1205
Trametinib	MedChemExpress	Cat# HY-10999
Fluorescein isothiocyanate–dextran	Sigma Aldrich	Cat# FD2000S
Type I rat-tail collagen	Enzo	Cat# ALX-522-435
Alexa Fluor 647 Phalloidin	Invitrogen	Cat# A22287
Hoechst 33342	Invitrogen	Cat# H3570
Flipper-TR	Spirochrome	Cat# CY-SC020
SPY650-FastAct	Spirochrome	Cat# CY-SC505
Sylgard 184	Dow	Cat# 4019862
Sylgard 527	Dow	Cat# 1696742
CY52-276	Dow	Cat# 2624028
Polybrene Transfection Reagent	Sigma Aldrich	Cat# TR-1003
Puromycin	Sigma Aldrich	Cat# P8833
pHrodo Red AM	Invitrogen	Cat# P35372
intracellular pH calibration buffer Kit	Invitrogen	Cat# P35379
PLL-g-PEG	NanoSoft	Cat# 11354

(*Continued on next page*)

Continued

REAGENT or RESOURCE	SOURCE	IDENTIFIER
Deposited data		
RNA-seq data	This paper	NCBI: PRJNA1175048
Experimental models: Cell lines		
NIH-3T3	Lab of Denis Wirtz	RRID: CVCL_0594
HT1080	Lab of Denis Wirtz	RRID: CVCL_0317
WI-38	Lab of Denis Wirtz	RRID: CVCL_0579
HEK 293A	Lab of Kun-Liang Guan	RRID: CVCL_6910
hTERT-RPE1	Lab of Rong Li	RRID: CVCL_4388
MCF-10A	ATCC	ATCC: CRL-10317
MDA-MB-231	ATCC	ATCC: HTB-26
HFF-1	ATCC	ATCC: SCRC-1041
Hs578t	ATCC	ATCC: HTB-126
BT-549	ATCC	ATCC: HTB-122
KPC cell lines	Lab of Denis Wirtz	N/A
Oligonucleotides		
shNHE1 targeting sequence 5′-GACAAGCTCAACCGGTTTAAT-3′	This paper	N/A
shRNA scramble control sequence 5′-GCACTACCAGAGCTAACTCAGATAGTACT-3′	This paper	N/A
Piezo1 knockout targeting sequence 5′-AGCATTGAAGCGTAACAGGG-PAM-3	Invitrogen	Cat# A35533
Primer Piezo1 forward: TATCATGGGAC CTGGGCATC, reverse: CAGGTGTGCACTGAAGGAAC	This paper	N/A
Recombinant DNA		
pLKO.1 puro	Stewart et al.[102]	Addgene: 8453
pEGFP-C1 F-tractin-EGFP	Belin et al.[103]	Addgene: 58473
pHAGE-RSV-GCaMP6s	Liberti et al.[104]	Addgene: 80146
pCMV-PV-NES-GFP	Pusl et al.[105]	Addgene: 17301
Software and algorithms		
MATLAB	MathWorks	N/A
Fiji (ImageJ)	https://imagej.net/Fiji	N/A
R	https://www.r-project.org/	N/A
Prism	GraphPad	N/A
SymPhoTime 64	PicoQuant	N/A
Ingenuity Pathway Analysis	Qiagen	N/A

EXPERIMENTAL MODEL AND STUDY PARTICIPANT DETAILS

Cell culture

NIH 3T3, HT1080, and WI-38 cells were a gift from Denis Wirtz (Johns Hopkins University, Baltimore, MD). HEK 293A cells were a gift from Kun-Liang Guan (University of California, San Diego, San Diego, CA). RPE-1 cells were a gift from Rong Li (Johns Hopkins University, Baltimore, MD). MCF-10A, MDA-MB-231, HFF-1 cells were purchased from American Type Culture Collection. 3T3, HT1080, MDA-MB-231, RPE-1, HEK 293A, and HFF-1 were cultured in Dulbecco's modified Eagle's media (DMEM; Corning) supplemented with 10% fetal bovine serum (FBS; Sigma), and 1% antibiotics solution contains 10,000 units/mL penicillin and 10,000 μg/mL streptomycin (Gibco). WI-38 cells were cultured in DMEM (low glucose 1 g/L; Gibco), with 15% FBS and 1% PS. MCF-10A were cultured in DMEM/F-12 supplemented with 5% horse serum, 20 ng/mL epidermal growth factor, 0.5 μg/mL hydrocortisone, 100 ng/mL cholera toxin, 10 μg/mL insulin, and 1% antibiotics solution, as previously described.[82] Cells were passaged using 0.05% trypsin-EDTA (Gibco). All cell cultures and live cell experiments were conducted at 37°C and 5% CO2.

METHOD DETAILS

Osmotic shock media preparation, and pharmacological inhibitors

Before hypotonic shock experiment, cells were pre-incubated in isotonic solution overnight. The isotonic solution (312 mOsm) contains 50% Dulbecco's phosphate-buffered saline without calcium and magnesium (Sigma-Aldrich) and 50% cell culture media. 50% hypotonic media (175 mOsm) was prepared by mixing 50% ultra-pure water with 50% cell culture media. For hypertonic shock experiment, cells were cultured in regular cell culture media, and then switched to hypertonic media (504 mOsm). The hypertonic media is the cell culture media supplemented with 160 mM D-Sorbitol (MilliporeSigma). The osmolality was measured using Advanced Instruments model 3320 osmometer.

In select experiments, cells were treated with the following pharmacological agents (purchased from Tocris unless otherwise stated): vehicle controls using DMSO (0.25%, Invitrogen), Latrunculin A (100 nM), Cytochalasin D (500 nM), (S)-nitro-Blebbistatin (1 μM, Cayman Chemical), PF-562271 (10 μM, Selleckchem), W7 hydrochloride (20 μM), NSC668394 (10 μM, MilliporeSigma), Ouabain (250 μM), EIPA (100 μM for 3T3, 50 μM for other cell lines), Bumetanide (40 μM), DCPIB (20 μM, Medchemexpress), 4-Aminopyridine (4-AP, 1 mM), Ruthenium red (20 μM), Gadolinium chloride (GdCl3, 20 μM), BAPTA Tetrapotassium Salt (1mM, Invitrogen), BAPTA-AM (5 μM, Invitrogen), and Trametinib (0.2 μM, Medchemexpress). In osmotic shock experiment, cells were pre-adapted in pharmacological agents for 2h expect for Latrunculin A (1 h), Cytochalasin D (1 h), EIPA (1 h), and Ouabain (4 h).

Microfluidic device fabrication

A detailed protocol can be found in Rochman et al.[40] In brief, FXm channel masks were designed using AutoCAD and ordered from FineLineImaging. Silicon molds were fabricated using SU8-3010 (Kayaku) photoresist following standard photolithography procedures and manufacturer's protocol. Two layers of photoresist were spin coated on a silicon wafer (IWS) at 500 rpm for 7 s with acceleration of 100 rpm/s, and at 2,000 rpm for 30 s with acceleration of 300 rpm/s, respectively. After a soft bake of 4 min at 95°C, UV light was used to etch the desired patterns from negative photoresist to yield feature heights that were $\sim$ 12 μm. The length of the channels is 16 mm and the width is 1.2 mm.

A 10:1 ratio of PDMS Sylgard 184 silicone elastomer and curing agent were vigorously stirred, vacuum degassed, poured onto each silicon wafer, and cured in an oven at 80°C for 45 min. Razor blades were then used to cut the devices into the proper dimensions, and inlet and outlet ports were punched using a blunt-tipped 21-gauge needle (McMaster Carr; 76165A679). The devices were cleaned by sonicating in 100% isopropyl alcohol for 10 min, and dried using a compressed air gun. The devices and sterilized 50-mm glass-bottom Petri dishes (FlouroDish Cell Culture Dish; World Precision Instruments) were exposed to oxygen plasma for 1 min for bonding. The bonded devices were then placed in an oven at 80°C for 45 min to further ensure bonding.

Cell volume tracking during pharmacological inhibition and osmotic shock experiment

Micro-fluidic FXm chambers were incubated with 50 μg/mL of type I rat-tail collagen (Enzo) for 1 h at 37°C, followed by washing with isotonic media. Before experiment, $\sim$ 1–2 million per mL cells with 0.2 mg/mL Alexa Fluor 488 Dextran (MW 2,000 kDa; ThermoFisher) dissolved in isotonic media were injected into the devices using syringe. Cells were then incubated for 1-2 h to allow them to attach and spread. To apply drug or osmotic shock, hypotonic or hypertonic media were injected into the channel gently using a syringe with the same amount of dextran. For osmotic shock experiment with drug treatment, cells were pre-adapted 1–4 h in the FXm device before applying osmotic shock. Cells were imaged using fluorescence microscopes as detailed below. The microscope was also equipped with a CO2 module and TempModule stage top incubator (Pecon) that was set to 37°C and 5% CO2 during the experiment. Biological repeat with sample size N $\geq$ 3 for all experiments.

Data analysis and cell volume calculation in fluorescence exclusion method

Individual cells were tracked by customized MATLAB code using the following algorithm. Firstly, a rough cell mask was draw from a Gaussian blurred epifluorescence image by a set threshold intensity for each cell. The cell mask was then expanded by 10 pixels (2.27 μm) in each direction to ensure proper cell cropping, and a rectangular box was draw based on the largest lateral dimensions in x and y direction. A cell would be discarded if any overlapping cells were found in the box. After all images at different time points were processed, we ran an automatic cell tracking algorithm based on the position of geometric center of each cell mask. In brief, the algorithm assigned each cell (C_t) to the closest cell in the next time frame ($C_{t+\Delta t}$), and then cross validated the tracking by assigning $C_{t+\Delta t}$ to its closest cell at frame t. The cell would be discarded if the cross validation failed to find C_t as the closest neighbor or found more than one closest neighbor, which is normally due to cell migration, detachment, or overlapping with other cells. The results from automatic cell tracking algorithm were then examined manually by one of the authors.

Cropped images from single cell tracking were then used for cell volume calculation based on the Fluorescence Exclusion method (FXm). The mean fluorescence intensity of the pixels outside cell masks, defined as the mean background intensity I_{bg}, reflects the height of the FXm channel. The local intensity within the cell mask, I_V defined the difference between channel height and cell height. Given a known channel height h, measured by confocal microscopy, the cell volume V can be calculated using the equation

$$V = h \iint_A \left(1 - \frac{I_V}{I_{bg}}\right) dA.$$

Benchmarking cell volume measurement using FXm

In this section, we discuss factors that affect the accuracy of FXm and how we benchmarked them. For the method details, please refer to previous STAR Methods section and to Cadart et al. (2017) and Rochman et al. (2020).[39,40]

We first examined whether endocytosis of dextran affects the volume measurement. High uptake of dextran can reduces the dye exclusion and leads to lower measured volume. We first incubated cells with Alexa Fluor 488 (2,000 kDa) dextran for 5 h. This time is longer than the typical dextran exposure time in our experiment. We then washed the dextran out and examined the remain fluorescence uptaken by cells. A representative image is shown in Figure S12A, where no significant fluorescence can be observed. We thus conclude that endocytosis does not affect cell volume measurement in this work.

We then examined whether our epi-fluorescence microscope was able to detect the fluorescence signals from the entire chamber. The chamber height is 12 μm. We thus imaged at different focus z positions by +/− 10 μm. The intensity from a space with no cells varies by +/− 2% (Figure S12B), indicating the microscope has the ability to detect all signals from the FXm device. We also examined the measured cell volume at different Z planes and observed up to 2% of volume measurement error (Figure S12C). This error is in agreement with the reported value by others,[39,106] and is relative small comparing to the observed volume change in this work.

Lastly, we examined whether FXm chamber physically confines cells during experiment. In all experiments, cells were allowed to fully spread, and the average cell height (averaged over the entire surface) is 2.5 μm and the maximum height is 6 μm for most cell types (Figures S12D and S12E). By tracking the cell height during osmotic shock, we found that some cell types, such as 3T3 can reach 3.5 μm on average cell height and 8 μm on maximum cell height. This cell height is far below the 12 μm channel height and thus FXm chamber is not a confinement. The only exception we observed is HT1080 cells treated with ouabain and subjected to hypotonic shock.

Nucleus volume measurement using N2FXm

To measure nucleus volume, we utilized the N2FXm technique as based on Pennacchio et al.[70] Cells stably expressing GFP-NES were generated as described below. These cells were seeded into the FXm channel containing 0.2 mg/mL Texas Red dextran (MW 70 kDa; Invitrogen) before experiment. Both Texas Red and NES-GFP were simultaneously imaged. Other experimental procedures follow the same protocol as FXm.

To determine nucleus volume, we first computed a cell height map (h_{cell}) using the the FXm protocol described above. Background subtraction was performed on the GFP-NES channel, which stains the entire cytoplasm except for the nucleus. This allows the intensity I_{NES} to be used to estimate the relative height of the cytoplasm compared to the cell. Regions of the cytoplasm not influenced by the nucleus were masked based on GFP-NES intensity (I_{cyto}). A relative height factor was then calculated as $\langle h_{cyto}/I_{cyto}\rangle$, where h_{cyto} is the cell height from the same part analyzed in the FXm. Subsequently, the cytoplasm volume V_{cyto} was calculated as $V_{cyto} = \iint_A (h_{cell} \times \langle h_{cyto}/I_{cyto}\rangle)\, dA$. The nucleus volume is then derived as $V_{cell} - V_{cyto}$.

Epi-fluorescence and confocal microscopy

For epi-fluorescence imaging, a Zeiss Axio Observer inverted, wide-field microscope using a 20× air, 0.8-NA objective or a 63× oil-immersion, 1.2-NA objective equipped with an Axiocam 560 mono charged-coupled device camera was used. In some experiments, a similar microscope equipped with a Hamamatsu Flash4.0 V3 sCMOS camera was used. For confocal imaging, a Zeiss LSM 800 confocal microscope equipped with a 63× oil-immersion, 1.2-NA objective was used. All microscopes were equipped with a CO2 Module S (Zeiss) and TempModule S (Zeiss) stage-top incubator (Pecon) that was set to 37°C with 5% CO2 for live cell imaging. For imaging of immunofluorescence assays, the samples were imaged under room temperature and without CO2. ZEN 2.6 or 3.6 Software (Zeiss) was used as the acquisition software. Customized MATLAB (MathWorks) programs or ImageJ were used for image analysis subsequent to data acquisition.

Measurement of membrane tension using fluorescence lifetime imaging microscopy and Flipper-TR

Cells were seeded into collagen-I coated (50 μg/mL for 1 h at 37°C) glass bottom 24 well plates or 35 mm glass bottom dish coated with 15 kPa PDMS substrates at a density of 5000 cells/cm^2 in isotonic media overnight. Cells were stained with 1 μM Flipper-TR (Spirochrome) for 30 min and imaged thereafter. Hypotonic shock was then conducted, and cells were imaged 3 min, 30 min, and 2 h after shock. Confocal fluorescence lifetime imaging microscopy was performed using a Zeiss LSM 780 microscope and a PicoQuant system consisting of a PicoHarp 300 time-correlated single-photon counting (TCSPC) module, two-hybrid PMA-04 detectors, and a Sepia II laser control module. A 485 nm laser line was used for excitation with a 600/50 nm band-pass detector unit. Cells were maintained at 37°C with 5% CO2 in a Pecon incubator during imaging. The data analysis was performed as previously described[47] using SymPhoTime 64 (PicoQuant) software.

PDMS substrates fabrication

3 kPa PDMS substrates were prepared by mixing a 1:1 weight ratio of CY52-276A and CY52-276B (Dow).[24] To generate 15 kPa and 130 kPa substrates, 2% and 20% Sylgard 527 (Dow, 1:1 base to curing agent ratio) were added to Sylgard 184 (Dow, 10:1 base to curing agent ratio), respectively.[102] In all cases, the elastomer was vacuum-degassed for approximately 5 min to eliminate bubbles,

and then spin-coated onto 35 mm or 50 mm glass bottom dishes at 1,000 rpm for 60 s. The dishes were cured overnight at room temperature, and then at 80°C for 20 min. The devices were subsequently plasma-treated and bonded to the FXm devices for cell volume measurement.

Live cell reporters, cloning, lentivirus preparation, transduction, and transfection

To generate 3T3 cells with stable knockdown of NHE1, the pLKO.1 puro (Addgene; 8453; a gift from Bob Weinberg)[103] backbone was used. For NHE1 depletion, the sequence 5′-GACAAGCTCAACCGGTTTAAT-3′ was subcloned into the pLKO.1 backbone. For generating control cell lines, the non-targeting scramble control sequence 5′-GCACTACCAGAGCTAACTCAGATAGTACT-3′ was subcloned into the pLKO.1 puro backbone.

For lentivirus production, HEK 293T/17 cells were co-transfected with psPAX2, VSVG, and the lentiviral plasmid of interest. 48 h after transfection, the lentivirus was harvested and concentrated using centrifugation. Wild-type 3T3 cells at 60–80% confluency were incubated for 24 h with 100X virus suspension and 8 μg/mL of Polybrene Transfection Reagent (Millipore Sigma). To maintain stable knockdown, cells transduced with the pLKO.1 puro backbone or sgBag6_1 with Ef1alpha Puro-P2A-BFP(1)(1) backbone were cultured in medium containing 0.5 μg/mL Puromycin (Gibco).

To label F-actin, we use both chemical probe SPY650-FastAct (SpiroChrome) and genetically coded indicator F-tractin. For SPY650-FastAct, we stained (1:1000) cells for 30 min prior to experiment following manufacturer's protocol. EGFP-C1 F-tractin-EGFP (Addgene 58473, a gift from Dyche Mullins)[104] plasmid was used for transient transfections. About 60–80% confluent 3T3 or HT1080 cells were transfected using Lipofectamine 3000 reagent following the manufacturer's recommendations. pHAGE-RSV-GCaMP6s (Addgene 80146, a gift from Darrell Kotton)[105] plasmid was used for Ca^{2+} imaging via lentiviral cell transduction. The lentivirus production is described above, and cells were selected using flow cytometry.

pCMV-PV-NES-GFP (Addgene 17301, gift from Anton Bennett)[107] plasmid was used to generate stable cell lines for N2FXm. To generate stable cell lines with NES-GFP, PiggyBac vector was generated by cloning PCR-amplified construct to PiggyBacc vector backbone via HiFi assembly (NEB). Wild-type 3T3 cells were transfected by 9:1 of PiggyBacc plasmids and Super-PiggyBacc transposase using Lipofectamine 3000 reagent following the manufacturer's guidance. To establish a stable-integrated transgenic cell line, the cell culture media is replenished with a complete medium supplied with 0.5 μg/mL of puromycin (Gibco) since day 1 post-transfection. Puromycin was refreshed every 2–3 days until the cell reached confluency and cryo-preserved. Expression of NES-GFP was induced by doxycycline (1 μg/mL) for 16 h before experiment.

CRISPR knockout

Single guide RNA (sgRNA) against PIEZO1 that targets the 5′-AGCATTGAAGCGTAACAGGG-PAM-3′ at Chr.8: 122513787–122513809 on GRCm38 was purchased from Invitrogen (A35533). The cells were transfected with the Cas9 enzyme (TrueCut Cas9 Protein v2, Thermo Fisher) and the sgRNA using Lipofectamine CRISPRMAX Transfection Reagent (Thermo Fisher) according to the manufacturer's instructions. Transfected cells were then expanded as single-cell clones by limited dilution into 96 well plates. To evaluate the editing efficiency, GeneArt Genomic Cleavage Detection Kit (Life Technologies) was used according to the manufacturer's instructions. Then, the following primers were used to amplify the region covering the CRISPR binding site: TATCATGGGACC TGGGCATC (forward), CAGGTGTGCACTGAAGGAAC (reverse). The knockout of Piezo1 was confirmed by next generation sequencing (NGS, provided by Genewiz) and western blot (Figure S5).

Immunofluorescence and image analysis

Cells were seeded into collagen-I coated (50 μg/mL for 1 h in 37°C) glass bottom 24 well plates or 35 mm glass bottom dish coated with 15kPa PDMS substrates at a density of 5000 cells/cm^2 overnight. For pMLC staining, hypotonic shock was applied and cells were fixed with 4% paraformaldehyde (ThermoFisher Scientific) at different time points as indicated. After washing 3X with PBS, cells were permeabilized in 0.1% Triton X-100 for 15 min. Then, cells were washed 3X in PBS and blocked for 1 h at RT with 5% BSA solution containing 5% normal goat serum (Cell Signaling) and 0.1% Triton X-100. Next, cells were incubated at 4°C with primary antibody overnight. After washing 3X with PBS, samples were incubated for 1 h at RT with secondary antibody. NHE1 staining follows the same protocol as described above but without osmotic shock. Primary antibody: anti-pMLC (Ser19) antibody (Cell Signaling; 3671; 1:100), anti-NHE1 (Invitrogen; PA5-116471; 1:100), anti-Piezo1 (Invitrogen; PA5-77617; 1:500), and anti-Ki-67 (Cell Signaling; 9129; 1:400). Secondary antibody: Alexa Fluor 488 goat anti-rabbit immunoglobulin G (IgG) H + L, (Invitrogen; A11008; 1:200). For actin staining, Alexa Fluor 647 Phalloidin (Invitrogen; A22287; 1:100) were added for 1h at RT. For nucleus staining, Hoechst 33342 (Invitrogen; H3570; 1:10000) were added for 10 min at RT.

Wide-field microscopy using the setup as described above was used to measure the total pMLC and Ki-67contents. A rectangle was cropped for each cell, and the boundary of the cropped area was used for calculating background intensity. The total expressed protein contents of each cell were quantified by summing all intensity after background subtraction. To evaluate Ki-67 expression, cell nucleus masks were drawn based on the Hoechst channel after cropping and background subtraction as aforementioned. The nucleus mask was then applied to Ki-67 staining images to measure the total intensity within each cell nucleus. The spatial distribution of NHE1 and actin was obtained using a confocal microscope as described above. A line was drawn along the cell to obtain the spatial distribution of NHE1 and actin using ImageJ.

Western blot

Western blots were performed using protocols previously described in Mistriotis et al.,[65] using NuPAGE 4–12% Bis-Tris Protein Gels (Thermo Fischer Scientific, NP0336BOX) in Invitrogen Novex NuPage MES SDS Running Buffer (1X, Thermo Fisher Scientific, NP0002). Primary antibody: anti-NHE1 (Santa Cruz Biotechnology; sc-136239; 1:1000), anti-Piezo1 (Invitrogen; PA5-77617; 1:1000), anti-Phospho-p44/42 MAPK (*p*-ERK1/2; Cell Signaling; 9101; 1:1000), anti-p44/42 MAPK (ERK1/2; Cell Signaling; 4695; 1:1000). GAPDH was used as a loading control (Cell Signaling; 2118; 1:4000). Secondary Antibody: anti-mouse IgG, HRP-linked antibody (Cell Signaling; 7076; 1:1000), and anti-rabbit IgG HRP-linked antibody (Cell Signaling, 7074S; 1:1000). Uncropped western blot imagings can be found in Figure S16.

Intracellular pH measurement

Intracellular pH was measured using pHrodo Red AM, following the manufacturer's instructions. Cells were seeded into collagen-I coated (50 μg/mL for 1 h at 37°C) glass bottom 24 well plates or 35 mm glass bottom dish coated with a 15kPa PDMS substrates at a density of 5000 cells/cm^2 overnight in isotonic media. Cells were then incubated with 1mL of media containing a dilution of 1 μL of 5 mM pHrodo Red AM in 10 μL of PowerLoad 100X concentrate at 37°C for 30 min. The cells were gently washed once with media and allowed to settle for 15 min before imaging. Cells before and after hypotonic shock were imaged every 5 min using a wide-field epi-fluorescence microscope as previously described. A rectangle larger than the cell size was cropped for each cell, and the signal at the boundary of each cropped area was used to calculate background intensity. pHrodo Red AM signals of individual cells were tracked and measured within the cropped area after background subtraction.

To obtain the absolute pH of different cell types, an intracellular pH calibration buffer Kit (Invitrogen, P35379) was used with pHrodo Red AM, following the manufacturer's protocol. Briefly, after loading pHrodo Red AM as instructed above, cells were then loaded with the calibration buffer containing 10 μM valinomycin and 10 μM of nigericin at pH values of 4.5, 5.5, 6.7, and 7.5 for at least 5 min. The cells were then imaged and processed through the same background subtraction as described above. Cells were masked, and the mean intensity per pixel was calculated for each cell. A pH calibration curve was then generated by linearly fitting the results from the calibration experiment. Single cell pHrodo intensity was measured, processed, and fitted into the calibration curve to obtain single cell pH results. Relative intracellular pH change ΔpH_i is calculated by comparing pH_i to isotonic or un-stretched points of each single cell.

Mechanical stretching

Cells were seeded into elastic PDMS chambers (STB-CH-4W, STREX) at a density of 5000 cells/cm^2 with cell culture media. The PDMS chambers were pre-coated with 200 μg/mL collagen-I (Enzo) for 4 h at 37°C. A one-time, 20% uniaxial stretching was applied using a mechanical stretching device (STB-100, STREX). pH measurement and data analysis were conducted as described above. Mechanical stretching may cause cell detachment; therefore, only cells that remained attached and spread both before and after mechanical stretching were analyzed.

Calcium dynamics imaging and quantification

Cells transiently expressing pGP-CMV-GCaMP6s were seeded into collagen I coated, glass bottom 24 well plate overnight at a density of 5000 cells/cm^2. For low frequency Ca^{2+} dynamics, cells before and after hypotonic shock were imaged every 2 min using the confocal microscope as described above. Ca^{2+} dynamics were monitored by the mean cell GFP signals per pixel using the image processing method as described above. To measure Ca^{2+} spikes, cells in isotonic media or subjected to hypotonic shock for 20 min were imaged every 10 s using the confocal microscope. Ca^{2+} spikes were identified as instances with greater than 2 times intensity over baseline signals.

RNA-seq and analysis

Total RNA was extracted and purified using RNeasy Mini Kit (Qiagen) or Quick-DNA/RNA MiniPrep Plus Kit (Zymo Research #D7003) following the manufacturer's protocol. Strand specific mRNA libraries were generated using the NEBNext Ultra II Directional RNA library prep Kit for Illumina (New England BioLabs #E7760), mRNA was isolated using Poly(A) mRNA magnetic isolation module (New England BioLabs #E7490). Preparation of libraries followed the manufacturer's protocol (Version 2.2 05/19). Input was 1ug and samples were fragmented for 15 min for RNA insert size of 200 bp. The following PCR cycling conditions were used: 98°C 30s/8 cycles: 98°C 10s, 65°C 75s/65°C 5 min. Stranded mRNA libraries were sequenced on an Illumina NovaSeq instrument, SP flowcell using 100bp paired-end dual indexed reads and 1% PhiX control.

Reads were trimmed by 8 base pairs on either end with the Cutadapt package and mapped to the mouse GRCm38 (mm10) or human GRCh38 (hg38) using the Salmon package. Reference genomes were obtained from Ensemble. Batch correction was performed in R with ComBat seq. In R (v.4.2.3), the DESeq2 package was used to determine differentially expressed genes between samples of interest with *p* values for each gene and comparison. *p* values were calculated with the DESeq2 package, assuming a negative binomial distribution and correcting for FDR. Differentially expressed genes with an FDR corrected *p* value $\langle = < 0.05$ were presented in volcano plots and further analyzed. The significantly differentially expressed genes with a log2 fold change $<= -1$ or $> = 1$ were input into Ingenuity Pathway Analysis (Qiagen) to determine pathway enrichment (significance determined by Fischer's exact method).

DNA extraction and whole-genome bisulfite sequencing (WGBS)

DNA was extracted using the Quick-DNA/RNA MiniPrep Plus Kit (Zymo Research #D7003) according to the manufacturer's instructions and genomic DNA samples were quantified by Qubit dsDNA HS assay (ThermoFisher #Q32851). WGBS libraries were prepared using the NEBNext Ultra DNA Library Prep Kit (NEB #E7370L) according to manufacturer's instructions with modifications. 1% unmethylated Lambda DNA (Promega #D1521) was spiked into genomic DNA to monitor bisulfite conversion efficiency. Genomic DNA (500ng) was fragmented to a target peak of 300–400 bp using a Covaris S2 Focused-ultrasonicator according to the manufacturer's instructions. Genomic DNA (500 ng) was fragmented to a target peak of 300–400 bp using a Covaris S2 Focused-ultrasonicator according to the manufacturer's instructions. The fragmented DNA was converted to end-repaired, adenylated DNA using NEBNext Ultra End Repair/dA-Tailing Module (NEB #7442L). Methylated adaptors (NEBNext Multiplex Oligos for Illumina; NEB #E7535L) were ligated to the product from the preceding step using NEBNext Ultra Ligation Module (NEB #7445L). The resulting product was size-selected as described in the manufacturer's protocol by employing modified SPRIselect (Beckman Coulter #B23318) bead ratios of 0.37X and 0.2X to select for an insert size of 300–400 bp. After size selection, the samples were bisulfite converted and purified using the EZ DNA Methylation-Lightning Kit (Zymo #D5030). Bisulfite-converted libraries were PCR-amplified and uniquely dual-indexed using NEBNext Multiplex Oligos for Illumina (NEB #E6440S) and the Kapa HiFi Uracil+ PCR system (Kapa #KK2801). PCR enrichment was performed with the following cycling parameters: 98°C for 45 s followed by 8 cycles at 98°C for 15 s, 65°C for 30 s, 72°C for 30 s and a final extension at 72°C for 1 min. The PCR-enriched product was purified via two successive 0.9X SPRIselect bead cleanups. The resulting WGBS libraries were evaluated on a 2100 Bioanalyzer using Agilent High-Sensitivity DNA Kit (Agilent #5067-4626) and quantified via qPCR using the KAPA Library Quantification Kit (KAPA #KK4824). WGBS libraries were sequenced on an Illumina NovaSeq6000 system at a 2 × 150 bp read length with a 5% PhiX control library spike-in.

Analysis of WGBS data

Adapter sequences were computationally trimmed with Trim Galore, using default parameters for libraries prepared with NEBNext. Bisulfite-aware alignment of the trimmed reads to the mm10 genome was performed using Bismark with default parameters. Samtools was used to merge individual bam files corresponding to fastq file pairs and to name-sort the merged bam file. Methylation bias (mbias) plots were generated using Bismark's methylation extractor in –mbias_only mode. Regions of methylation bias at the 5′ and 3′ ends of reads were determined visually. Bismark was then used to deduplicate merged, name-sorted bam files, and finally, Bismark's methylation_extractor was used to create CpG_report files. Successful bisulfite conversion rate was confirmed by alignment of trimmed reads to the lambda genome using Bismark with default parameters.

The Bioconductor package DMRseq was used for DMR-finding. The cytosine report output files from Bismark's methylation_extractor were used as inputs to DMRseq. CpG methylation values were coverage-filtered with a cutoff of 2X for each replicate. Then DMRseq was run to find DMRs; aside from allowing a minimum of 3 CpGs per DMR and using 24 chromosomes per chunk, default parameters were used. Genes overlapping DMRs were identified using Bioconductor package GenomicRanges. DMRs were then filtered to those that overlapped a gene with significant differential expression of RNA. Gene set enrichment analysis was performed using web program Enrichr.

Model overview

The model of cell volume considers the coupled interactions between different ion transporters and the cell mechanics. The model details can be found in Li et al.[42] Briefly, we consider the following intracellular species: $Na^+, K^+, Cl^-, H^+, HCO_3^-, A^-, Buf^-$, and HBuf. A^- is the charged organic molecules and proteins that are not permeable across the cell membrane. Buf^- and HBuf are unprotonated buffer and protonated buffer species, respectively, where the total buffer $Buf^- + HBuf$ concentration is fixed and both species are non-permeable across the cell membrane. The cell is assumed to be spherical, and the change of cell radius is controlled by water flux across the cell surface (J_{water}) as

$$\frac{dr}{dt} = J_{water} = -\alpha_W(\Delta p - \Delta \Pi). \quad \text{(Equation 1)}$$

In this equation, the water flux is determined by the difference between the hydrostatic pressure (Δp) and the osmotic pressure gradient ($\Delta \Pi$) across the cell surface.[13,108] α_W is the combined permeability coefficient of water of cell lipid membrane and aquaporins. The force generated by hydrostatic pressure on cell surface is under force balance with cell membrane and the actomyosin cortical tension, which can be written by Laplace Law as $\Delta p = 2h\sigma/r$. The osmotic pressure gradient is written as

$$\Delta \Pi = RT\left(\sum_n c_n - \sum_n c_n^0\right), \quad \text{(Equation 2)}$$

where $c_n = \{c_{Na}, c_K, c_{Cl}, c_H, c_{HCO_3}, c_A, c_{Buf}, c_{HBuf}\}^T$ is the intracellular osmolarity, and $c_n^0 = \{c_{Na}^0, c_K^0, c_{Cl}^0, c_H^0, c_{HCO_3}^0, c_A^0, c_{Buf}^0, c_{HBuf}^0\}^T$ is the extracellular osmolarity.

We treated Na^+, K^+, and Cl^- as non-reactive ion species, and the their conservation is written as

$$\frac{d}{dt}(Vc_n) = 4\pi r^2 J_n, n \in \{Na^+, K^+, Cl^-\}, \quad \text{(Equation 3)}$$

where J_n is the net ion flux across the cell membrane for each species through active and passive ion transporters, and $V = 4/3\pi r^3$ is the cell volume. The conservation equation for the intracellular reactive species is

$$\frac{d}{dt}(Vc_{\mathrm{H}}) - 4\pi r^2 J_{\mathrm{H}} = \frac{d}{dt}(Vc_{\mathrm{HCO_3}}) - 4\pi r^2 J_{\mathrm{HCO_3}} + \frac{d}{dt}(Vc_{\mathrm{Buf}}). \quad \text{(Equation 4)}$$

We considered the following ion transporters: passive Na^+, K^+, and Cl^- channels, Na^+-K^+-Cl^- co-transporter (NKCC), Na^+-K^+ ATPase (NKA), Na^+-H^+ exchanger (NHE), Na^+-HCO_3^- co-transporter (NBC), and anion exchange protein 2 (AE2). The net flux for each ion species is modeled as the sum of fluxes through the relevant transporters:

$$J_{\mathrm{Na}} = J_{\mathrm{Na},p} + J_{\mathrm{NKCC,Na}} + J_{\mathrm{NKA,Na}} + J_{\mathrm{NHE,Na}} + J_{\mathrm{NBC,Na}}, \quad \text{(Equation 5)}$$

$$J_{\mathrm{K}} = J_{\mathrm{K},p} + J_{\mathrm{NKCC,K}} + J_{\mathrm{NKA,K}}, \quad \text{(Equation 6)}$$

$$J_{\mathrm{Cl}} = J_{\mathrm{Cl},p} + J_{\mathrm{NKCC,Cl}} + J_{\mathrm{AE2,Cl}}, \quad \text{(Equation 7)}$$

$$J_{\mathrm{H}} = J_{\mathrm{NHE,H}}, \quad \text{(Equation 8)}$$

$$J_{\mathrm{HCO_3}} = J_{\mathrm{AE2,HCO_3}} + J_{\mathrm{NBC,HCO_3}}. \quad \text{(Equation 9)}$$

Passive ion transporters are typically gated by the membrane electrochemical potential or the membrane tension, and thus we modeled the passive ion fluxes as

$$J_{n,p} = \alpha_{n,p} G_m (RT \ln \Gamma_n - z_n F V_m), n \in \{\mathrm{Na^+}, \mathrm{K^+}, \mathrm{Cl^-}\} \quad \text{(Equation 10)}$$

where V_m is the membrane potential, z_n is the valence of each ion species, $\Gamma_n = c_n^0/c_n$ is the ratio of extra-to intra-cellular ion concentrations, $\alpha_{n,p}$ is the permeability coefficient of each species, and $G_m = [1 + e^{-\beta_1(\tau_m - \beta_2)}]^{-1} \in \{0, 1\}$ is a mechanosensitive gating function. NKCC flux is modeled as

$$J_{\mathrm{NKCC}} = J_{\mathrm{NKCC,Na}} = J_{\mathrm{NKCC,K}} = \frac{1}{2} J_{\mathrm{NKCC,Cl}} = \alpha_{\mathrm{NKCC}} RT (\ln \Gamma_{\mathrm{Na}} + \ln \Gamma_{\mathrm{K}} + 2 \ln \Gamma_{\mathrm{Cl}}), \quad \text{(Equation 11)}$$

where α_{NKCC} is the permeability coefficient independent of the cortical tension. NHE is modeled as a pH gated function:

$$J_{\mathrm{NHE}} = J_{\mathrm{NHE,Na}} = -J_{\mathrm{NHE,H}} = \alpha_{\mathrm{NHE}} G_{\mathrm{NHE}} RT (\ln \Gamma_{\mathrm{Na}} - \ln \Gamma_{\mathrm{H}}), \quad \text{(Equation 12)}$$

where α_{NHE} is the permeability coefficient of NHE, which is assumed as a constant. $G_{\mathrm{NHE}} = [1 + e^{\beta_{\mathrm{NHE},1}(\mathrm{pH} - \beta_{\mathrm{NHE},2})}]^{-1}$ is a pH-gated function of NHE. Ion fluxes through AE2 takes a similar form:

$$J_{\mathrm{AE2}} = J_{\mathrm{AE2,Cl}} = -J_{\mathrm{AE2,HCO_3}} = \alpha_{\mathrm{AE2}} G_{\mathrm{AE2}} RT (\ln \Gamma_{\mathrm{Cl}} - \ln \Gamma_{\mathrm{HCO_3}}), \quad \text{(Equation 13)}$$

where α_{AE2} is the permeability coefficient of AE2 that is assumed to be a constant, and $G_{\mathrm{AE2}} = [1 + e^{-\beta_{\mathrm{AE2},1}(\mathrm{pH} - \beta_{\mathrm{AE2},2})}]^{-1}$ is the pH-gated function of AE2. Ion fluxes through NBC depends on the electrochemical potential of Na^+ and HCO_3, which is modeled as

$$J_{\mathrm{NBC}} = J_{\mathrm{NBC,Na}} = -\frac{1}{2} J_{\mathrm{NBC,HCO_3}} = \alpha_{\mathrm{NBC}} \left[RT \ln \left(\Gamma_{\mathrm{Na}} \Gamma_{\mathrm{HCO_3}}^2 \right) - (z_{\mathrm{Na}} + 2 z_{\mathrm{HCO_3}}) F V_m \right], \quad \text{(Equation 14)}$$

where α_{NBC} is the permeability coefficient of NBC. Ion fluxes through NKA is modeled as

$$J_{\mathrm{NKA}} = J_{\mathrm{NKA,Na}} = -\frac{3}{2} J_{\mathrm{NKA,K}} = -\alpha_{\mathrm{NKA}} G_{V,\mathrm{NKA}} \left(1 + \beta_{\mathrm{NKA,Na}} \Gamma_{\mathrm{Na}}\right)^{-3} \left(1 + \frac{\beta_{\mathrm{NKA,K}}}{\Gamma_{\mathrm{K}}}\right)^{-2}, \quad \text{(Equation 15)}$$

where α_{NKA} is the permeability coefficient of NKA, $\beta_{\mathrm{NKA,Na}}$ and $\beta_{\mathrm{NKA,K}}$ are scaling constant for Γ_{Na} and Γ_{K}, respectively. $G_{V,\mathrm{NKA}} = 2[1 + e^{-\beta_{\mathrm{NKA},1}(V_m - \beta_{\mathrm{NKA},2})}]^{-1}$ is the voltage-gated activity function of NKA.

Inside the cell, we modeled the bicarbonate-carbonic acid equilibrium as

$$\mathrm{CO_2(aq) + H_2O(l) \leftrightharpoons H^+(aq) + HCO_3^-(aq)},$$

where $[CO_2]_{\mathrm{aq}}$ depends on the partial pressure of CO_2, P_{CO_2}, by Henry's constant, k_H, i.e., $[CO_2]_{\mathrm{aq}} = P_{CO_2}/k_H$. For intracellular pH, we have

$$\mathrm{pH} - \mathrm{p}K_c = \log_{10} \frac{[\mathrm{HCO_3^-}]_{\mathrm{aq}}}{[\mathrm{CO_2}]_{\mathrm{aq}}},$$

where $pH = -\log_{10}[H^+]_{aq}$ is the intracellular pH, $K_c = [HCO_3^-]_{aq}[H^+]_{aq}/[CO_2]_{aq}$ is the equilibrium constant for the bicarbonate-carbonic acid pair, and $pK_c = -\log_{10}K_c$. Cells also contain various buffer solutions, and their reactions can be written as

$$H_\ell Buf(aq) \leftrightharpoons \ell H^+(aq) + Buf^{\ell-}(aq),$$

where $\ell = 1, 2, 3, \ldots$ for different buffer species. $K_{B,\ell} = [Buf^{\ell-}]_{aq}[H^+]^\ell_{aq}/[H_\ell Buf]_{aq}$ is the equilibrium constant, and $pK_{B,\ell} = -\log_{10}K_{B,\ell}$. We set $\ell = 1$ by default.We also assume both the intracellular and the extracellular are electro-neutral, which is realized by enforcing $\sum z_n c_n = 0$.

Overall, the full set of equations is as follows:

$$\frac{dr}{dt} = J_{water} = -\alpha_W\left[\frac{2h\sigma}{r} - RT\left(\sum c_n - \sum {}^0_n c\right)\right], \quad \text{(Equation 16)}$$

$$\sum z_n c_n = 0, \quad \text{(Equation 17)}$$

$$\frac{d}{dt}(Vc_{Na}) = 4\pi r^2(J_{Na,p} + J_{NKCC} + J_{NKA} + J_{NHE} + J_{NBC}), \quad \text{(Equation 18)}$$

$$\frac{d}{dt}(Vc_K) = 4\pi r^2\left(J_{K,p} + J_{NKCC} - \frac{2}{3}J_{NKA}\right), \quad \text{(Equation 19)}$$

$$\frac{d}{dt}(Vc_{Cl}) = 4\pi r^2(J_{Cl,p} + 2J_{NKCC} + J_{AE2}), \quad \text{(Equation 20)}$$

$$\frac{d}{dt}(Vc_H) + 4\pi r^2 J_{NHE} = \frac{d}{dt}(Vc_{HCO_3}) + 4\pi r^2(J_{AE2} - 2J_{NBC}) + \frac{d}{dt}(Vc_{Buf}), \quad \text{(Equation 21)}$$

We solved 6 unknowns, $r, V_m, c_{Na}, c_K, c_{Cl}$ and pH from Equations 16, 17, 18, 19, 20, and 21. Other parameters are derived either from give quantities or from the unknowns. Details can be found in Li et al. (2021).[42]

All systems were initialized at the same condition, then we allowed each system to evolve to a steady state. The generic parameters that applicable to all cell types used in this work can found in Table S1. The hypotonic shock was applied by reducing 50% of the extracellular species concentration. The inhibition of NHE and NKA was conducted by reducing their permeability coefficients by 90%.

Model parameterization

The expression and activity of membrane ion transporters vary among different cell types, and the response of cells to osmotic shocks depends on their overall ion transporter activities.[42] For example, from our experimental data, HT1080 and 3T3 cells display different levels of volume recovery after a hypotonic shock. However, in some cases, no volume recovery is observed unless parameters are adjusted following the application of a hypotonic shock.[42]

To systematically investigate the impact of ion transporter activity on cell volume regulation during hypotonic shock, we employed a Monte Carlo search of widely-reported volume-regulated transporters, including NHE, NKCC, NKA, and passive Na, Cl, and K channels. Each parameter was randomly varied between 10^{-2} and 10^2 times its baseline value, where the baseline value represents the typical level observed in a mammalian tissue cell exhibiting stable homeostasis. The baseline values for each transporter are listed in Table S2, where $P_0 = 3\times10^{-9}$ mol^2/(J • m^2 s) is the overall scaling factor. The rest of the parameters are provided in Table S1.

Using our experimental findings, we first identified ion transporter activities that result in (50 ± 5)% cell volume recovery after hypotonic shock, as shown in Figure S11A. The activity level of each transporter is normalized to its corresponding baseline value. We then conducted a principal component analysis (PCA) to examine the relative importance of ion transporters in controlling regulatory volume recovery. The first 6 principle components (PCs) explains the majority of the variance (Figure S11B), indicating that ion transporter activities that mainly project onto these PCs are potentially less important since they do not need to be kept within a specific range. Therefore, we focused on the last 3 PCs and plotted the eigenvectors of the covariance matrix of all six ion transporters in Figure S11C. We found that among active ion transporters, PCs 7–9 are mainly contributed by NHE and NKA. This observation suggests that the activities of NHE and NKA are two key parameters for regulatory volume recovery, while NKCC, NBC, and AE2 plays a less significant role. This finding is in agreement with our experimental observations. Among passive ion channels, the Na channels is the major contributor to PCs 7–9. We also plotted the projections of ion transporter parameters onto PCs 7–9 (Figures S11D and S11E).

Using our experimental data, we have identified sets of membrane ion transporter activities that are representative of HT1080 and 3T3 cells. These parameters, which are derived from random simulations, are listed in Table S3, along with the remaining parameters provided in Table S1.[13,98–101] Their projections on PCs 4–6 are highlighted in Figures S11D and S11E. It is important to note that the

parameters in Table S3 represent the activity levels of the ion transporters, rather than their RNA expression levels. The activity levels are function of ion transporter expression as well as their activation by voltages, tension, and $[Ca^{2+}]$. These parameters are used to model the changes in cell volume following hypotonic shocks as depicted in the main text.

Modeling secondary volume increase in 3T3 cells

The volume response of 3T3 cells exhibits a secondary volume increase (SVI) after a hypotonic shock. Based on our modeling, it is not possible to directly produce the SVI by solely adjusting parameters. This suggests the existence of additional activation mechanisms contributing to the SVI. As discussed in the main text, we attribute the additional volume increase to the activation of NHE following the initial volume recovery in response to the hypotonic shock. To incorporate this phenomenon into the model, we artificially introduced an NHE activation function in the 3T3 cells by prescribing an amplitude adjustment factor, $A(t)$, to the NHE flux expression in Equation 12.

This normalized factor is chosen by

$$A(t) = 1 + \gamma_1(t - t_a)e^{-\gamma_2 t}, \quad \text{(Equation 22)}$$

where γ_1 and γ_2 are constant that modulate the amplitude of the SVI. We set $\gamma_1 = 1\ s^{-1}$ and $\gamma_2 = 1\times10^{-3}\ s^{-1}$ as a reference value based on the experimental data. The parameter t_a represents the activation time of the SVI. The additional NHE activation is triggered at the same time as the hypotonic shock, as we assume that NHE is activated as the cell swells in response to the shock. This activation factor is only applied to the control and NHE inhibition results; it is not included in the NKA inhibition results.

QUANTIFICATION AND STATISTICAL ANALYSIS

For time series plots, error bars represent the mean and the standard error of mean of at least 3 biological repeats. The number of cells analyzed per condition were noted in the plots or in the captions. Mann–Whitney U-tests were used comparing two conditions at each time points after osmotic shock or mechanical stretch, and the p values were plotted as a function of time in Figures S13–S15. For scatterplots, error bars represent the mean and the standard deviation of at least 3 biological repeats. Shapiro–Wilk tests were used for normality testing in cases in which the number of data points was between 3 and 8. D'Agostino–Pearson omnibus normality test was used to determine whether data were normally distributed with > 8 data points. For Gaussian distribution, Student's T test was used. For non-Gaussian distributions, nonparametric Mann–Whitney U-tests were used comparing two conditions, and comparisons for more than two groups were performed using Kruskal–Wallis tests followed by Dunn's multiple-comparison test. The statistical analysis was conducted using MATLAB 2021b (Mathworks), or GraphPad Prism 9 or 10 (GraphPad Software). Statistical significance was identified as $p < 0.05$. ns for $p > 0.05$, *$p < 0.05$, **$p < 0.01$, ***$p < 0.001$ and ****$p < 0.0001$.

Cell Reports, Volume *43*

Supplemental information

Cytoskeletal activation of NHE1 regulates mechanosensitive cell volume adaptation and proliferation

Qin Ni, Zhuoxu Ge, Yizeng Li, Gabriel Shatkin, Jinyu Fu, Anindya Sen, Kaustav Bera, Yuhan Yang, Yichen Wang, Yufei Wu, Ana Carina Nogueira Vasconcelos, Yuqing Yan, Dingchang Lin, Andrew P. Feinberg, Konstantinos Konstantopoulos, and Sean X. Sun

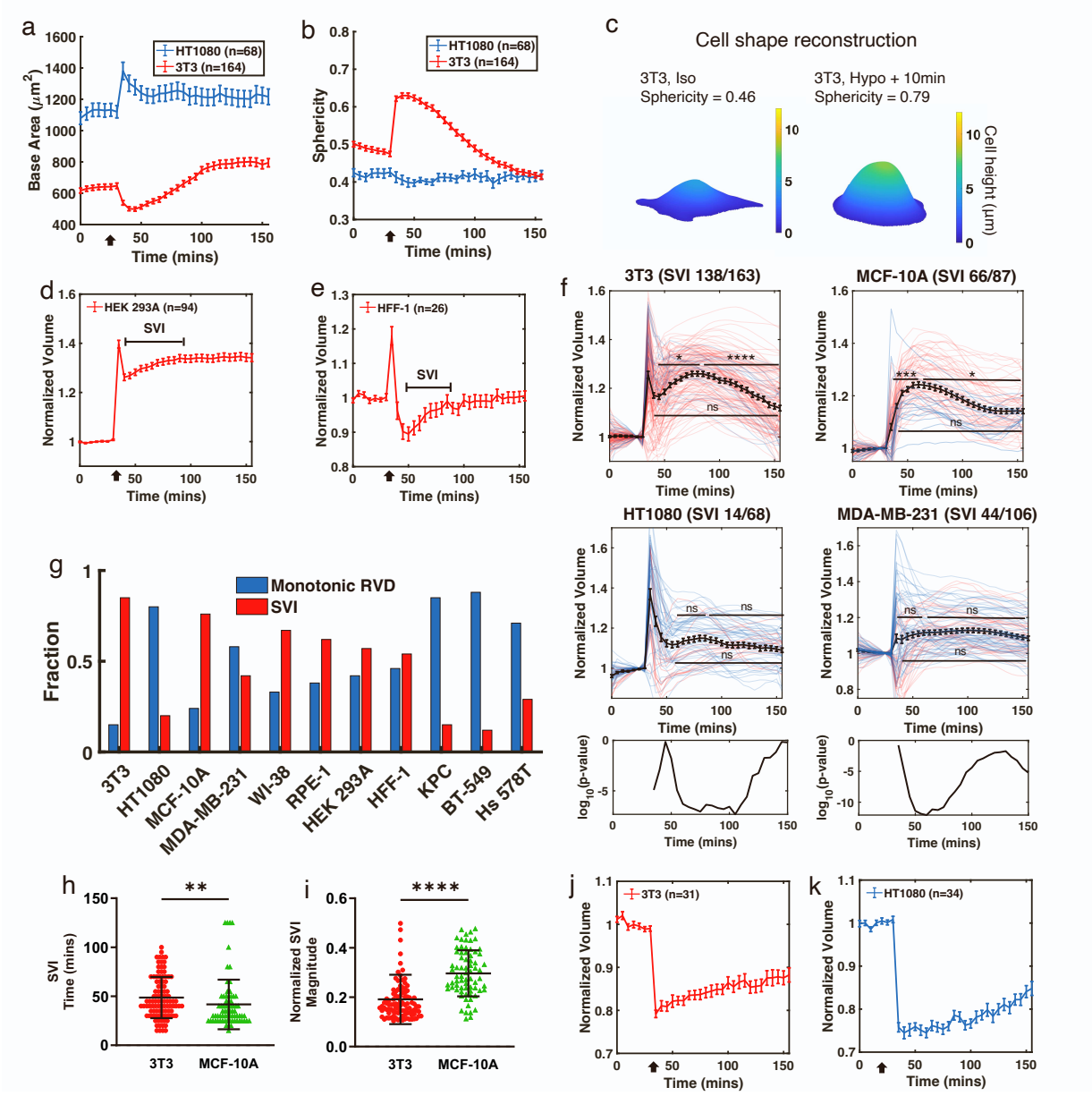

Figure S1: **Hypotonic shock induced cell area and shape changes, cell volume variations, and volume changes during hypertonic shock.**

Figure S1: Hypotonic shock induced cell area, shape, and volume changes, SVI variation and statistical significance, and hypertonic shock. (a) Cell base area dynamics during hypotonic shock applied at 30 min. (b) Cell sphericity during hypotonic shock. Sphericity is calculated as $\frac{\pi^{\frac{1}{3}}(6V)^{\frac{2}{3}}}{A_{surface}}$. Surface area $A_{surface}$ is calculated from cell shape reconstruction based on FXm. (c) Representative 3D reconstruction of cell shape from FXm. (d, e) Cell volume tracking of HEK 293A (d) and HFF-1 (e) before and after hypotonic shock. (f) Normalized single cell volume trajectories of 3T3, HT1080, MCF-10A, and MDA-MB-231 before and after hypotonic shock. Cells display at least 10% SVI after initial RVD are considered as a SVI type and are marked in red, and others cells are marked in blue. Mann-Whitney U tests were conducted among the following time points within each cell lines: the first time points after initial RVD (15 min after shock for 3T3, 25 min for HT1080, and 5 min for MCF-10A and MDA-MB-231), the peak of SVI (50 min after shock for 3T3 and HT1080, and 30 min for MCF-10A and MDA-MB-231), and the last time point (2 h after shock). The bottom panels are p-value as a function of time between two pairs of cells: 3T3 versus HT1080 (left) and MCF-10A versus MDA-MB-231 (right) at each time point after shock. ****p<0.0001, ***p<0.001, **p<0.01, and ns p>0.05. (g) The fraction of cells showing monotonic RVD and SVI in all cell lines tested. (h, i) The time (h) and magnitude (i) of the SVI in 3T3 and MCF-10A. (j,k) 3T3 (j) and HT1080 (k) volume dynamics with 50% hypotonic shock at 30 min. (a, b, i, j) Error bars indicates standard error of mean (SEM). (f, g) Error bars indicates standard deviation. Mann-Whitney U tests were conducted.

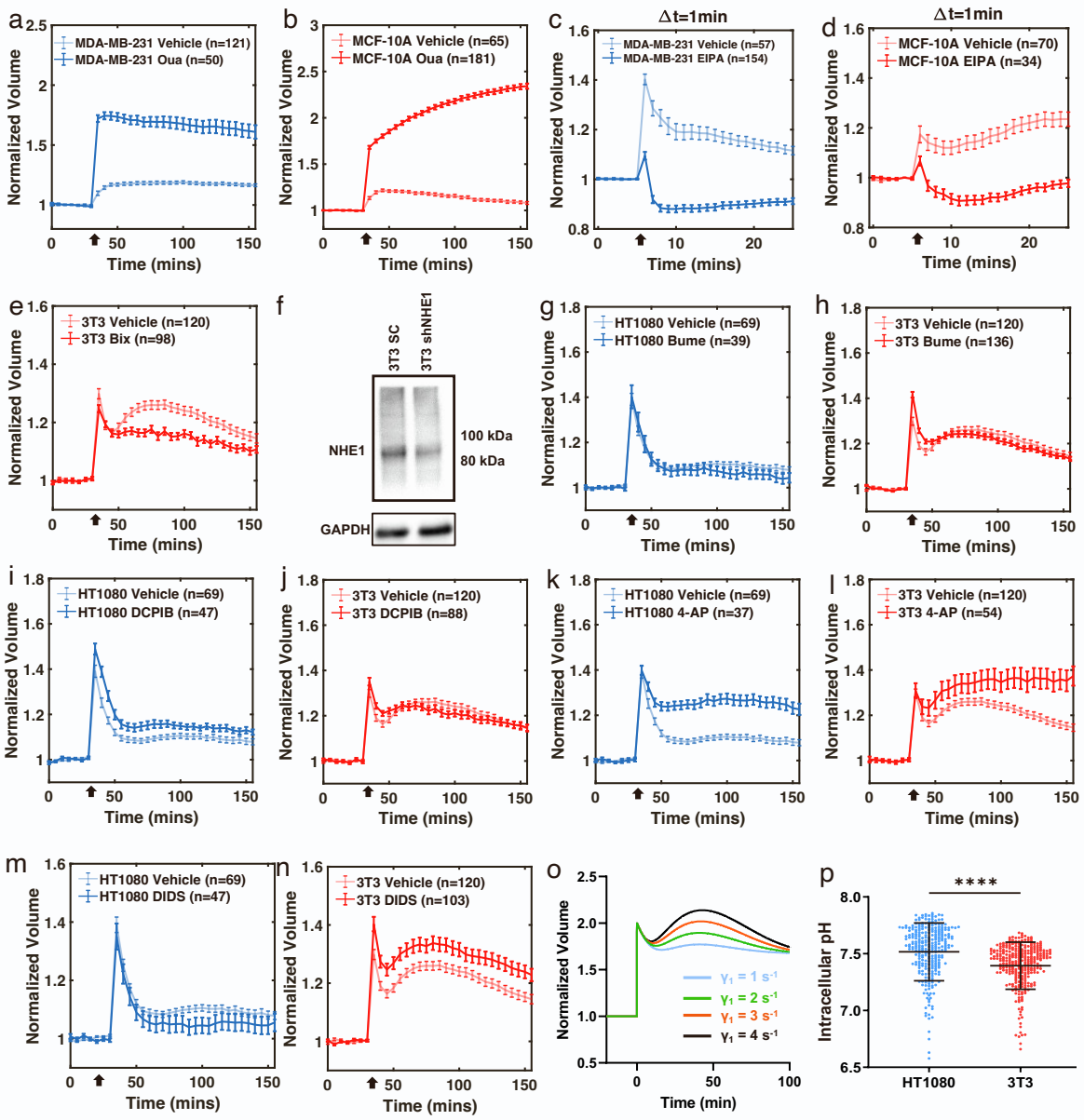

Figure S2: **The effects of Na^+-K^+ flux in regulating cell volume.** (a, b) Oua treated MDA-MB-231 (a) and Mcf-10a (b) volume dynamics under hypotonic shock. (c, d) EIPA treated MDA-MB-231 (c) and Mcf-10a (d) volume dynamics under hypotonic shock (applied at 5 min). Frame rate is 1 min. (e) Bix treated 3T3 volume dynamics under hypotonic shock. (f) Representative western blot from 3T3 transduced with shRNA sequences to NHE1 or a noncoding scramble control (SC) sequence. (g-n) Volume dynamics of 3T3 and HT1080 treated Bume (g for HT1080, h for 3T3), DCPIB (i for HT1080, j for 3T3), 4-AP (k for HT1080, l for 3T3), or DIDS treatment (m for HT1080, n for 3T3). (o) Simulated 3T3 volume dynamics with different NHE activation functions. (p) Intracellular pH of HT1080 and 3T3 at homeostasis. n = 291 and 206, respectively. Error bars indicate standard deviation. Mann-Whitney U tests. (a-e, g-n) Error bars indicate SEM.

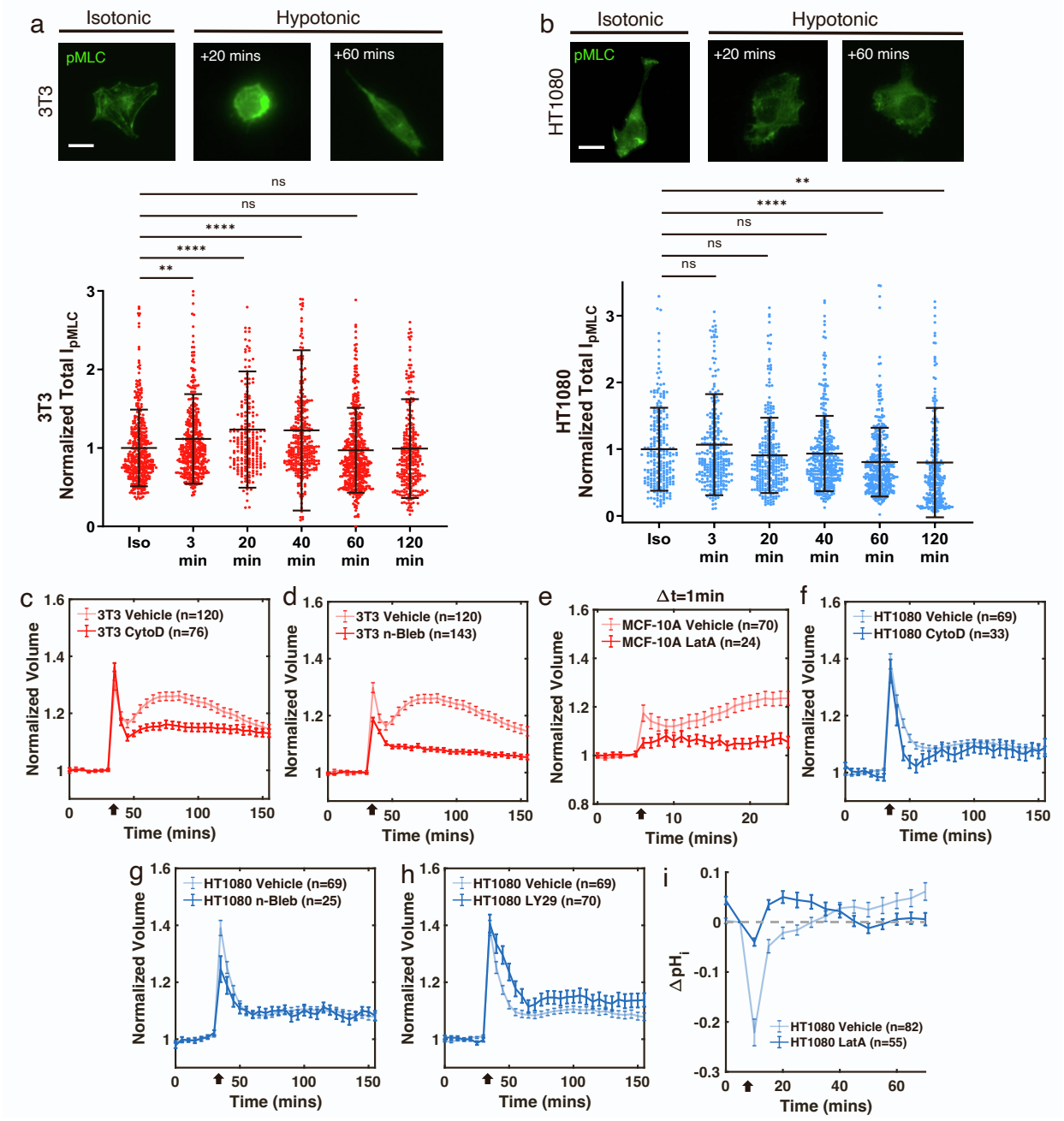

Figure S3: **Hypotonic shock induces changes in pohospho-myosin light chain activity and volume dynamics after actomyosin disruption.** (a, b) Representative immunofluorescent images of pohospho-myosin light chain (pMLC) and quantifications of 3T3(a) and HT1080 (b). In the quantifications, epi-fluorescence microscopy was used to obtain the total fluorescence intensity of pMLC. Cells were fixed in isotonic media, and 3, 20, 40, 60 and 120 min after hypotonic shock. For 3T3 (a), n = 405, 401, 216, 330, 441, 287. For HT1080 (b), n = 224, 283, 296, 358, 366, 284. Error bars indicate standard deviation. Kruskal–Wallis tests followed by Dunn's multiple-comparison test. (c, d) CytoD (c) and n-Bleb (d) treated 3T3 volume dynamics under hypotonic shock. (e) LatA treated MCF-10A volume dynamics under hypotonic shock. Frame rate = 1min. (f-h) CytoD (f), n-Bleb (g), and LY29 (h) trated HT1080 volume dynamics under hypotonic shock. (i) $\Delta pH_i$for LatA treated HT1080 and vehicle control under hypotonic shock. (c-i) Error bars indicate SEM. (a, b) Scale bars, 20 μm.

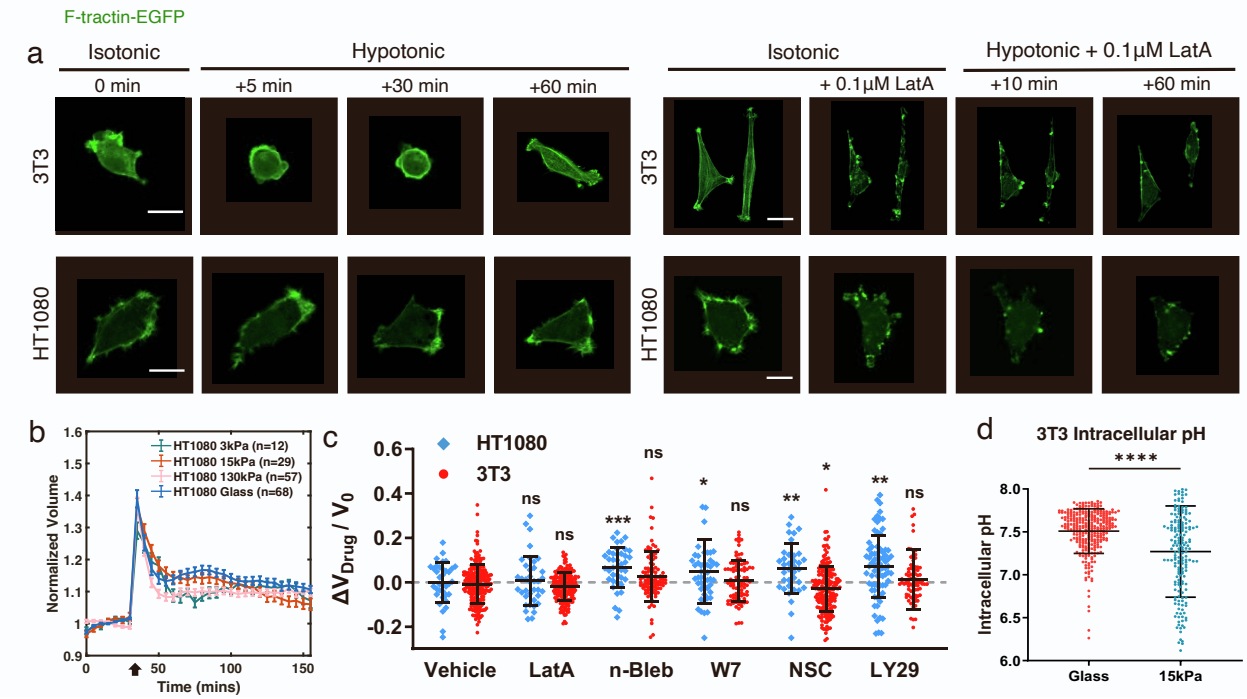

Figure S4: **3T3 and HT1080 volume and actin dynamics change under actomyosin disruption or grown on varied substrate stiffness.** (a) Confocal images of EGFP-F-tractin transfected 3T3 and HT1080 with or without subjected to LatA treatment before and hypotonic shock. (b) HT1080 volume dynamics during hypotonic shock on 3, 15, and 130 kPa PDMS substrates and on glass. Error bars indicate SEM. (c) Fractional cell volume changes under vehicle control and drugs for cytoskeleton: Latrunculin A (LatA, dissembling actin network), para-nitro-blebbistatin (n-Bleb, Myosin II inhibitor), W7 (blocking Calmodulin - Ca^{2+} binding), and NSC668394 (NSC, blocking ezrin-actin binding). $n_{HT1080} = 36, 190, 40, 46, 36, 77$, and $n_{3T3} = 213, 38, 102, 89, 202, 84$, respectively. Error bars indicate standard deviation. Kruskal–Wallis tests followed by Dunn's multiple-comparison were conducted between data sets and the vehicle control of the corresponding cell type. (d) Intracellular pH measured by pHrodo-red AM for 3T3 grown on glass and 15kPa PDMS substrates. Error bars indicate standard deviation, and Mann-Whitney U test was conducted. n= 306 and 192, respectively. (a) Scale bar, 20 μm.

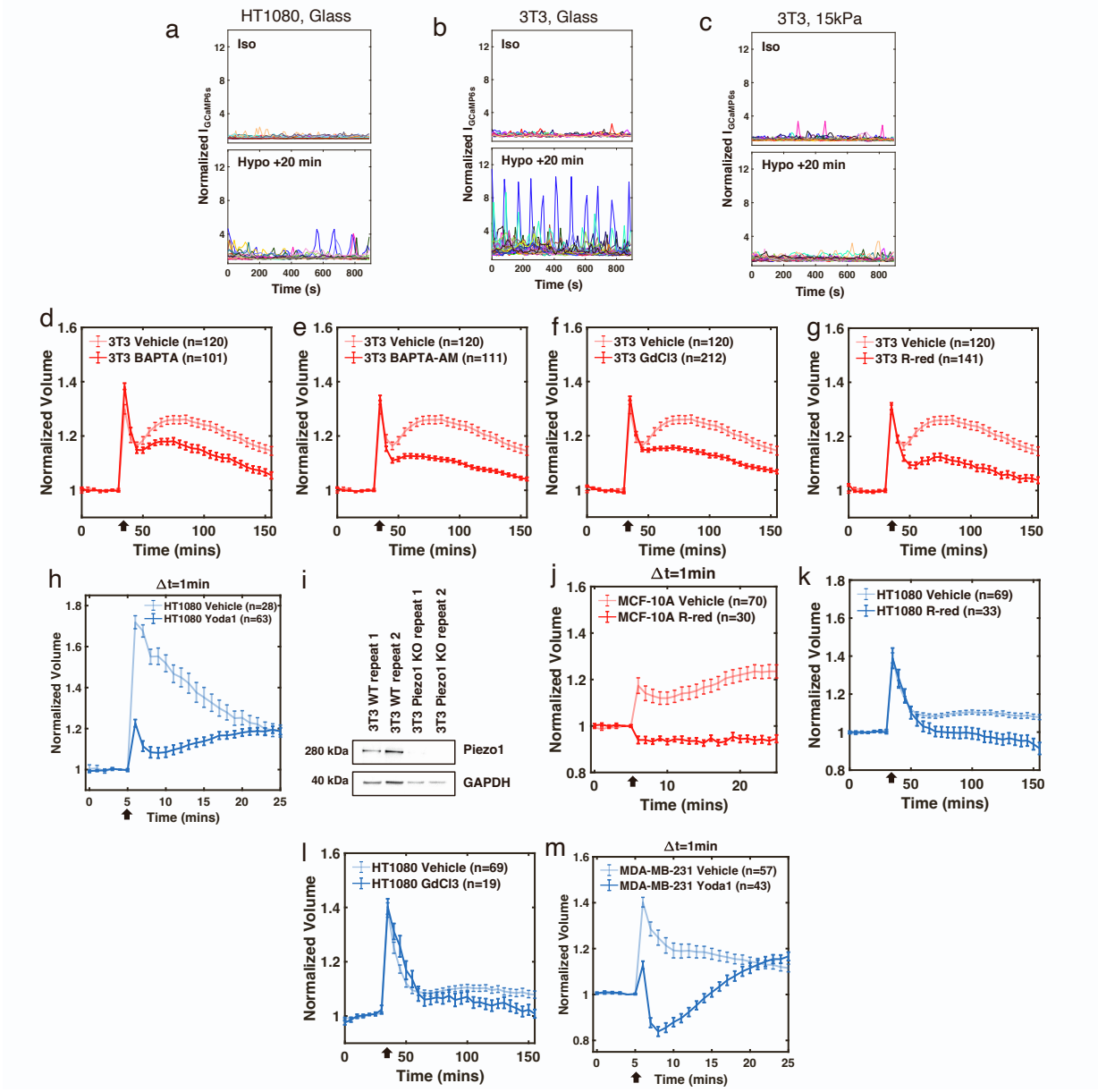

Figure S5: **Ca^{2+} signaling affects cell volume regulation.** (a-c) Single-cell GCaMP6s dynamics in isotonic media (upper) and 20 min after hypotonic shock (lower) for HT1080 grown on glass (a), 3T3 grown on glass (b), and 3T3 grown on 15 kPa (c). Imaged at 10 s frame rate. (d-g) BAPTA (d), BAPTA-AM (e), $GdCl_3$ (f), and R-red (g) treated 3T3 volume dynamics under hypotonic shock. (h) HT1080 volume dynamics with Yoda1 added together with hypotonic solution at 5 min. (i) Representative western blots showing Piezo1 levels in 3T3 WT and Piezo1 CRISPR knockout cells. (j) R-red treated MCF-10A volume dynamics under hypotonic shock applied at 5 min. Frame rate is 1 min. (k-l) R-red (k) and $GdCl_3$ (l) treated HT1080 volume dynamics under hypotonic shock. (m) MDA-MB-231 volume dynamics with Yoda1 added together with hypotonic solution at 5 min. (a, d-h, j-m) Error bars indicate SEM.

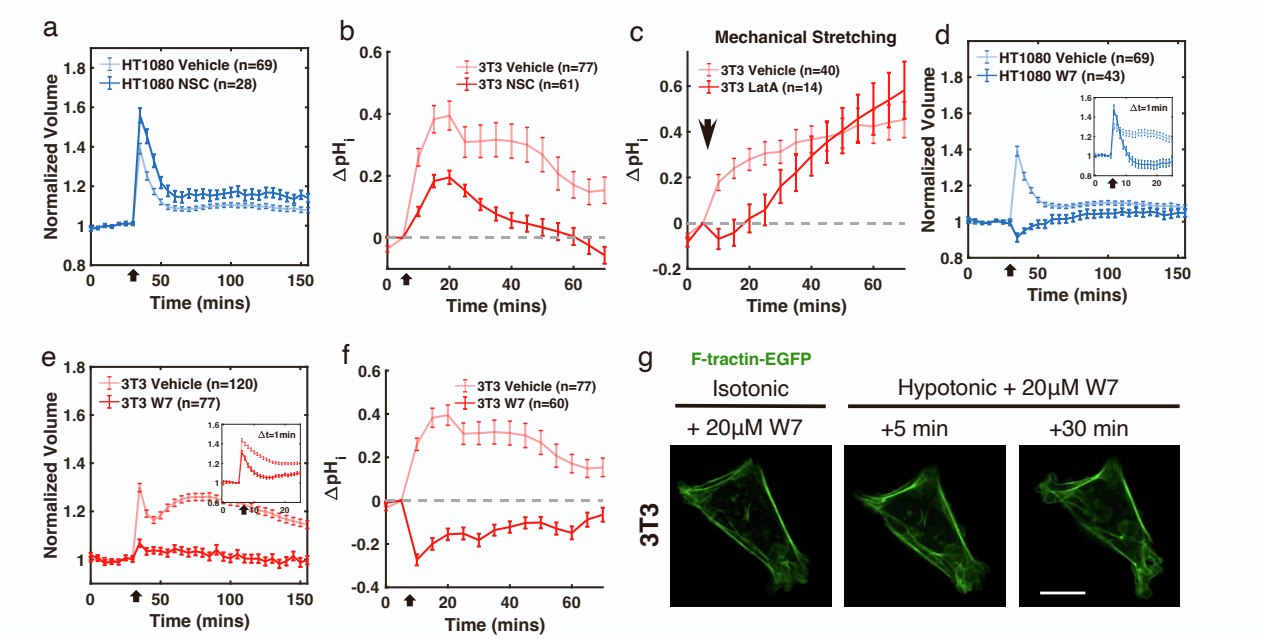

Figure S6: **Ca^{2+}, calmodulin and ezrin affect cell volume regulation.** (a) NSC treated HT1080 volume dynamics under hypotonic shock. (b-c) $\Delta pH_i$for NSC treated 3T3 under hypotonic shock (b) and 20% uniaxial mechanical stretch (c). (d, e) W7 treated HT1080 (d) and 3T3 (e) volume dynamics under hypotonic shock. Insets have 1 min frame rate (HT1080 Vehicle n = 53, W7 = 20, and 3T3 Vehicle n = 42, W7 n = 46). (f) $\Delta pH_i$for W7 treated 3T3 under hypotonic shock. (g) 3T3 expressing F-tractin with W7 treatment before and after hypotonic shock. (a-f) Error bars indicate SEM. (g) Scale bar, 20 μm.

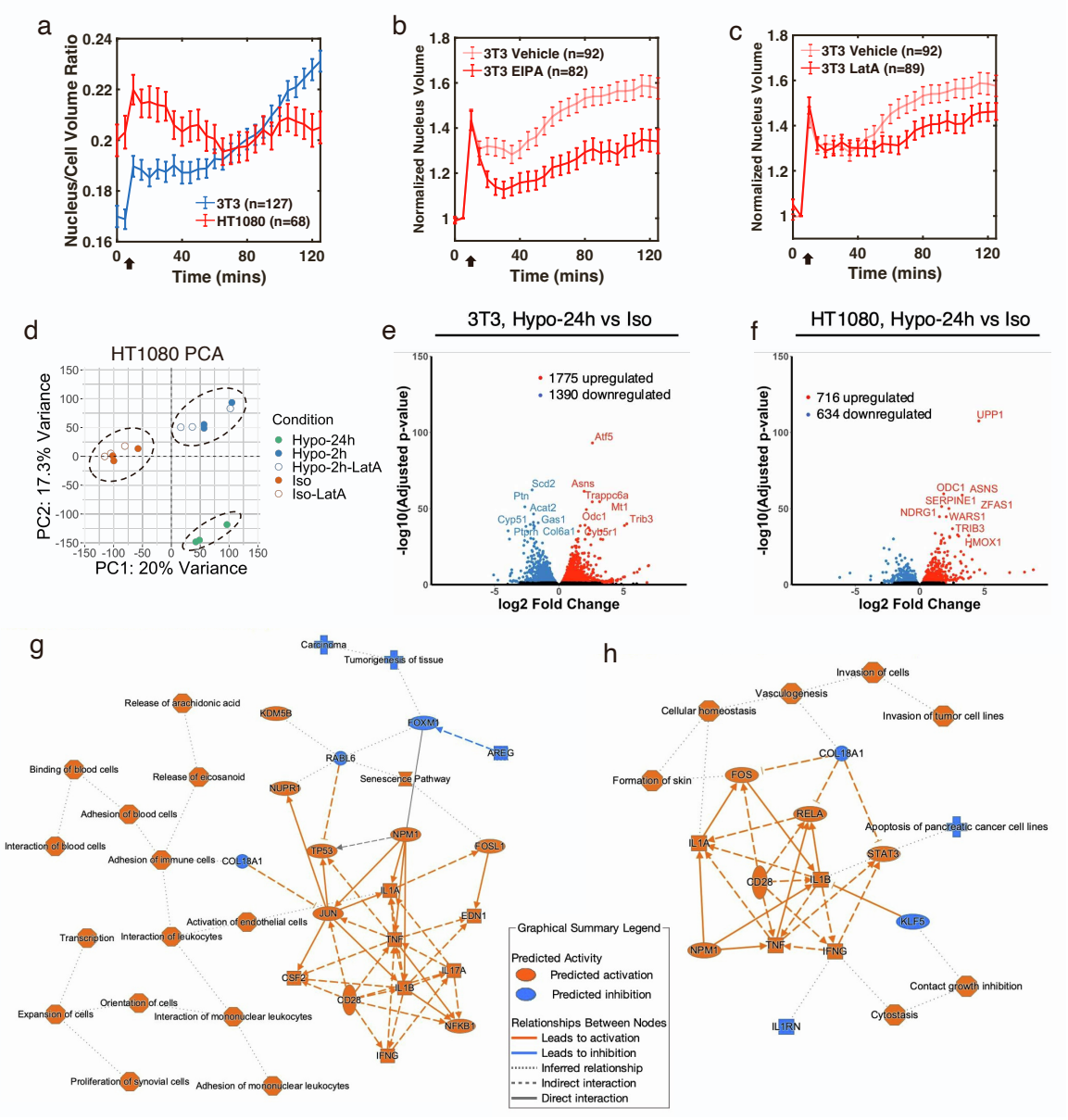

Figure S7: **Hypotonic shock induces nucleus deformation and transcriptomic changes.** (a) Nucleus to cell volume (N/C) ratio of 3T3 and HT1080 with hypotonic shock applied at 5 min. (b-c) Normalized nucleus volume of 3T3 vehicle *versus* treated with EIPA (b) and LatA (c) with hypotonic shock applied at 5 min. (a-c) Error bars indicate SEM. (d) Principle component analysis (PCA) for HT1080 before and after hypotonic shock and with or without LatA treatment. N = 3 biological repeats. (e, f) Volcano plots showing differentially expressed genes (DEGs) at 24-hour hypotonic shock versus in isotonic media for 3T3 (e) and HT1080 (f). (g, h) Summaries of pathways during 2-hour hypotonic shock for 3T3 (g) and HT1080 (h) using Ingenuity Pathway Analysis .

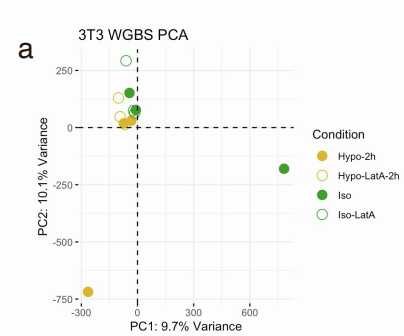

b

Comparison	Hypomethylated DEG-DMRs	Hypermethylated DEG-DMRs	Total DEG-DMRs
Hypotonic 2hr vs Isotonic	284	720	1004
Hypotonic 2hr LatA vs Hypotonic	47	36	83
Isotonic LatA vs Isotonic	59	58	117
Hypotonic 2hr LatA vs Hypotonic (exclusive)	23	28	51
Isotonic LatA vs Isotonic (exclusive)	42	39	81

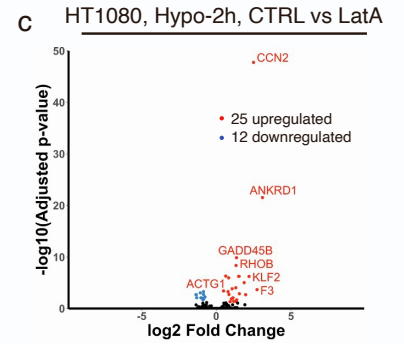

d

Gene	Log 2 Fold Change	Adjusted P-value
RUNX1	1.71	5.21×10^{-13}
NFKB1	0.61	3.63×10^{-5}
CEBPD	0.44	0.02

Figure S8: **DNA methylation and HT1080 RNAseq.** (a) Principle component analysis (PCA) of 3T3 WGBS data before and after 2 h hypotonic shock and with or without LatA treatment. N = 3 biological repeats. (b) Summary of the number of DEG-DMRs comparing all conditions from 3T3 WGBS data. (c) Volcano plots showing DEGs at 2-hour hypotonic shock control versus LatA treatment for HT1080. (d) Differential expression of select transcription factors between Hypotonic 2 h and Isotonic cells.

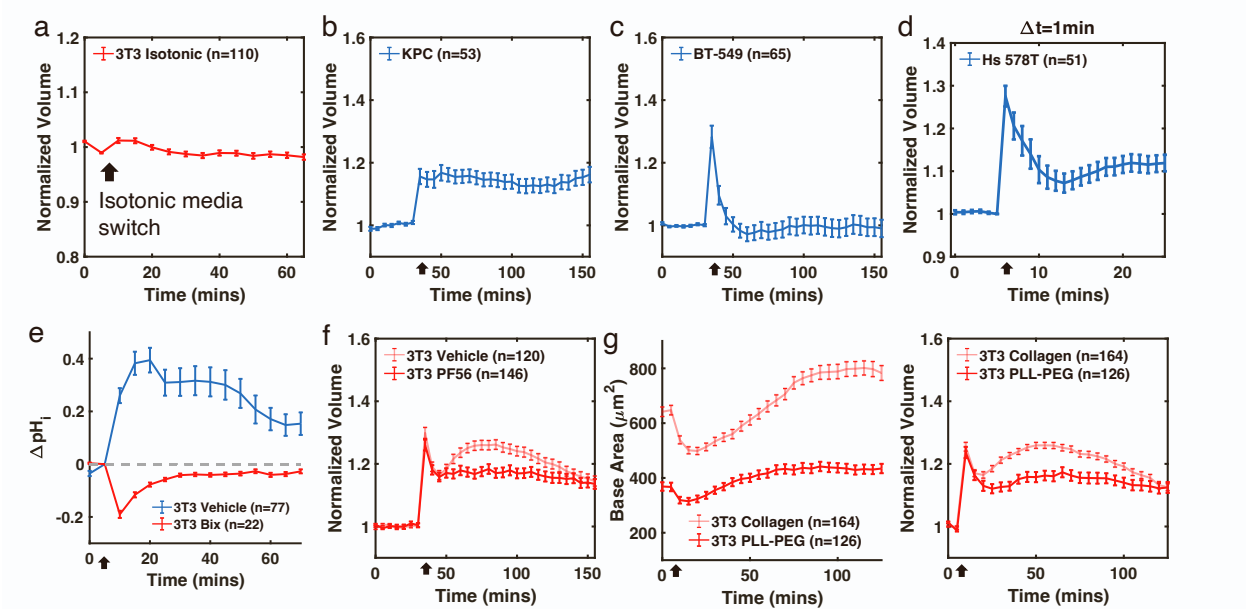

Figure S9: **Cell volume and pH change under media switch, hypotonic shock, and drug inhibition.** (a) 3T3 cell volume change with isotonic media switch applied at 5 min in FXm chamber. (b-d) Cell volume tracking of KPC (b), BT-549 (c), and Hs 578T (d) before and after hypotonic shock. (d) Imaged at 1 min frame rate. (e) $\Delta pH_i$for Bix treated 3T3 and vehicle control under hypotonic shock. (f) Volume dynamics of 3T3 treated with PF56 and vehicle control under hypotonic shock. (g) Base area (left) and volume (right) dynamics of 3T3 plated on PLL-PEG coated versus collagen coated FXm devices. (a-g) Error bars indicate SEM.

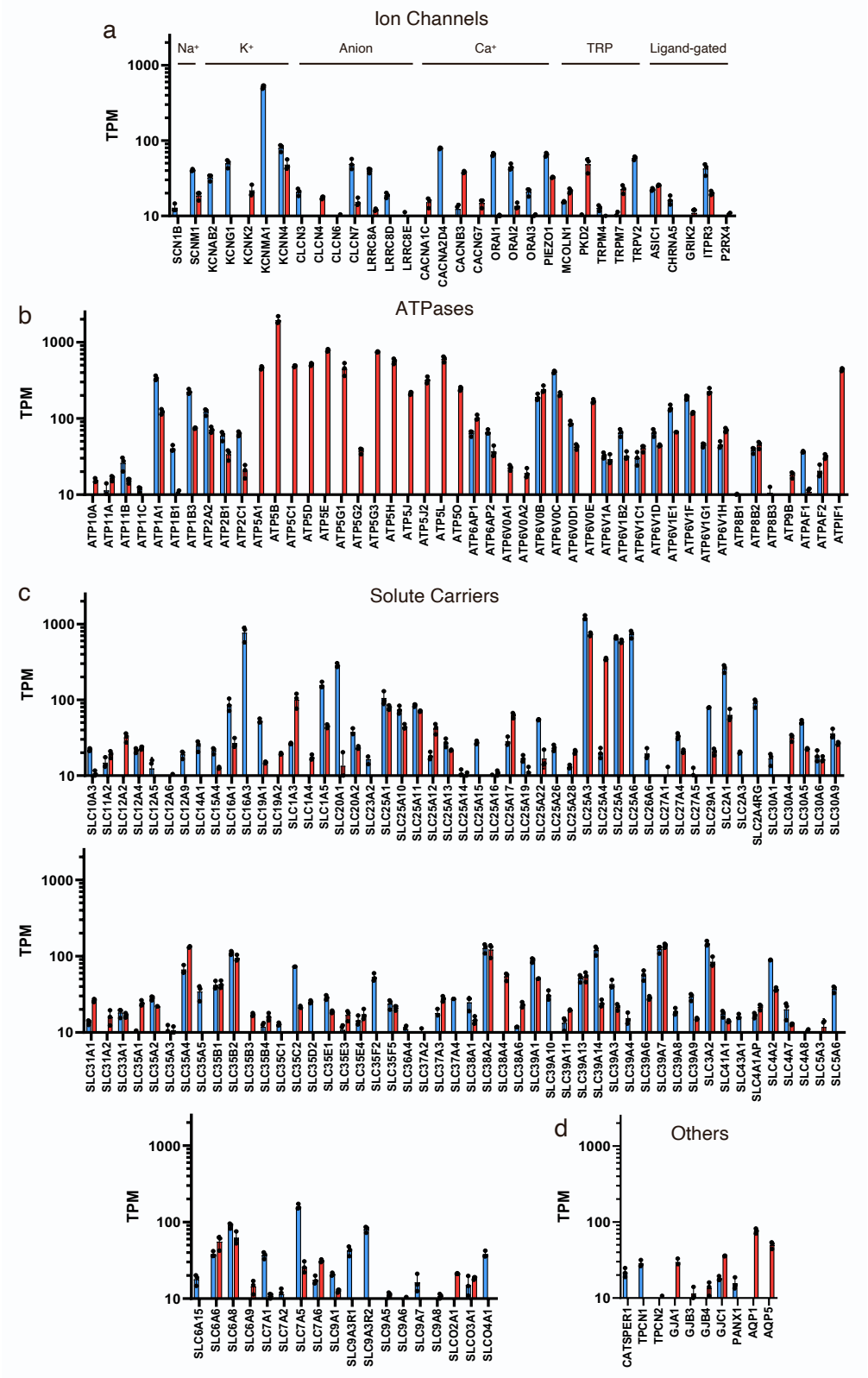

Figure S10: **RNA seq reveals ion transporters expression in 3T3 and HT1080.** (a-d) Ion transporters expressed at least 10 transcripts per million (TPM) in either 3T3 (red) or HT1080 (blue). Ion transporters are characterized into (a) passive ion channels (b) ATPases, (c) solute carriers, and (d) others. N = 3 biological repeats. Error bar represents standard deviation.

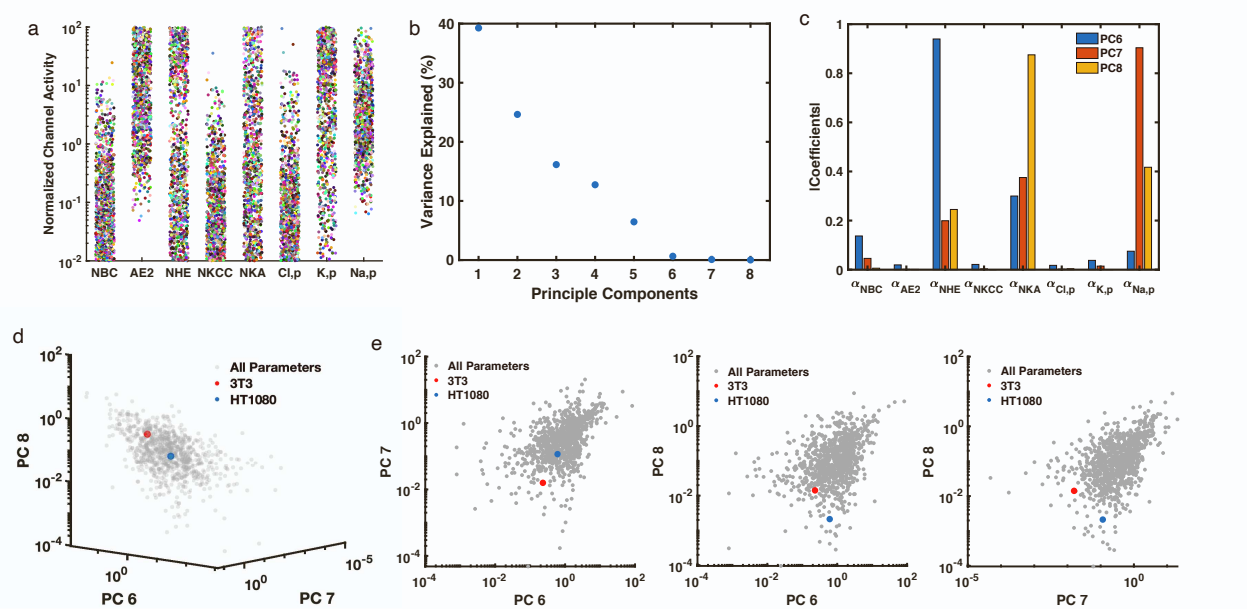

Figure S11: (a) Distribution of ion transporter activities that generate (50 $\pm$ 5)% regulatory cell volume recovery upon a hypotonic shock. Each activity level is normalized with respect to the corresponding base-line value. The base-line values become 1 after normalization. Each color represents a set of parameters obtained from the parameter search. (b) Variance explained at each principle components (PCs) of all parameters presenting in (a). (c) Eigenvectors of the covariance matrix of parameters presenting in (a) on PC 7, 8, and 9. (d) All parameters (gray), and parameters of 3T3 (red) and HT1080 (blue) projected on PC 7, 8, and 9. (e) 2D projections of (d).

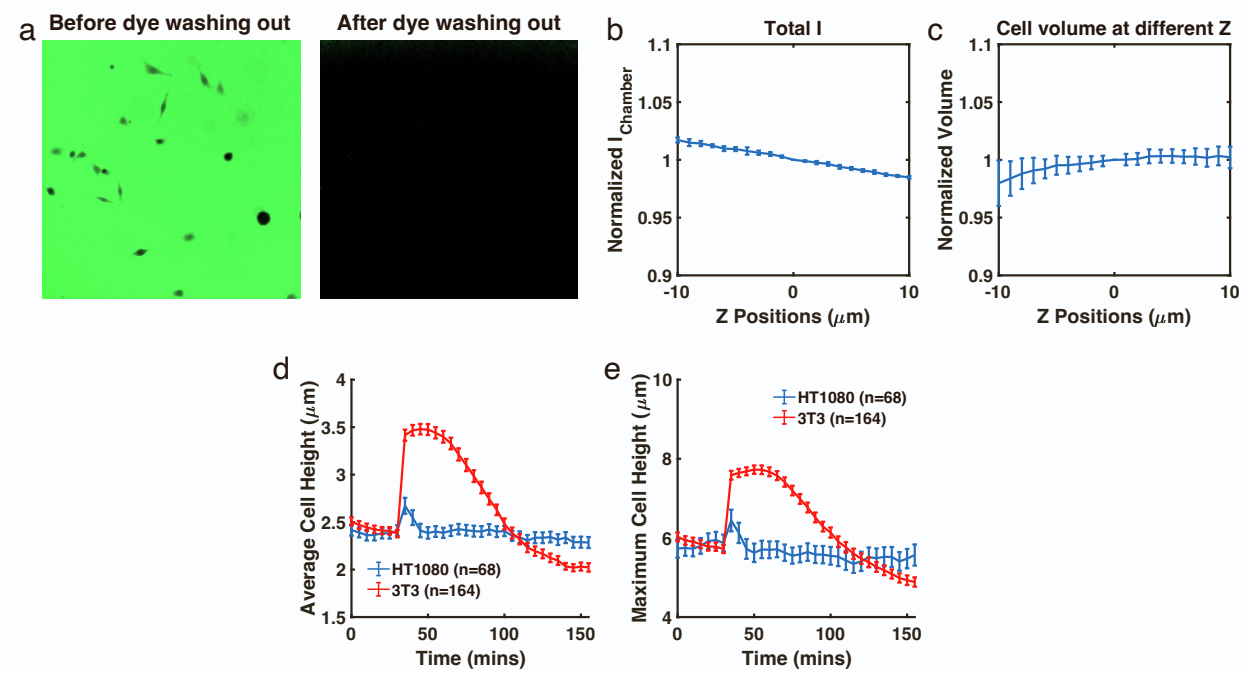

Figure S12: Benchmarking cell volume measurement using Fluoresence Exclusion method (FXm). (a) Representative epi-fluorescence images of FXm with and without dextran. Cells were incubated with Alexa Fluor 488 for 5 hours, followed by washing out with culture media. (b, c) The total fluorescence intensity of regions free of cells in FXm channel (b) and measured cell volume (c) with focused at different Z positions. (d, e)Average (d) and maximum (e) cell height of 3T3 and HT1080 cells during osmotic shock. Their volume are shown in Fig 1c and 1f. (b-d) Error bars represent the standard error of mean (SEM).

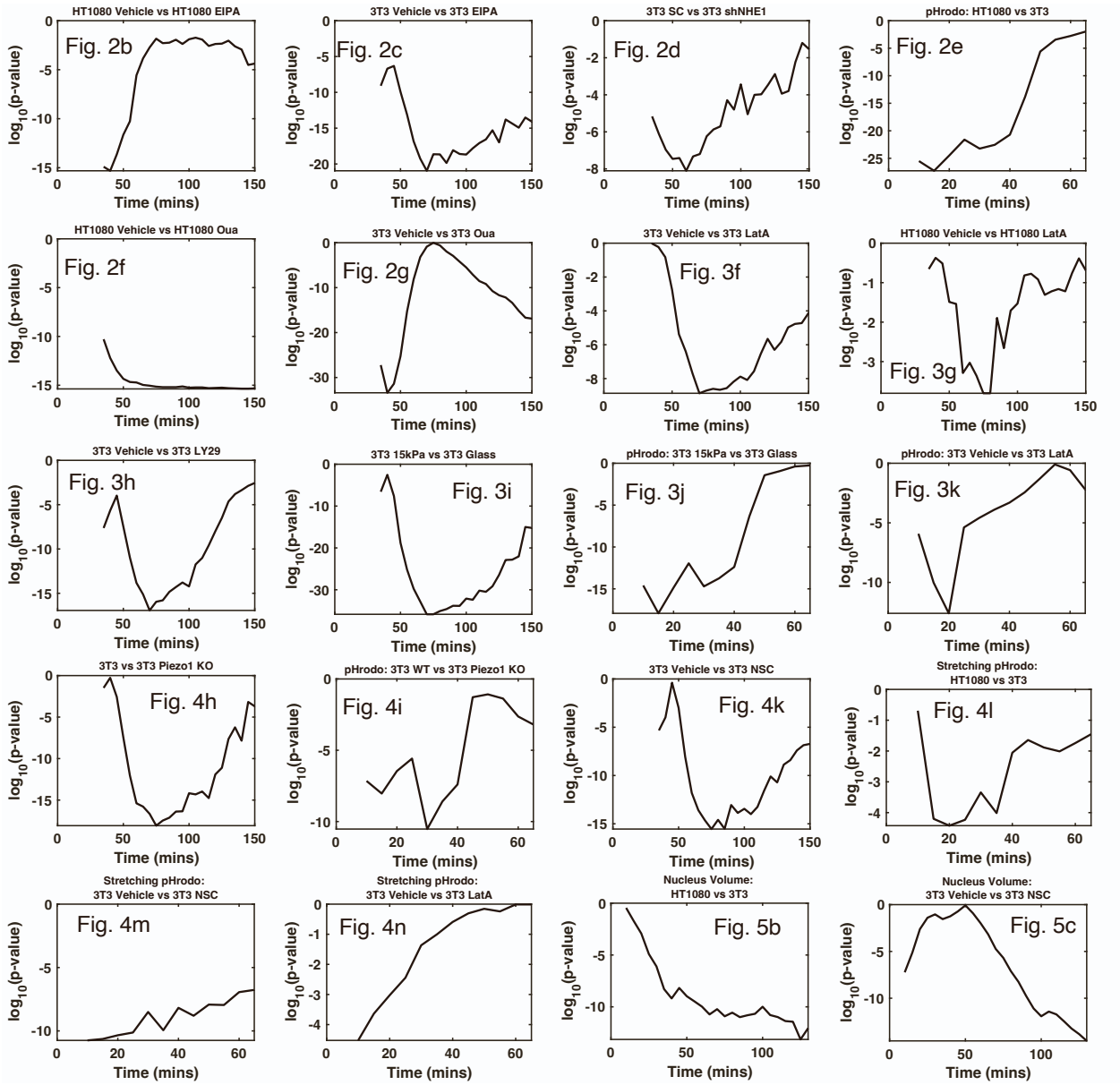

Figure S13: Statistical analysis of all time series plots in main figures.

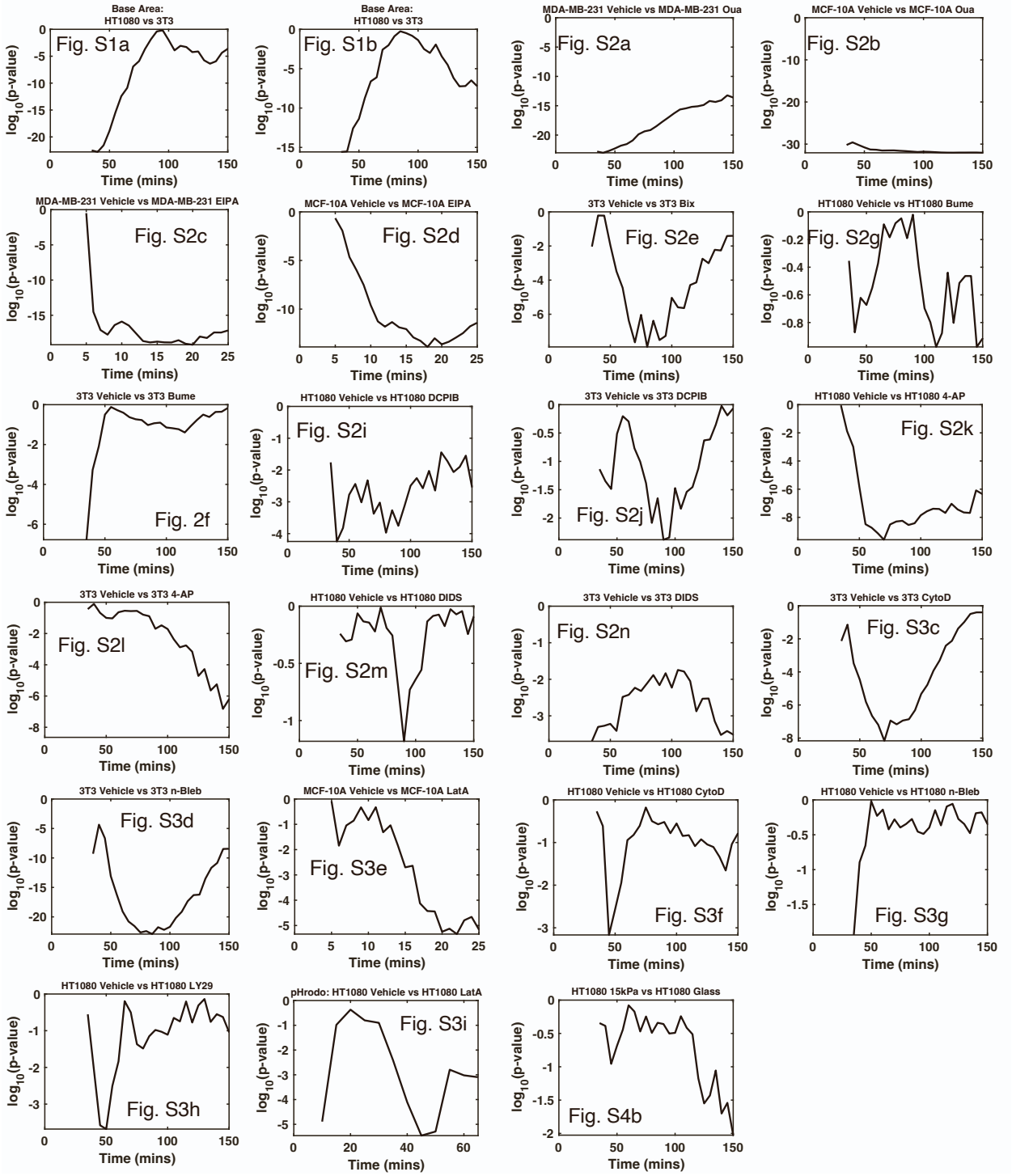

Figure S14: Statistical analysis of all time series plots in Supplementary figures S1-S4.

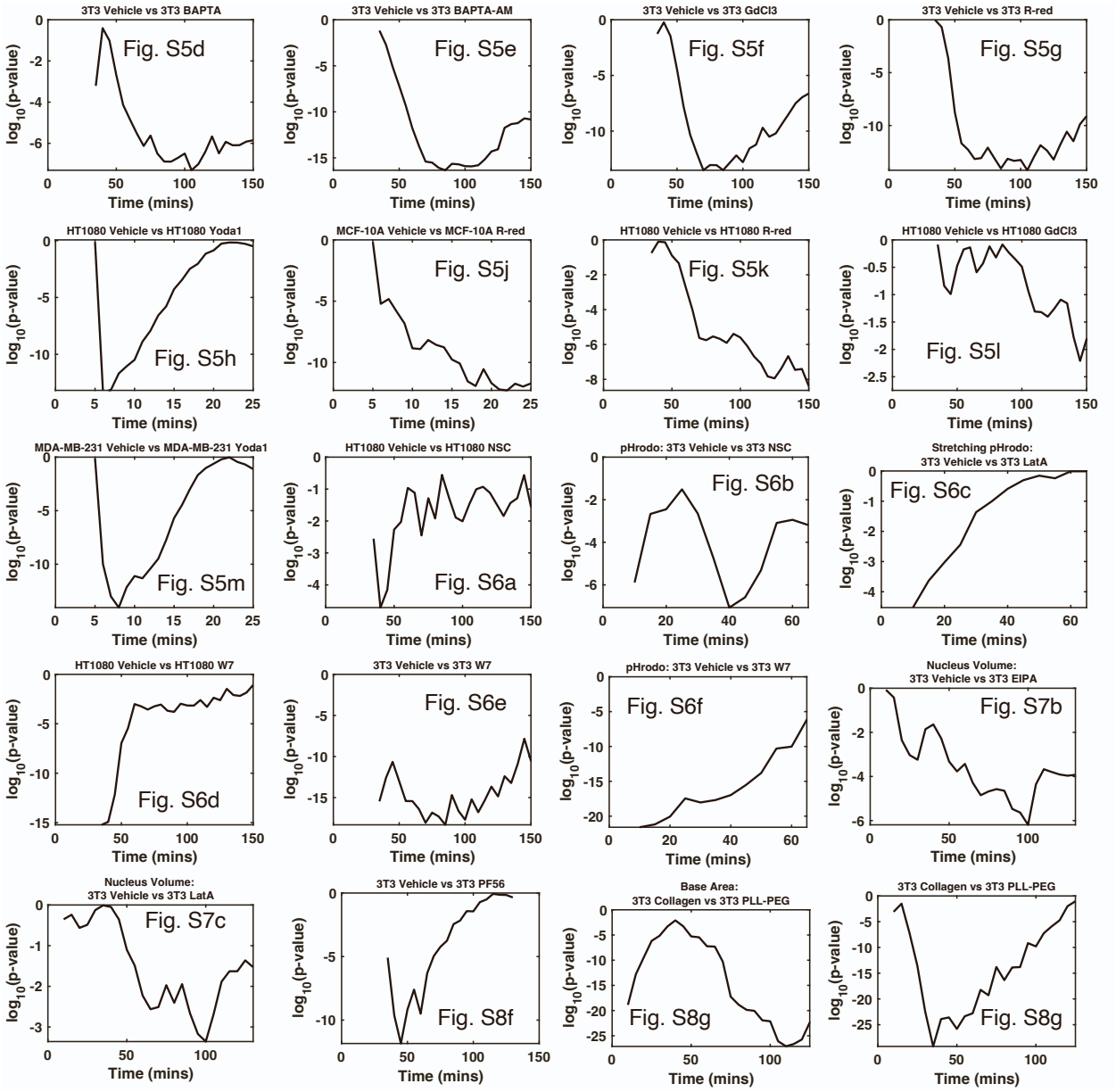

Figure S15: Statistical analysis of all time series plots in Supplementary figures S5-S7.

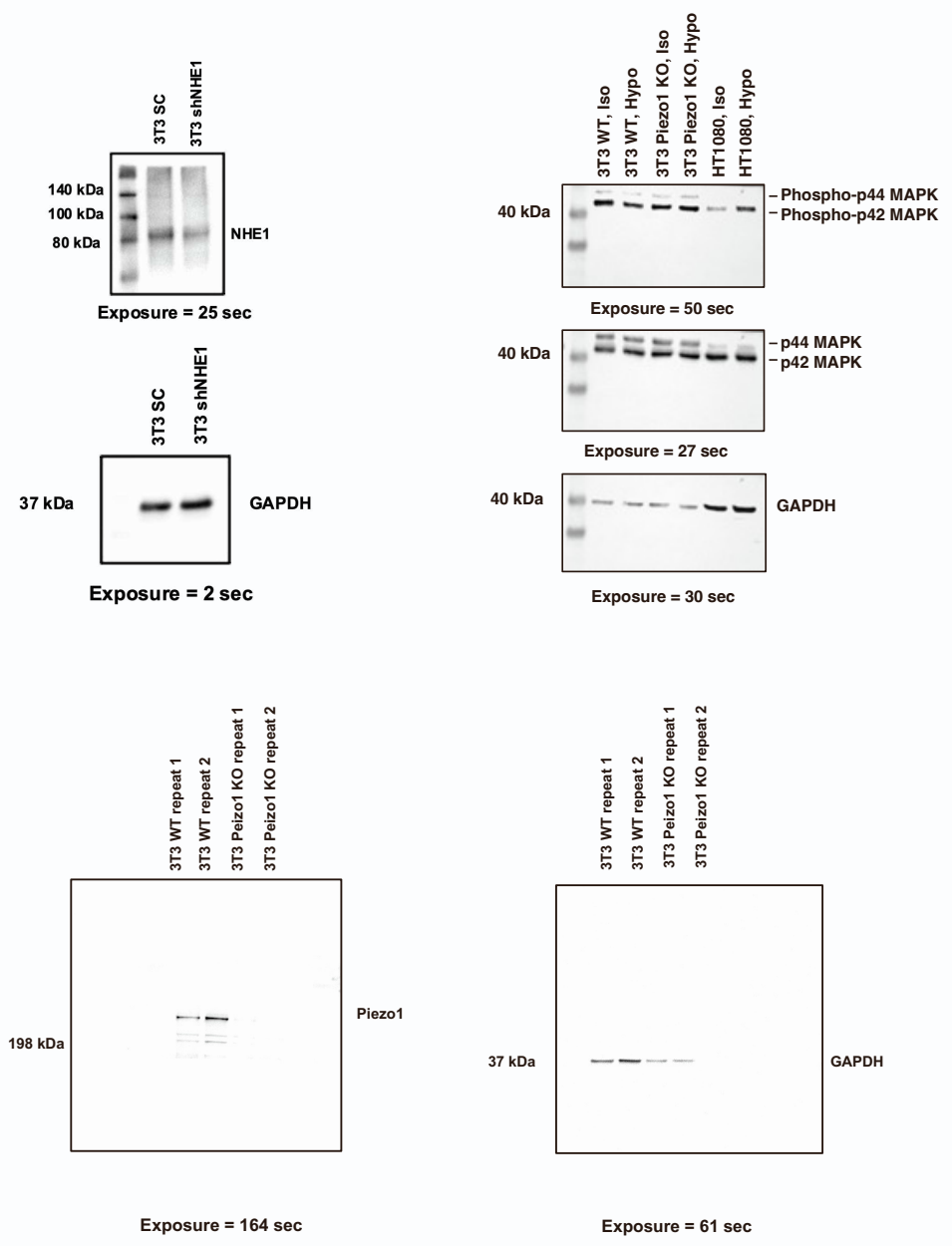

Figure S16: Uncropped western blot.

Table S1: Generic model parameters.

Parameter	Description	Value	Source
h (nm)	Cortical thickness	500	(*105*)
R (J/mol/K)	Ideal gas constant	8.31	Physical constant
T (K)	Absolute temperature	310	Physiological condition
σ_a (Pa)	Active contraction	10^3	(*105*)
N_A (mol)	Total intracellular A^-	0.142	Estimated
$N_{\mathrm{Bul}} + N_{\mathrm{HBul}}$ (pmol)	Total intracellular Buffer Solution	0.16	Estimated
α_{w} (m/Pa/s)	Permeability coefficient of water	10^{-10}	(*13*)
$\beta_{\text{NKA,Na}}$	Constant in J_{NKA}	0.1	Estimated
$\beta_{\text{NKA,K}}$	Constant in J_{NKA}	10	Estimated
β_1 (m/N)	In $G_m = [1 + e^{-\beta_1(\tau_m - \beta_2)}]^{-1}$	2×10^3	Estimated
β_2 (N/m)	In $G_m = [1 + e^{-\beta_1(\tau_m - \beta_2)}]^{-1}$	5×10^{-4}	Estimated
$\beta_{\text{NKA,1}}$ (1/mV)	In $G_{V,\mathrm{NKA}} = 2/[1 + e^{-\beta_{\text{NKA,1}}(V_m - \beta_{\text{NKA,2}})}] - 1$	0.03	(*106*)
$\beta_{\text{NKA,2}}$ (mV)	In $G_{V,\mathrm{NKA}} = 2/[1 + e^{-\beta_{\text{NKA,1}}(V_m - \beta_{\text{NKA,2}})}] - 1$	-150	(*106*)
$\beta_{\text{NHE,1}}$	In $G_{\mathrm{NHE}} = [1 + e^{\beta_{\text{NHE,1}}(\mathrm{pH} - \beta_{\text{NHE,2}})}]^{-1}$	15	(*107*)
$\beta_{\text{NHE,2}}$	In $G_{\mathrm{NHE}} = [1 + e^{\beta_{\text{NHE,1}}(\mathrm{pH} - \beta_{\text{NHE,2}})}]^{-1}$	7.2	(*107*)
$\beta_{AE,1}$	In $G_{\mathrm{AE2}} = [1 + e^{-\beta_{AE,1}(\mathrm{pH} - \beta_{AE,2})}]^{-1}$	10	(*107*)
$\beta_{AE,2}$	In $G_{\mathrm{AE2}} = [1 + e^{-\beta_{AE,1}(\mathrm{pH} - \beta_{AE,2})}]^{-1}$	7.1	(*107*)
k_H (atm/M)	Henry's constant	29	(*108*)
$P_{\mathrm{CO_2}}$ (atm)	Partial pressure of CO_2	5%	Physiological condition
K_c	pK for bicarbonate-carbonic acid pair	6.1	(*108*)
K_B	pK for intracellular buffer	6.7	Estimated
c^0_{Na} (mM)	Na^+ concentration in the medium	145	Physiological condition
c^0_{K} (mM)	K^+ concentration in the medium	9	Physiological condition
c^0_{Cl} (mM)	Cl^- concentration in the medium	105	Physiological condition
$c^0_{\mathrm{HCO_3}}$ (mM)	HCO_3^- concentration in the medium	35	Physiological condition
c^0_{G} (mM)	Molecular concentration in the medium	25	Physiological condition

Table S2: Base-line activity values for each channel and pump.

Parameter	Description	Value
$\alpha_{\text{Na},p}$ (mol^2/J/m^2/s)	Permeability coefficient of Na channel	$0.1P_0$
$\alpha_{\text{K},p}$ (mol^2/J/m^2/s)	Permeability coefficient of K channel	P_0
$\alpha_{\text{Cl},p}$ (mol^2/J/m^2/s)	Permeability coefficient of Cl channel	$0.2P_0$
α_{NKA} (mol/m^2/s)	Permeability coefficient of NKA	$10^5 P_0/RT$
α_{NKCC} (mol^2/J/m^2/s)	Permeability coefficient of NKCC	$10^{-3}P_0$
α_{NHE} (mol^2/J/m^2/s)	Permeability coefficient of NHE	P_0
α_{AE2} (mol^2/J/m^2/s)	Permeability coefficient of AE2	$0.1P_0$
α_{NBC} (mol^2/J/m^2/s)	Permeability coefficient of NBC	$1.5P_0$

Table S3: Parameters for HT1080 and 3T3 cells.

Parameter	Description	HT1080	3T3
$\alpha_{\text{Na},p}$ (mol^2/J/m^2/s)	Permeability coefficient of Na channel	1.12×10^{-11}	1.41×10^{-11}
$\alpha_{\text{K},p}$ (mol^2/J/m^2/s)	Permeability coefficient of K channel	1.27×10^{-8}	9.12×10^{-10}
$\alpha_{\text{Cl},p}$ (mol^2/J/m^2/s)	Permeability coefficient of Cl channel	8.78×10^{-12}	2.26×10^{-8}
α_{NKA} (mol/m^2/s)	Permeability coefficient of NKA	7.99×10^{-9}	3.06×10^{-9}
α_{NKCC} (mol^2/J/m^2/s)	Permeability coefficient of NKCC	2.04×10^{-10}	1.68×10^{-12}
α_{NHE} (mol^2/J/m^2/s)	Permeability coefficient of NHE	1.04×10^{-9}	1.19×10^{-10}
α_{AE2} (mol^2/J/m^2/s)	Permeability coefficient of AE2	5.75×10^{-12}	1.73×10^{-9}
α_{NBC} (mol^2/J/m^2/s)	Permeability coefficient of NBC	5.03×10^{-10}	3.46×10^{-8}
K_B	pK for intracellular buffer	8.55	4.73